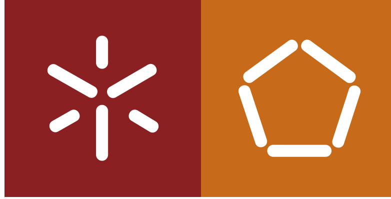

University of Minho
School of Engineering

Inês Eduarda Alves Pires

Development of a MEMS Actuator for Optical Modulation Enabling Enhanced Photonic Sensing

january 2023

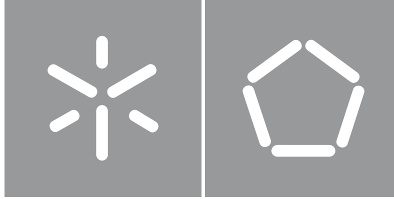

University of Minho
School of Engineering

Inês Eduarda Alves Pires

Development of a MEMS Actuator for Optical Modulation Enabling Enhanced Photonic Sensing

Masters Dissertation
Mestrado Integrado em Engenharia Eletrónica Industrial
e Computadores

Dissertation supervised by
Professora Doutora Graça Maria Henriques Minas
Doutora Rosana Maria Alves Dias

january 2023

Copyright and Terms of Use for Third Party Work

This dissertation reports on academic work that can be used by third parties as long as the internationally accepted standards and good practices are respected concerning copyright and related rights.

This work can thereafter be used under the terms established in the license below.

Readers needing authorization conditions not provided for in the indicated licensing should contact the author through the RepositóriUM of the University of Minho.

License granted to users of this work:

CC BY-NC-ND

https://creativecommons.org/licenses/by-nc-nd/4.0/

Acknowledgements

To my parents, for the love and unconditional support. Cândida Pires and Aníbal Pires, this one is for you. To my brother, Telmo, thank you for your friendship.

A big thank you to my supervisor, Professor PhD Graça Minas, and to my INL supervisor, PhD Rosana Dias, for the opportunity and knowledge transmitted.

To the people who walked by my side these years. A special shout goes to you, Gabriela Viana, Cátia Carneiro, Beatriz Machado, Rodrigo Pereira, João Borlido, Carlos Ribeiro, Jorge Pinto, Simão Leite, José Gomes, Paulo Pereira, Eduardo Fernandes, Diogo Cerqueira, Rui Lima and Dinis Fernandes. For the countless great memories and for keeping it real. Life is way better because you are part of it.

To the people I had the privilege to meet during my time at the International Iberian Nanotechnology Laboratory: Filipa Mota, Dimitri Santos, Filipe Alves, João Vieira and Jorge Pereira. Thank you for the help and words of advice. Inês Garcia, thank you for everything (name included).

Statement of Integrity

I hereby declare having conducted this academic work with integrity.

I confirm that I have not used plagiarism or any form of undue use of information or falsification of results along the process leading to its elaboration.

I further declare that I have fully acknowledged the Code of Ethical Conduct of the University of Minho.

University of Minho, Braga,

Inês Eduarda Alves Pires

Abstract

Silicon mechanical photonic wavelength converter (MPWC) has been investigated aiming at the need for all-silicon photodetectors in the infrared spectrum. All-silicon photodetectors have the advantage of low-cost micromachining but suffer from low efficiency and poor resolution (high noise levels), being unsuitable for wavelengths larger than 1 um. The operation of a MPWC requires high-frequency modulation, in the order of 1MHz, of a light beam over a few hundred microns.

Herein, a new MEMS (microelectromechanical system) actuator is proposed for integration into the MPWC. It consists of an interferometer in which the incident input light is modulated at a temporal frequency matched to the mechanic resonance of nanorods in the reference beam waveguide and relies on the resonance of the nanorods due to optical gradient force. The challenge is fabricating a MEMS shutter/actuator with high enough operating frequencies and enough displacement amplitude. High-frequency MEMS resonators exist but with limited displacements.

This works reports the development of a MEMS optical modulator with a grate shape to decrease the displacement amplitude required to modulate a 100x100 μm^2 beam area (necessary for application). Given the trade-off between resonance frequency and displacement amplitude typical of MEMS optical shutters, the challenge lies in having micrometre displacements at such a high frequency. MEMS design focused on minimizing movable mass, minimizing damping, and tuning the spring stiffness to set the resonance frequency at 500 kHz. The design includes 2 μm pitch grating (100x100 μm^2) on a support frame with metal sputtered on top, four springs and either parallel-plate or comb drive actuation electrodes.

The fabricated devices' experimental in-plane displacement and resonance frequency were measured by stroboscopic video microscopy on a Polytec MSA-500. The device was set in an acrylic chamber, and the results were extracted at atmospheric pressure and low vacuum. At low vacuum pressure, the quality factor increases and maximum displacement amplitudes are achieved.

Keywords High-frequency, optical, modulator, MEMS, displacement

Resumo

O conversor mecânico de comprimento de onda fotónico de silício (MPWC) foi investigado tendo em vista a necessidade de fotodetetores totalmente de silício no espectro infravermelho. Os fotodetetores totalmente de silício têm a vantagem de micro fabricação de baixo custo, mas sofrem de baixa eficiência e pouca resolução (níveis de ruído elevados), sendo inadequados para comprimentos de onda superiores a 1 μm. O funcionamento de um MPWC requer uma modulação de alta frequência, na ordem de 1 MHz, de um feixe de luz superior a algumas centenas de micros.

Assim, um novo atuador MEMS (sistema microeletromecânico) é proposto para integração no MPWC. Consiste num interferómetro em que a luz de entrada incidente é modulada numa frequência temporal correspondente à ressonância mecânica dos nanorods. O desafio é fabricar um obturador/atuador MEMS com frequências de funcionamento suficientemente altas e amplitude de deslocamento suficiente.

Este trabalho relata o desenvolvimento de um modulador ótico MEMS com uma forma de grelha para diminuir a amplitude de deslocamento necessária para modular uma área de 100x100 μm^2 (necessário para aplicação). Dado o compromisso entre a frequência de ressonância e a amplitude de deslocamento típica dos moduladores óticos MEMS, o desafio reside em ter deslocamentos de micrómetros a uma frequência tão elevada. O desenho MEMS centrou-se em minimizar a massa móvel, minimizar o amortecimento, e ajustar a rigidez das mola para definir a frequência de ressonância a 500 kHz. O desenho inclui uma grelha (100x100 μm^2) com 2 μm de espessura e metal no topo numa estrutura de suporte, quatro molas e elétrodos de acionamento (*parallel plates* ou *comb drives*).

O deslocamento experimental no plano e a frequência de ressonância dos dispositivos fabricados foram medidos por microscopia vídeo estroboscópica num Polytec MSA-500. O dispositivo foi colocado numa câmara de acrílico, e os resultados foram extraídos à pressão atmosférica e a baixo vácuo. A baixa pressão de vácuo, o fator de qualidade aumenta e a amplitudes máximas de deslocamento são alcançadas.

Palavras-chave Frequência, ótico, modulador, MEMS, deslocamento

Contents

Acknowlegdements ii

Abstract iv

Resumo v

Table of Contents vi

List of figures ix

List of tables xii

Acronyms xiii

1 Introduction 1

1.1 Motivation 2

1.2 Objectives 3

1.3 Organisation of the Dissertation 4

2 Literature Review 5

2.1 High-frequency MEMS devices 5

2.2 High-frequency MEMS devices for large displacements 8

2.3 Conclusions 9

3 Theoretical Foundations 11

3.1 One Degree of Freedom Micro actuator 11

3.2 Electrostatic Driving of Mechanic Actuator 14

3.2.1 Parallel Plate 14

3.2.2 Comb Drive 15

3.3 Elastic spring model 16
3.4 Damping 18
3.4.1 Squeeze film damping 18
3.4.2 Slide film damping 20
3.5 Maximum Displacement 21
3.6 Conclusions 21

4 Actuator Modelling and Analysis 23
4.1 Analytical Evaluation 23
4.1.1 Influence of geometry and actuation voltage on the displacement in SSP/MMP types of structures 25
4.1.2 Influence of geometry on the displacement in CD type of structures 28
4.2 FEM Evaluation 30
4.2.1 Resonance Frequency (Eigenfrequency Simulation) 30
4.2.2 In plane displacement and stress (static structural simulation) 32
4.2.3 Thermal Deformation 34
4.3 Designed MEMS Structures 35
4.4 Conlusions 38

5 Microfabrication 39
5.1 MEMS Modulator Process 39
5.1.1 MEMS Standard Micromachining Process 40
5.2 Devices Distribution on the SOI Wafer 41
5.3 Device MEMS Modulator Micromachining Process 43
5.3.1 Device Thinning 43
5.3.2 FS Metal Deposition 44
5.3.3 FS + BS SiO2 Deposition 44
5.3.4 Grid Patterning 45
5.3.5 BS Hard Mask Patterning 49
5.3.6 FS Device Patterning 49
5.3.7 FS Structure Etch 51
5.3.8 BS Structure Etch 53
5.3.9 Structure Release 54

5.3.10 Final Optical Inspection 55
5.4 Conclusions 57

6 Experimental Characterization **58**
6.1 Structure Selection and Packaging 58
6.2 Measurement Set Up 60
6.2.1 Polytec 60
6.2.2 Vacuum Chamber 61
6.3 Surface and Topography Analysis 63
6.4 Out of Plane and Vibration Analysis 64
6.5 In-plane Analysis 66
6.5.1 Measurements at atmospheric pressure 66
6.5.2 Measurements at Vacuum 67
6.6 Conclusions 72

7 Conclusions **74**
7.1 Future Work 75

References **79**

A Appendix - Alignment Marks Mask **80**

B Appendix - Metal Mask **81**

C Appendix - BS Mask **82**

D Appendix - Silicon Mask **83**

E Appendix - Chip Carrier **84**

List of Figures

1.1 Schematic illustration of MEMS components. 1
1.2 Schematic Sketch of the MPWC device. 2
1.3 Schematic Sketch of the MPWC device with the MEMS optical modulator. 3

2.1 Schematic view of clamped-clamped beam resonator [16]. 6
2.2 Two different resonators characterised in [17]. 7
2.3 Optical image of the fabricated resonator in [18]. 7
2.4 Accelerometer model [19]. 8
2.5 Device developed in [22] and respective displacement measured at 70 V DC and 8.6 V AC. 8
2.6 Measured responses in air and in vacuum for the device characterised in [25]. 9

3.1 1 DOF parallel plate actuator. 11
3.2 Step response of different quality factor devices. 13
3.3 Multiple parallel plates. 15
3.4 Comb drive actuator. 16
3.5 Guided fixed beam with referential and variables. 17
3.6 Squeeze film motion. 18
3.7 Slide film motion. 20

4.1 Different geometry approaches considered where (a) is the single parallel plate (SSP), (b) the multiple parallel plates (MPP) and (c) the comb drive (CD) types of structures. . . 24
4.2 Cross section of the SOI wafer. 24
4.3 Influence of the number of actuators on the dynamic displacement. 26
4.4 Influence of the thickness of the device layer on the dynamic displacement. 27
4.5 Influence of the actuation voltage on the dynamic displacement. 28

4.6 Influence of the number of combs on the dynamic displacement. 29

4.7 Simplified model for the modal and structural evaluation. 30

4.8 Eigenfrequency mode plots for l_s=17.1 μm. 31

4.9 Boundary load and fixed constraints (a) and displacement in x direction evaluation (b). . 32

4.10 Stress on a spring with 17.1 μm length (a) and 49.2 μm length (b). 33

4.11 Stress deformation at 288.15 K (a) and 298.15k (b). 34

4.12 Die 3D Model design. 35

4.13 Ten different structures and distribution on each die. 36

4.14 Structure 5 layout. 37

5.1 SOI Wafer cross-section. 40

5.2 Microfabrication process used. 40

5.3 Main fabrication process steps. 41

5.4 Devices distribution on SOI wafer. 42

5.5 Device layer thickness, Nanocalc. 43

5.6 Mask Aligner. 46

5.7 Metal layer patterning, OM after development. 47

5.8 Grid patterning, process steps and OM inspection. 48

5.9 Grid patterning, SEM inspection. 48

5.10 BS Patterning, process steps and OM after development on Karl Suss. 49

5.11 FS device patterning, OM after PR development. 50

5.12 FS device patterning gaps, OM inspection. 50

5.13 Device layer etch, SEM inspection after Pegasus. 51

5.14 Device layer etch, OM inspection. 52

5.15 Device layer etch, SEM inspection after ICP. 52

5.16 Grid inspection on EDX INCA software present on the FEI NovaNano SEM system. . . . 53

5.17 SEM inspection after structure etch. 53

5.18 BS trenches etch seen through the FS, OM. 54

5.19 Structure release, silicon oxide etch. 54

5.20 Wafer with the individual dies suspended. 55

5.21 Optical inspection results of a parallel plate (left) and comb drive (right). 56

5.22 Optical inspection results with structure collapse (left) and broken springs (arrows on right figure). 56

6.1 Chip carrier and respective cross-section. 59
6.2 Chip carrier with die connected through wire bonding. 59
6.3 Vacuum Chamber set up. 62
6.4 Final characterisation set up. 62
6.5 3D scanning of the C04D04S07 device (a) and C07D05S05 (b) 63
6.6 Scanning results of mentioned devices. 64
6.7 Out of plane and vibration analysis, C05D04S05. 65
6.8 Magnitude and phase of C05D04S05 device. 67
6.9 C05D04S05 device displacement magnitude at atmospheric pressure and low vacuum. 67
6.10 C05D04S05 device magnitude and phase at above -0.9 bar pressures. 68
6.11 C05D04S05 device magnitude displacement with constant DC and varying AC (top) and constant AC and varying DC (bottom). 70
6.12 C05D04S05 device magnitude displacement with constant DC and varying AC (top) and constant AC and varying DC (bottom), step 10 Hz. 71
6.13 C05D04S05 device magnitude displacement with constant DC and varying AC (top) and constant AC and varying DC (bottom), step 5 Hz. 72

List of Tables

1.1 Target characteristics of the MEMS optical modulator 4

2.1 Summary of the characteristics of the devices analysed in the literature review. 10

4.1 Initial simulation parameters for SSP type structures. 25

4.2 Initial simulation parameters for CD type structures. 28

4.3 Eigenfrequency study results when ls=17.1 μm and k=7300 N/m. 31

4.4 Eigenfrequency study results when l_s=42.9 μm and k=462.35 N/m.. 32

4.5 Layout dimensions of the ten structures. 35

4.6 Electrical and mechanical parameters for each structure. 38

5.1 Die ID matrix. 43

5.2 Nanocalc results. 44

6.1 Mechanical features adjusted. 59

6.2 Comsol Eigenfrequencies for the adjusted mechanical values with the one responsible for the in-plane vibration highlighted in bold. 64

6.3 Out of plane and vibration analysis frequency results. 66

6.4 Microstructure's Parameters. 68

Acronyms

BOX	Buried Oxide Layer
CMOS	Complementary Metal Oxide Semiconductor
MEMS	Micro Electro Mechanical Systems
MPWC	Mechanical-Photonic Wavelength Converter
FEM	Finite Element Method
AC	Alternating Current
DC	Direct Current
SDOF	Single-Degree of Freedom
SOI	Silicon on Insulator
FS	Front Side
BS	Back Side
PMMA	Polymethyl Methacrylate
PECVD	Plasma-Enhanced Chemical Vapor Deposition
CVD	Chemical Vapour Deposition
RF	Radio Frequency
MF	Mid-Frequencies
MA	Mask Aligner
DWL	Direct Writing Laser
UV	Ultraviolet
OM	Optical Microscope
PR	Photoresist
AM	Alignment Marks
PCB	Printed circuit board

Chapter 1

Introduction

Micro Electro Mechanical Systems (MEMS) is an interdisciplinary field of study committed to the physical integration of micromechanical systems with microelectronics, resulting in a miniature embedded system that involves micromachined components and structures. It is a technology that, in its most general form, can be defined as miniaturised mechanical and electromechanical elements, such as devices and structures made using the techniques of microfabrication. The critical physical dimensions of MEMS devices can vary from well below one micron on the lower end of the dimensional spectrum all the way to several millimetres. Likewise, the types of MEMS devices can vary from relatively simple structures having no moving elements to extremely complex electromechanical systems with multiple moving components under the control of integrated microelectronics [1].

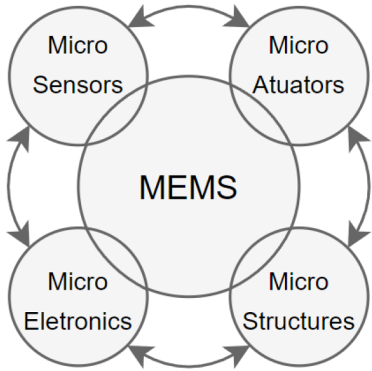

Figure 1.1: Schematic illustration of MEMS components.

While the functional elements of MEMS are miniaturised structures, sensors, actuators, and microelectronics, the most notable ones are the microsensors and microactuators. Microsensors and microactuators are devices that convert energy from one form to another. In the case of microactuators, these

generate mechanical motion of solids by converting one form of energy into kinetic energy such as electrostatic [2].

Over the past few decades, the microelectronics industry increased the fabrication of miniaturized systems based on silicon, with a lot of attention on the fabrication of microelectromechanical systems due to its versatility, mechanical properties, the abundance of potential silicon-based novel applications, and cost, being even so as one of the most affordable materials [3]. For these reasons, there has been growing interest in photonic devices based on Si-compatible materials in optical telecommunications and interconnection fields.

1.1 Motivation

Optics and photonics have significantly benefited from miniaturisation through MEMS [4]. And although Si has good optical, thermo-dynamical, and mechanical properties, Si is inefficient in telecom-light detection since it does not absorb light at a wavelength above 1 μm [5].

To develop all-silicon photodetectors and to take advantage of low-cost standard Si-CMOS processing technologies without additional material or process steps, several options have been proposed [6], for example, two-photon absorption [7], sub gap photo-effect, internal photoemission effect [8], and thermal nonlinear effect [9].

However, the previous methods have low efficiency and poor resolution due to high noise levels. A new concept was presented to solve these problems: a mechanical-photonic wavelength converter (MPWC) in Si, which can be used as an infrared detector and is not based upon absorption, figure 1.2. The approach consists of converting an incident amplitude-modulated infrared light signal into a light signal at a different reference wavelength with the same amplitude modulation [10]. The reference wavelength is below 1 μm, and a silicon detector can measure it.

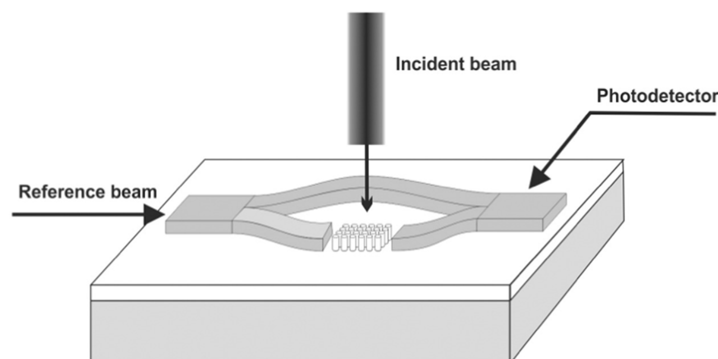

Figure 1.2: Schematic Sketch of the MPWC device.

The operation principle of the MPWC involves a reference beam sent through a waveguide fabricated on top of the wafer at a wavelength that can be absorbed by silicon. The light passes through a region with nanorods (pillars/wires along the direction perpendicular to the wafer) and reaches a Si photodetector [10]. The incident beam can be at any wavelength and illuminates the nanorod's structure region perpendicular to the surface of the wafer.

The MPWC utilises an optical gradient force induced on Si nanorod by an electromagnetic field of incident illumination. When a lens focuses an infrared beam on a surface filled with such Si nanorods, the photonic gradient force, which is directed laterally, leads to the mechanical bending of the nanorod. Furthermore, the MPWC takes advantage of the construction of nanorods by modulating the input beam at a temporal frequency matched to the mechanical resonance of the nanorods. The use of the resonant properties of the nanorod implies that a global shutter modulates the incident beam with a frequency equal to the resonant frequency of the nanorods.

1.2 Objectives

This dissertation aims to develop an optical modulator (figure 1.3) capable of operating at a sufficiently high frequency, thus creating the perfect match between the nanorods' mechanical resonance and the incoming light's pulse frequency. The mechanical resonance frequency of the nanorods is defined by the aspect ratio between the diameter and height of the pillars that constitute the nanorod array. The minimum achievable resonance frequency of the nanorods is limited by this aspect ratio, and it should not be below 1MHz.

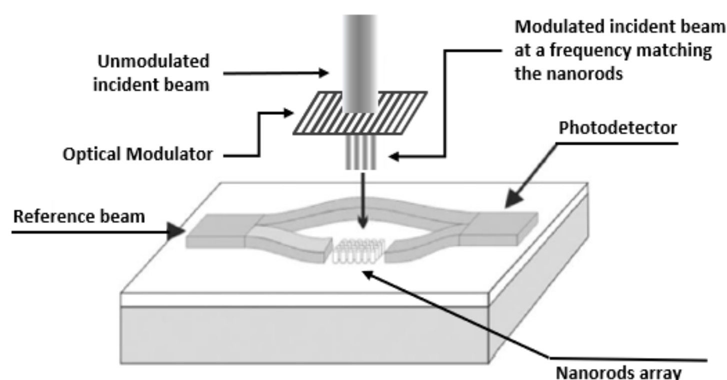

Figure 1.3: Schematic Sketch of the MPWC device with the MEMS optical modulator.

The challenge of the MEMS actuator required to be implemented in the MPWC lies in meeting the required displacement at such a high frequency, given the trade-off between resonance frequency and

displacement amplitude typical of MEMS optical shutters. To modulate all nanorods, the structure must move at a distance equal to the grid beam spacing. Therefore, to match the nanorods' mechanical resonance to the incoming radiation's pulse frequency, the incoming light must pass through a mechanical MEMS-based shutter operating at around 2 MHz.

Table 1.1: Target characteristics of the MEMS optical modulator

Characteristic	**Value**	**Unit**
Modulating frequency	1-2	MHz
Displacement	1	μm
Modulating area	100x100	μm^2
Actuation	<20	V

1.3 Organisation of the Dissertation

Initially, the literature was studied for microactuators operating at high frequencies, as well as their application and respective characteristics, such as operating frequency displacement actuation voltage, to name a few. Understand the operating principles that are the electrical and mechanical foundations for projecting and developing the device in question. And the subsequent analytical and Finite Element Method (FEM) analysis. Followed by the microfabrication of the projected devices and respective characterisation.

This dissertation is organised into seven chapters. The first is the Introduction chapter, where the motivation and objectives are described, followed by the literature review, which is presented and analysed. The third chapter, Theoretical Foundations, describes and studies the electrical and mechanical behaviour that the microactuator is based upon. Next is the Modelling and Analysis. The analytical and numerical models and evaluations were presented as well as the FEM modelling and simulation. The design and features implemented on the devices are also exhibited in this chapter.

Chapter five is Microfabrication, where the steps of the device fabrication process are detailed. Followed by the Characterisation in chapter six, where it is presented the tests performed on the device as well as the respective results. Finally, in the Conclusions chapter, the outcomes are enumerated as well as the plans for future work.

Chapter 2

Literature Review

This dissertation aims to develop an optical modulator that operates at high frequency and has a large displacement. To understand the specifications and requirements for this device, research was conducted on similar devices with similar characteristics. Many features required for meeting these characteristics are presented in other kinds of actuators. Accordingly, the literature was studied for MEMS devices operating at high-frequency and devices with the same goal application.

Depending on the application, the devices have a specific resonance frequency which is the natural vibrations frequency of the MEMS structure, and it is determined by the physical parameters and operating conditions of the actuator. The design of the incorporated actuators usually implies a compromise between displacement amplitude and frequency of operation [11]. The displacement of a movable structure is directly proportional to the quality factor and inversely proportional to the movable mass and resonance frequency, as demonstrated in more detail in 3.5.

Therefore, microactuators with a high operation frequency were looked into to understand their behaviour. The displacement and area were also considered since they are important features in developing the optical modulator. Its actuation methods and at what pressure the tests are performed are also considered. This chapter mentions devices that have been developed with a focus on specific frequency operation and devices that have been designed for displacement applications.

2.1 High-frequency MEMS devices

Microelectromechanical resonators are being developed and used in frequency-specific applications due to their specific resonance frequency [12]. The physical parameters and operating conditions of the MEMS resonators determine the natural vibration frequency of the MEMS resonators. Due to the miniature

size, the resonant frequency of MEMS resonators is typically in the kHz to MHz range, [13] [14].

In terms of specific frequency micro devices, resonators are developed to achieve higher or lower frequencies. Common applications for these devices are filters and oscillators. In general, the performance of MEMS resonators is assessed using two parameters, the resonance frequency and the quality factor. The different geometries of micromechanical resonators can achieve higher or lower frequencies, and various designs are, most commonly, the clamped-clamped beam and clamped-free beam. Other variations include free–free beams and suspended masses, among others, [15].

The work in [16] presents the implementation and characterisation of high-Q in-plane capacitive beam resonators with sub-100 nm to submicron transduction gap, figure 2.1. For a beam with 700x6 μm^2, the resonance frequency is 80 KHz and a quality factor of 74000. If the beam dimensions are adjusted to 200x10 μm^2, the clamped-clamped beam can achieve a resonance frequency of 3.2 MHz with a quality factor of 4500. The results are obtained with a custom vacuum system, which keeps the pressure below 1 mTorr.

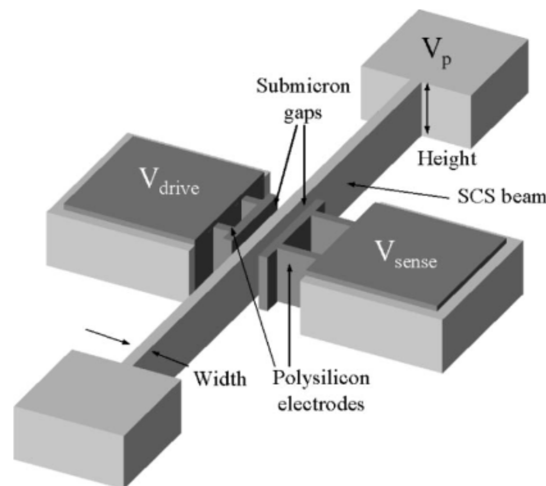

Figure 2.1: Schematic view of clamped-clamped beam resonator [16].

In addition, the work shown in [17] reports two different suspended mass resonators, and their respective characterisation are represented. Figure 2.2 is both resonators' microscopic (SEM) images.

The results were computed at 50 V biasing voltage, and for each resonator design, the frequency was calculated at atmospheric pressure and in vacuum (1 μTorr). For structure (a), the resonance frequency is 1.86 MHz with a Q-factor of 97 at atmospheric pressure and 1.87 MHz with a Q-factor of 610 at vacuum pressure, and for structure (b), the resonance frequency is 3.35 MHz with a Q-factor of 66 at atmospheric pressure and 3.36 MHz with a Q-factor of 446 at vacuum pressure.

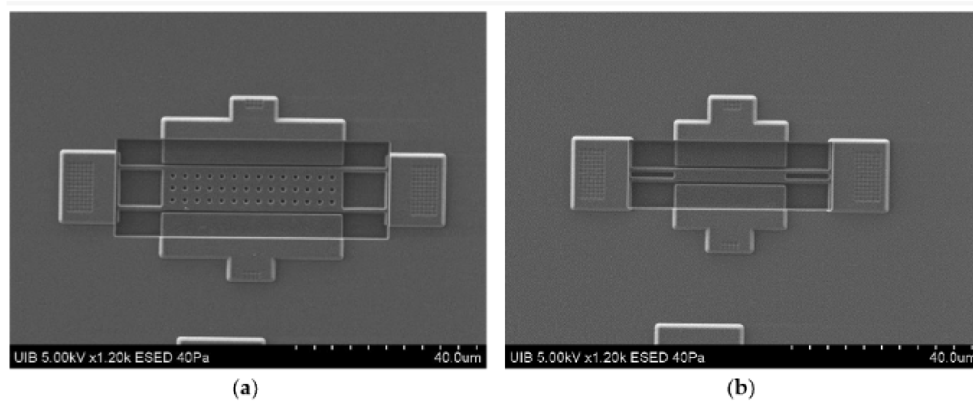

Figure 2.2: Two different resonators characterised in [17].

Moreover, the work presented on [18] reports the design and implementation of a high-frequency MEMS oscillator operating in air. The resonator is actuated by differential capacitive driving and has piezoresistive sensing. Figure 2.3 is an optical micrograph of the fabricated resonator. The area is 2x2 mm^2 with a SOI thickness of 25 μm and in air for a quality factor of 7337 has a resonant frequency of 2.201 MHz.

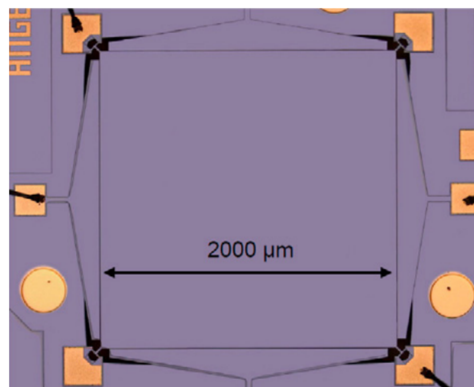

Figure 2.3: Optical image of the fabricated resonator in [18].

In [19] is detailed the design of single axis folded beam electro-statically actuated comb-drive-based accelerometer for high resonant frequency range applications. The accelerometer consists of three elements: free-hanging movable mass (200x200 μm^2), an attached comb pair and a fixed free-folded beam as shown in figure 2.4.

The proof mass is attached to the free end of folded beam structure which oscillates out-of-plane under the influence of applied forces. A constant DC voltage of 9.8 V is applied to the proof mass, and an AC voltage of magnitude 10 V is attached to the fixed comb structure, length is set to 200 μm and width to 21.5 μm to obtain the resonance frequency of 1 MHz. Proof mass displacement of 938.83 fm is obtained at this resonance.

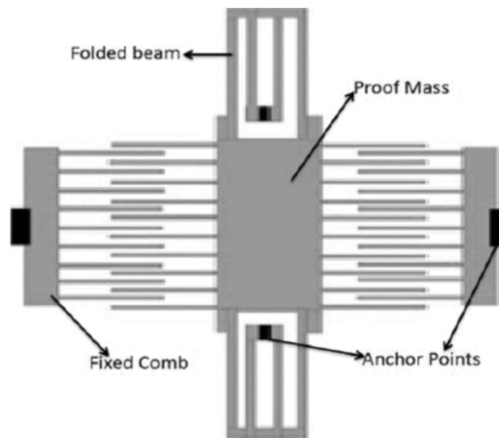

Figure 2.4: Accelerometer model [19].

2.2 High-frequency MEMS devices for large displacements

The resonators are MEMS devices developed for frequency specif applications, so the displacement amplitude is not the main concern. Other approaches were considered related to the goal application of the modulator to be developed: high-frequency devices with an in-plane displacement.

Electrostatic comb drives in-plane actuators have been developed for large displacements [20]. Typically, for a larger displacement, the resonance frequency is usually hundreds of Hertz, limited by the large size of the actuator needed for achieving the travel range [21].

A high-frequency in-plane MEMS actuator [22] has a parallel plate actuation and, at a frequency of about 90kHz, has a maximum displacement of 1.5 μm. At atmospheric pressure, the actuation voltages mentioned for this displacement are 150 V DC with 10 V AC. Similarly, [23] reports another approach with an in-plane comb drive actuator with a travel range of 2 μm for a resonance frequency of 93.5 KHz. The same design described here, but with a different spring, has an amplitude displacement of 5.5 μm at 26.055 KHz. Both these results are obtained at atmospheric pressures.

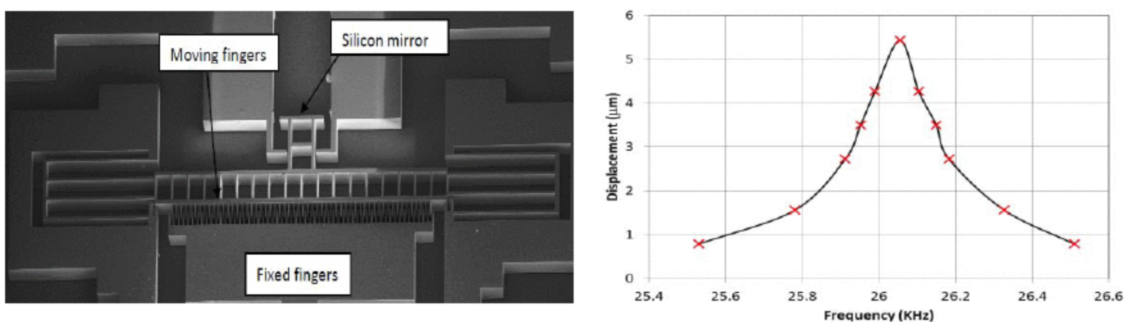

Figure 2.5: Device developed in [22] and respective displacement measured at 70 V DC and 8.6 V AC.

The oscillator studied in [24] has a movable mass of 515x20 μm^2. It has two sets of parallel comb

finger banks and four folded beams, which provide elastic recovery force for the oscillator. For this design, a driving voltage of 20V applied to the comb fingers results in an amplitude of motion of about 1um. At 7 mTorr, the natural resonance frequency is 26.48 kHz, and the quality factor is 640.

The work demonstrated in [25] studies the effects of reduced pressures on the dynamic behaviour of a micromirror. When operating in air at standard pressure, the actuator dynamics are affected. As the actuator moves, the gap between the two electrodes decreases, forcing the air out. The air leaves the cavity, dissipating energy through viscous drag at the actuator surface, and this dissipation effect can limit the actuator's behaviour.

Figure 2.6 depicts the resulting actuator response at standard atmospheric pressure (760 Torr) and then when it was sealed in a vacuum chamber (at 6 Torr). The left is the resulting displacement when submitted to air pressure, and the right is at vacuum pressure.

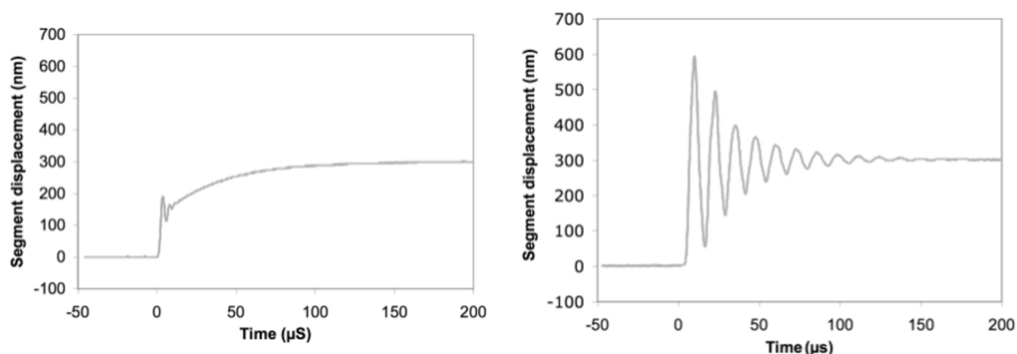

Figure 2.6: Measured responses in air and in vacuum for the device characterised in [25].

2.3 Conclusions

The challenge is fabricating a MEMS shutter/actuator with a high enough operating frequency and enough displacement amplitude. High-frequency MEMS actuators exist, but their displacements are limited to the picometre range, which is the case of the resonators. Displacements in the order of micrometre can be achieved, but the resonance frequency is less than 100 kHz.

High-quality factors generally mean higher operating frequencies, and by reducing the ambient pressure, it is possible to increase the actuator's displacement response. Both in frequency specif and displacement MEMS devices, the increase of the quality factor is used to improve the resulting parameters.

This means that for the development of the MEMS modulator, the challenge lies in having micrometre displacements at such high frequency with a movable structure with an area of 100x100 μm^2 (given the trade-off between resonance frequency and displacement amplitude typical of MEMS optical shutters).

The table 2.1 resumes the device's features analysed in this section. The product of the squared resonance frequency and the amplitude of the travel range is used as a " Figure of Merit" (FoM) for the actuator performance with units of nm.kHz^2, although the size of the actuator (in particular for this application, the area of the movable part), the pressure at which a given displacement is achieved, and also the voltage required for actuation are also relevant factors for comparison.

Table 2.1: Summary of the characteristics of the devices analysed in the literature review.

Work	**Frequency**	**Displ.**	**Area**	**Q**	**Pressure**	**Voltage**	**FoM**
Pourkamali, 2003 [16]	80 kHz	-	700x6 μm^2	74000	<1 mTorr	-	-
Pourkamali, 2003 [16]	3.2 MHz	-	200x10 μm^2	4500	<1 mTorr	-	-
Perelló-Roig, 2018 [17]	1.87 MHz	-	41x10 μm^2	610	1 uTorr	-	-
Perelló-Roig, 2018 [17]	3.36 MHz	-	25x3 μm^2	446	1 uTorr	-	-
Lin, 2010 [18]	2.2 MHz	-	2x2 mm^2	7337	atm	-	
Singh, 2013 [19]	1 MHz	938.83 fm	200x200 μm^2	-	-	9.8 V DC 10 V AC	0.001
Eltagoury, 2015 [22]	90 kHz	1.5 μm	-	-	atm	150 V DC 10 V AC	13.1
Eltagoury, 2016 [23]	93.5 kHz	2 μm	-	-	atm	100 -150V	17
Zhang, 2002 [24]	26.48 kHz	1 μm	515x20 μm^2	-	7mTorr	20 V	3.4
Bifano, 2005 [25]	40 kHz	600 nm	300x300 μm^2	-	6 Torr	-	0.96

Chapter 3

Theoretical Foundations

To model a MEMS device, it is necessary to consider the mechanical and electrical components that influence its behaviour. This chapter depicts the working equations of a one-degree-of-freedom actuator whose working principles are the same as the optical modulator to be developed.

3.1 One Degree of Freedom Micro actuator

MEMS resonators/modulators may be accurately modelled as single-degree of freedom (SDOF) damped oscillators because their vibrational response may be described as a single time-dependent position coordinate. The device developed during this dissertation operates as an SDOF electrostatic micro-actuator.

The system considered is a gap-varying parallel plate capacitor with one movable plate. The movable one is connected to a spring and a damper, and when voltage is applied across the parallel plates, the inter-plate distance changes [26].

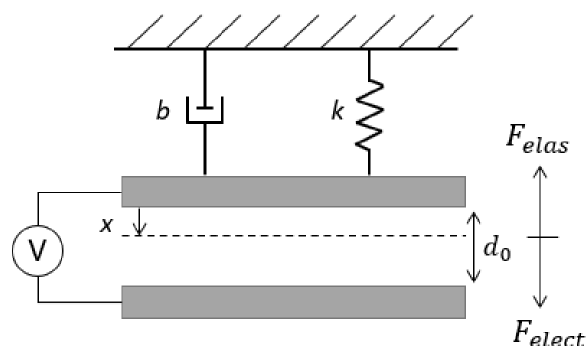

Figure 3.1: 1 DOF parallel plate actuator.

The capacitance between two parallel plates is

$$C_0 = \varepsilon \frac{A}{d_0} \tag{3.1}$$

where A is the overlapping area of the plates, d_0 the distance between the two plates, ε the relative permittivity of the medium between two electrodes, which is approximately equal to unity for air. If one plate moves towards the other, decreasing the inter-plate gap, the capacitance increases. Including the displacement of the device as the variable x, the new capacitance is:

$$C_x = \varepsilon \frac{A}{d_0 - x} = C_0 \frac{d_0}{d_0 - x} \tag{3.2}$$

This system presents a set of mechanical and electrical forces. The electrical force is the electrostatic force, and the mechanical ones are the elastic force, inertia, damping, and the force generated by external accelerations.

The equilibrium forces can be calculated as follows:

$$F_{elect} + F_{elas} + F_b + F_i = 0 \tag{3.3}$$

When a voltage V is applied between the parallel plates of the capacitor, an electrostatic force is generated that attracts the two plates together. When the distance between plates decreases, the capacitance and electrostatic force increase, according to:

$$F_{elect} = \frac{1}{2} V^2 \frac{C_x}{d_0 - x} = \frac{1}{2} V^2 \frac{C_0 d_0}{(d_0 - x)^2} \tag{3.4}$$

When the movable plate is displaced from its rest position by a distance *x*, the spring with a stiffness k causes a restoring force:

$$F_{elas} = -kx \tag{3.5}$$

The elastic force increases as the gap decreases, and it is contrary to the movement direction.

Next, if it is assumed that the damping is purely viscous, then if the mass moves with a velocity $v = \dot{x}$, the force exerted by the damper is:

$$F_b = -bv = -b\frac{dx}{dy} \tag{3.6}$$

where b is the damping coefficient. The inertia F_i arises due to the acceleration of the movable plate with a mass, *m*.

$$F_i = m\frac{d^2x}{dt^2} \tag{3.7}$$

Therefore, the equation 3.3 can be rewritten as:

$$\frac{1}{2}V^2\frac{d_0}{(d_0-x)^2} - kx - b\frac{dx}{dt} - m\frac{d^2x}{dt^2} = 0 \tag{3.8}$$

If there is no electrostatic force, the structure can be represented mechanically as a second-order system, and the previous equation is simplified to:

$$kx + b\frac{dx}{dt} + m\frac{d^2x}{dt^2} = 0 \tag{3.9}$$

The natural resonant frequency is $w_0 = \sqrt{k/m}$ and Q is the quality factor given by $Q = \sqrt{km}/b$ and the equation 3.9 can be rewritten as:

$$\frac{d^2x}{dt^2} + \frac{w_0}{Q}\frac{dx}{dt} + w_0^2x = 0 \tag{3.10}$$

The system can be divided into three categories regarding the quality factor: underdamped when Q>0.5, critically damped when Q=0.5, and overdamped when Q<0.5. An underdamped system is characterized by an oscillatory behaviour, and an overdamped system is by a non-oscillatory behaviour, as depicted in 3.2.

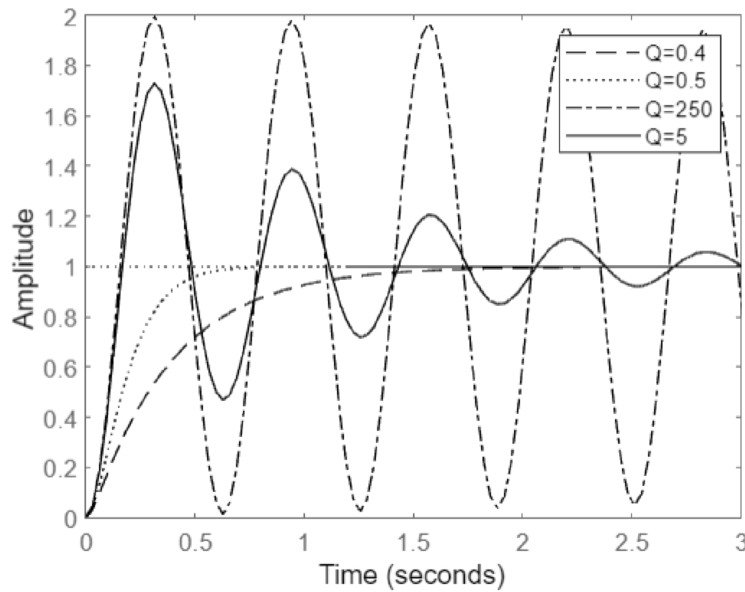

Figure 3.2: Step response of different quality factor devices.

3.2 Electrostatic Driving of Mechanic Actuator

3.2.1 Parallel Plate

The parallel plate approximation in 3.1 is considered to highlight the major aspects of the analysis. The mass is supported by elastic beams with stiffness, k, and it can move only in its normal direction. The mass is used as the movable electrode, and the fixed electrode is under the mass with the original gap distance of d_0. When the electrodes are supplied with a voltage difference, V, an electrostatic force is applied to the mass, pulling it towards the fixed electrode.

Once the mass is displaced, an elastic recovery force by the beams tends to pull the mass back towards its original position. The balanced position of the mass is determined by the force balance condition.

As inertia and damping forces are neglected in the static analysis, the joint action of the electrostatic force and the elastic force, the condition of force balance is

$$F_{total} = F_{elect} + F_{elas} = 0 \tag{3.11}$$

where F_{elect} is the electrostatic force and F_{elas} is the elastic recovery force. The balanced displacement is determined by

$$\frac{A\varepsilon\varepsilon_0 V^2}{2(d-x)^2} - kx = 0 \tag{3.12}$$

At a particular applied voltage, the magnitude of the electrostatic force equals the mechanical force. At this point, the electrostatic and the mechanical restoring forces balance each other. The applied voltage that breaks this equilibrium is named the pull-in voltage, V_{PI}. The voltage and displacement behind this phenomenon perform an essential role in the electrostatic actuators. The equilibrium points existing in this particular state can be found by solving the equation:

$$\frac{d|F_{elas}|}{dx} = \frac{d|F_{elect}|}{dx} \tag{3.13}$$

The only solution for x under where the equation 3.13 can be satisfied is for $x < \frac{1}{3}d_0$ and is the critical pull-in displacement.

When applied a voltage, $V > V_{PI}$, the F_{elect} is always larger than F_{elas}, resulting in the elastic force no longer compensating the electrostatic force. Consequently, the movable plate will always move towards the fixed electrode and finally snap into contact with the fixed electrode.

The pull-in voltage is found to be:

$$V_{PI} = \sqrt{\frac{8}{27}\frac{d_0^2 k}{C_0}} \tag{3.14}$$

For a voltage V smaller than V_{PI}, the displacement mass is given by the equation 3.12

Comb-like structures

The intertwined parallel plates form comb-like structures as in figure 3.3. The transverse movement of the plates maintains the overlapping area and changes the gap size between the plates.

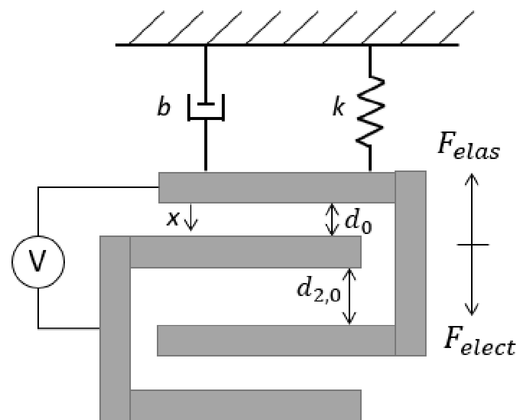

Figure 3.3: Multiple parallel plates.

In this configuration, in addition to the main gap d_0, there is a larger gap $d_{2,0}$ where electrostatic force is also generated, acting opposite to displacement.

Pull-in instability limits the minimum gap spacing between the fingers and the displacement. This limitation is critical in parallel-plate actuators, as transversely driven actuators' displacement is restricted to about one-third of the gap spacing. Once the driving voltage reaches the critical pull-in point, the microactuators will fail as their mobile comb structures stick to the fixed part.

3.2.2 Comb Drive

The motion of comb drive actuators and the parallel plate actuators is controlled by the equilibrium of the electrostatic force and elastic force from the springs.

During lateral motion or parallel actuation, the attractive force between two comb electrodes is mainly due to the fringing fields because the small fingers are thick compared with their width and length. Since the distance between the comb fingers is constant, the capacitance changes linearly regarding the plate area that overlaps during such movement.

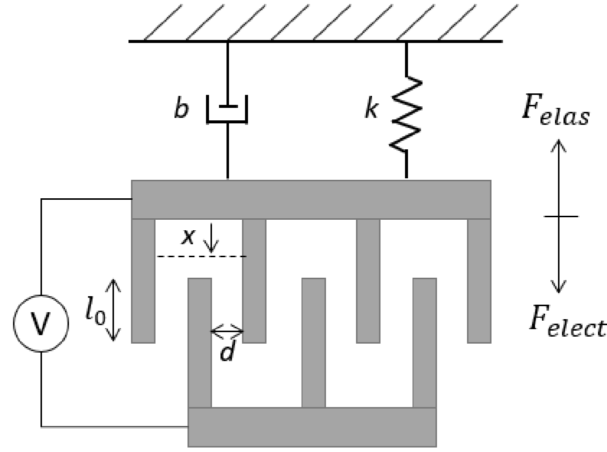

Figure 3.4: Comb drive actuator.

Keeping the direction of motion along the x-axis, the electrostatic force is

$$F_{elect} = \frac{nh\varepsilon\varepsilon_0}{d} V^2 \tag{3.15}$$

where n is the number of comb pairs; h is the thickness of the plate; d is the gap spacing; ϵ is the permittivity of the medium. The equation for the balanced displacement is

$$\frac{nh\varepsilon\varepsilon_0 V^2}{2d} - kx = 0 \tag{3.16}$$

where *h* is the height of the fingers, *d* is the distance between the movable electrode and the stationary electrode, and *n* is the number of active fingers.

Therefore, the balanced displacement of the movable mass is

$$x = \frac{nh\varepsilon\varepsilon_0 V^2}{2kd} \tag{3.17}$$

The plate displacement is directly proportional to the square of the applied voltage V.

3.3 Elastic spring model

To design the springs that support the movable structure is necessary to design the physical elastic components. Consider a fixed guided beam as depicted in figure 3.5 and the respective variables.

The movable structure is suspended by fixed guided beams where the height is equivalent to the thickness of the SOI device layer, width and length are to be determined. The stiffness of the springs is defined by the natural resonance frequency selected through the equation 3.18.

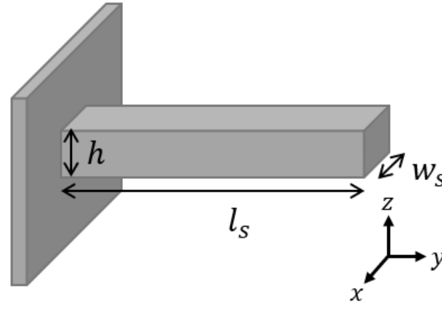

Figure 3.5: Guided fixed beam with referential and variables.

$$k = (2 * \pi * f_0)^2 * m \tag{3.18}$$

This value corresponds to the total elastic coefficient of the device and f_0 is the resonance frequency, and m is the equivalent mass of the moving parts driven by the supported spring. By increasing the number of springs implemented in the device, the number of support points of the movable structure is also being increased and, consequently, their stability. Thus, when several springs are connected in parallel to the same mass, the total elasticity coefficient corresponds to the sum of the elastic constants of all the springs in the system.

The elasticity coefficient of each parallel spring, k_x, is defined by $k_x = k/n$ where the n is the number of springs implemented in the device and k_x is the stiffness coefficient of the support system along the x direction and is given by 3.19.

$$k_x = \frac{12EI}{l_s^3} \tag{3.19}$$

Where I is the inertial moment, and E is the Young's modulus. The inertial moment is calculated by:

$$I = \frac{1}{12} h w_s^3 \tag{3.20}$$

Considering the elastic coefficient of each spring (3.19) and the equation for the inertial moment (3.20), the length of the spring, l_s, can be calculated by:

$$l_s = \sqrt[3]{\frac{12EI}{K_x}} \tag{3.21}$$

The spring length varies when the mass frame and established resonance frequency also vary. If the mass is suspended on four springs, the total stiffness coefficient of the structure is $k = 4k_x$.

3.4 Damping

3.4.1 Squeeze film damping

Air damping is related to the surface of the moving parts, and it is important for microdevices and systems in determining their dynamic performance due to the large surface area to volume ratio of the moving parts, [27].

As shown in figure 3.6, the movable plate moves towards the fixed one, and the air film between them is squeezed so that some of the air flows out of the gap. When this happens, additional pressure develops in the gap due to the viscous airflow. On the contrary, when the plate moves away from the wall, the pressure in the gap is reduced to keep the air flowing into the gap.

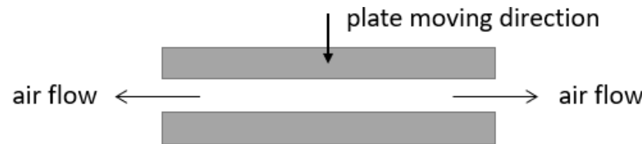

Figure 3.6: Squeeze film motion.

In both moving directions of the plate, the forces on the plate caused by the built-up pressure are against the movement of the plate. In other words, the air film acts as a damper, and the damping is called squeeze-film air damping. The damping force of squeeze-film air damping depends on the gap distance; the smaller the gap, the larger the damping force [28].

The squeeze-film air damping has significant effects on the dynamic behaviour of microstructures and is prevalent in systems where the air gap thickness is sufficiently small compared to the lateral dimensions of the structure.

For structures where the air gap thickness changes in time, the pressure changes *p* relative to the wall velocity are described by the Reynolds equation [29]:

$$\frac{d^3}{12\eta}(\frac{\partial^2 p}{\partial x^2}+\frac{\partial^2 p}{\partial y^2})=\frac{d}{P_a}\frac{\partial p}{\partial t}+\frac{\partial d}{\partial t} \tag{3.22}$$

Where P_a is the ambient pressure, η is the gas viscosity, and d is the gap between plates.

If the spring effect is disregarded, the damping coefficient is given by:

$$b=\frac{768wl\eta}{\pi^6 d^3}\sum_{m,n,odd}\frac{1}{(mn)^2(\frac{m^2}{w^2}+\frac{n^2}{l^2})} \tag{3.23}$$

Where *m* and *n* are odd integers, and w and l are the width and length of the parallel surfaces, respectively.

Rarefaction Effects

One of the most significant effects present in squeeze film flow in MEMS structures is that of rarefaction. This effect arises because of the extremely small gaps in which the air or gas is forced to flow.

For gases, the Knudsen number, k_n, defined as the ratio of the mean free path of the gas molecules to the characteristic flow length, provides a very good measure of rarefaction.

$$K_n = \frac{\lambda}{d} \tag{3.24}$$

where λ is the mean free path of molecules and d is the typical dimension of the damping structure.

For Knudsen numbers in the transitional regime ($0.01 \leq k_n \leq 3$), the Navier-Stokes equations can be used with a single modification - the boundary condition at the fluid-solid interface is changed from the standard non-slip condition to that of a slip-flow condition. In gas film theory, the viscosity coefficient usually includes the slip-flow condition. This way the resulting coefficient is an effective viscosity η_{eff} that takes into account the rarefaction effects:

$$\eta_{eff} = \frac{\eta}{Q_{pr}} \tag{3.25}$$

Where η is the viscosity of the gas and Q_{pr} is the relative flow rate coefficient and is given by:

$$Q_{pr} = 1 + 9.658 k_n^{1.159} \tag{3.26}$$

Border Effects

The squeeze-film model was derived from the assumption of gas pressure at the surface borders at ambient pressure. This condition is true if the surface dimensions are larger than the film thickness. However, in practical devices, the flow escaping from the damper borders might significantly affect the damping coefficient.

The border effects can be included in the analytically derived squeeze-film model if a modified surface length $l_0 = l + \triangle l$ and surface width $w_0 = w + \triangle w$ are used. The (ref here) model reports the following effective elongations:

$$l_0 = l + 1.3(1 + 3.3k_n)d \tag{3.27}$$

$$w_0 = w + 1.3(1 + 3.3k_n)d \tag{3.28}$$

The elongations depend on both the gap size and the Knudsen number, and if l and w are replaced by l_0 and w_0 in 3.23, the border effects are included in the squeeze film model.

3.4.2 Slide film damping

Slide film damping occurs when two plates of area A, separated by a distance d, slide parallel to each other as shown in figure 3.7. The relative motion of the parallel structure leads to a fluid flow that exerts a force opposing the relative motion.

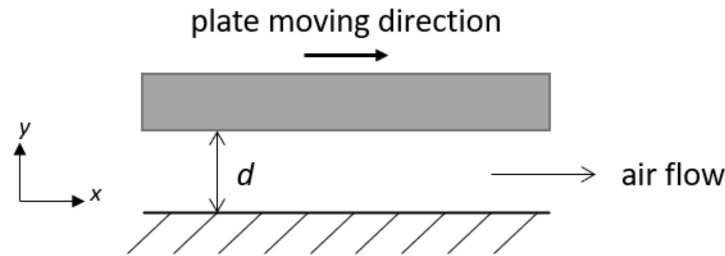

Figure 3.7: Slide film motion.

As shown in figure 3.7, the plate at y=d moves a velocity in the direction of the x-axis, while the second one, y=0, is fixed. At low surface velocities, the gas velocity profile can be assumed to be linear, and due to gas rarefaction, the gap width effectively increases by 2λ, where λ is the mean free path of the gas. According to [30], the shear stress at one of the surfaces is

$$\tau = \frac{\eta A}{d + 2\lambda} v_x \tag{3.29}$$

where A is the surface area and η is the viscosity coefficient. The contribution of the mean free path can be included in the effective viscosity by

$$\mu_{eff} = \frac{\mu}{1 + 2k_n + 0.2k_n^{0.788} e^{-k_n/10}} \tag{3.30}$$

where k_n, the Knudsen number, is the measure of the rarefaction effect. It is the ratio between the mean free path λ and gap height d: $k_n = \lambda/d$. The resulting damping coefficient b is then simplified to

$$b = \frac{\tau}{v_x} = \frac{\mu_{eff} A}{d} \tag{3.31}$$

To extend the damping model to be valid at higher frequencies, the time-dependent velocity profile of the gas must be considered. The dynamics of the gas are modelled with the one-dimensional diffusion equation

$$\frac{\partial v(y)}{\partial t} = v\frac{\partial^2 v(y)}{\partial y^2} \tag{3.32}$$

where v is the kinematic viscosity $v = \eta/\rho$ and ρ is the density of the gas.

3.5 Maximum Displacement

Considering the equation for the natural resonance frequency:

$$w_0 = \sqrt{\frac{k}{m}} \tag{3.33}$$

where k is the spring stiffness and m is the movable structure mass. The spring stiffness is given by

$$k = mw_0^2 \tag{3.34}$$

Considering the equations of balanced displacement where the electrostatic force and elastic force have the same value and the elastic force is $F_{elas} = xk$ the displacement can be written as

$$x = \frac{F}{k} \tag{3.35}$$

There are different damping coefficient outputs for different air pressure: lower air pressure leads to a lower damping factor [31]. Squeeze-film gas damping is a determinant of the dynamic behaviour of MEMS, especially at low ambient pressures, which influences the mechanical quality factors of the microfabricated actuator [32]. Therefore, manipulation of the Q factor essentially involves the manipulation of damping in the structure.

The dynamic behaviour of a MEMS structure is related to the pressure conditions, and the maximum displacement can be calculated as an approximation:

$$x_{max} = x * Q \tag{3.36}$$

where x is the displacement at the condition of force balance.

3.6 Conclusions

The theoretical foundations behind the behaviour of an electrostatic actuator have been detailed. A series of applied forces of both mechanic and electrical origin are present in the behaviour of this

device which is based on a parallel plate capacitor. It is possible to analyse three different electrostatic-driven mechanical actuators and their respective static analysis where the conditions for force balance are established.

The damping effects are considered an important aspect of analysing the displacement of the movable mass. This way, an underdamped system with a large quality factor translates to an oscillatory behaviour, and the damping can be computed. Therefore, in an oscillatory system, an equilibrium of electrostatic and elastic forces persists, and the displacement of the movable mass is amplified in proportion to the quality factor.

This chapter presents the main equations that translate the behaviour of the modulator based on parallel plates, with 1DOF, to be dimensioned. It is now possible to model a MEMS device to accommodate the desired working characteristics.

Chapter 4

Actuator Modelling and Analysis

In the process of modelling, analysing and evaluating a device, it is necessary to go through the numerical analysis and FEM modelling with the respecting evaluation. The different models that describe the modulator performance will be presented in this chapter. Initially, the parameters that are essential to the numerical evaluation and that can be computed analytically will be studied considering the restrictions imposed.

With the results of the analytic analysis and the numerical model, it is essential to develop a FEM model. A FEM model and its simulation aim to represent complex physical phenomena through a theoretical mathematical model, describing them by equations and solving them to get real phenomena approximations. The simulation tool used is COMSOL Multiphysics 5.4.

In this chapter, the analytical evaluation is performed in Matlab, and the respective geometry and behaviour analysis results are fundamental to developing a FEM model where the computed results are further studied and compared to the established analytical parameters.

4.1 Analytical Evaluation

The modulator design concept is, in the most simple terms, a moving grid supported by four springs. The three types of electrostatic driving actuators analysed in the previous chapter were considered as the actuation for the optical modulator.

Therefore, three different types of electrostatic driving actuators were considered in the modulator design: parallel plate, multiple parallel plates and comb drive. The concept for the different geometry approaches considered are depicted in figure 4.1 as (a) is the parallel plate actuation model, (b) the multiple parallel plate model and (c) the comb drive model. The geometry parameters are depicted where

d_0 is the electrostatic actuator distance, w_s and l_s are the spring width and length, respectively, l_g is the grid length, l_a is the actuator length and w_a the width.

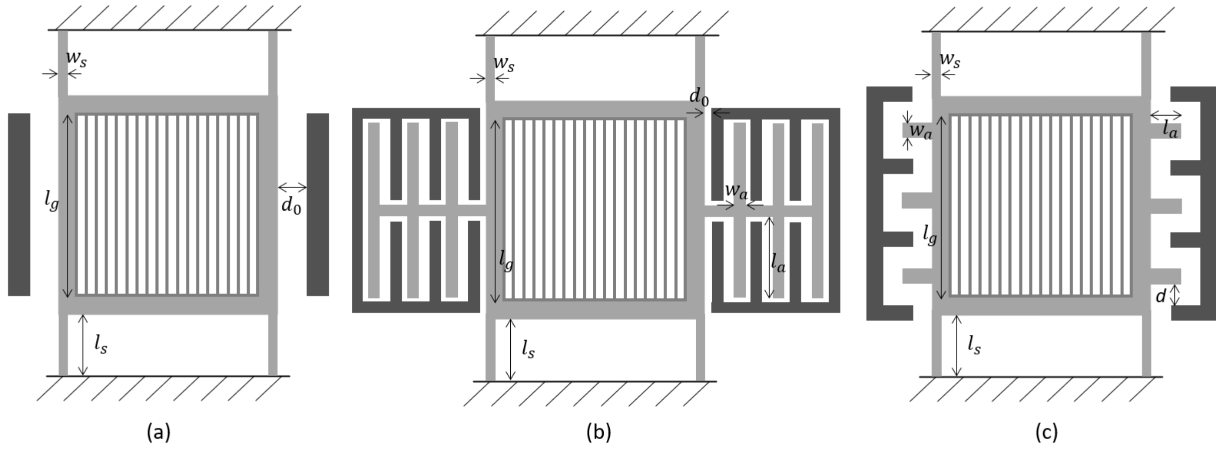

Figure 4.1: Different geometry approaches considered where (a) is the single parallel plate (SSP), (b) the multiple parallel plates (MPP) and (c) the comb drive (CD) types of structures.

It was necessary to establish some initial parameters to compute the features that constitute the layout of the actuators to be developed. All the parameters except the non-linear damping coefficient can be easily determined through analytical calculation considering the established ones.

The initial parameters were defined considering the thickness of the wafer, the modulating area of the structure and the operating resonance frequency and are as follows:

- First, the wafer used for this dissertation is a Silicon on Insulator (SOI) wafer, meaning it is a silicon wafer with a thin silicon film on insulating oxide. It is composed of a set of three layers: the device layer (made of silicon and 5 μm thick), the buried oxide layer (made of silicon oxide and 2 μm thick) and the handle layer (made of silicon and 650 μm thick), figure 4.2;

Figure 4.2: Cross section of the SOI wafer.

- It was established that the modulator grid, defined by the modulating area, is 100x100 μm^2 with a surrounding frame of 10 μm wide. Also, some devices have a modulating grid of 200x200 μm^2, and the surrounding frame maintains the same width.

- The devices are projected to achieve either a frequency of 0.5 MHz or 2 MHz, so the features added to the movable mass are intrinsically related to the resonance frequency wanted. The goal application of the modulator requires that the operating resonance frequency is set at 2 MHz, but for characterisation purposes, there were devices designed to operate at 0.5 MHz.

Aiming for the target characteristics and the system's structural behaviour, the remaining variables were calculated using the equations mentioned in the previous chapter.

The different geometry approaches lead to different considerations on the layout design, for instance, the gap distance between actuator plates (d_0), the number of combs in the movable structure on a single side (Na), device thickness (h) and actuation voltage (V).

4.1.1 Influence of geometry and actuation voltage on the displacement in SSP/MMP types of structures

Considering the SSP structure, with a grid area of 100x100 μm^2, a spring width of 3 μm and a resonance frequency of 0.5 MHz, the spring length is calculated using the elastic spring model present in 3.3, and the results are computed using the system behaviour equations.

Table 4.1 presents the geometrical parameters used for the simulation. Where the number of actuators, device thickness and the applied voltage is considered.

Table 4.1: Initial simulation parameters for SSP type structures.

Parameter	**Value**	**Unity**
Spring width, ws	3	μm
Spring length, ls	42.9	μm
Grid length, lg	100	μm
Height, h	5	μm
Grid beam spacing, sg	1	μm
Grid beam width, wg	1	μm
Applied voltage, V	10	V

Number of actuators

The number of actuator plates in the movable structure is considered. If the number of actuator plates increases, the electrostatic force (3.15) and the static displacement of the movable mass (3.16)

both increase. The quality factor decreases as the damping increases.

Overall, increasing the number of actuator plates leads to an increase in the modulator static displacement and an increase in the dynamic displacement, although not significant because the quality factor value is less. Maintaining the other parameters and only changing the number of actuator plates, the results can be seen in figure 4.3. The three graph plots presented are for the obtained static displacement, quality factor, and dynamic displacement. The plots are in function of the varying actuator gap (d_0), the dotted black line is for the goal displacement (1 um), and the grey dotted line is the maximum pull-in gap spacing.

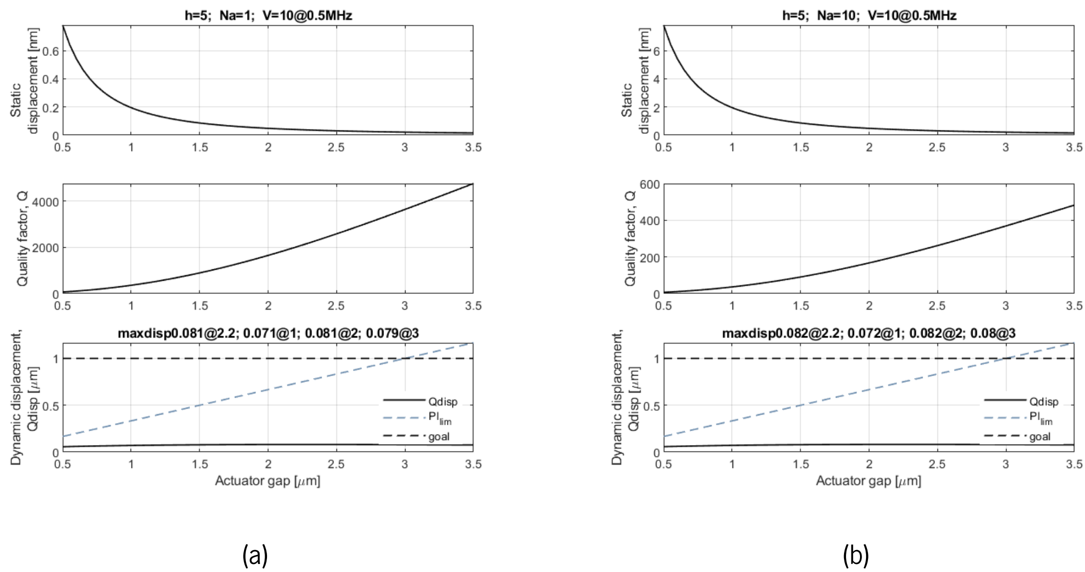

(a) (b)

Figure 4.3: Influence of the number of actuators on the dynamic displacement.

Where h is the thickness of the device layer, Na is the number of actuator plates on a single side, and V is the actuation voltage. By comparing (a) and (b), the most notable differences are in the decrease in quality factor values with the increase of damping, and the static displacement, which increases with the electrostatic force. More or less, the dynamic displacement stays the same.

Height - device thickness

Another aspect to consider is the thickness of the device layer, if the layer thickness is reduced, the structure mass and spring stiffness decrease; the damping coefficient decreases as plate area is reduced, making it so that the quality factor increases. The static displacement stays more or less the same, but the increment in quality factor increases the dynamic displacement with it.

Figure 4.4 are the resulting plots when the height is 3 μm and 2 μm.

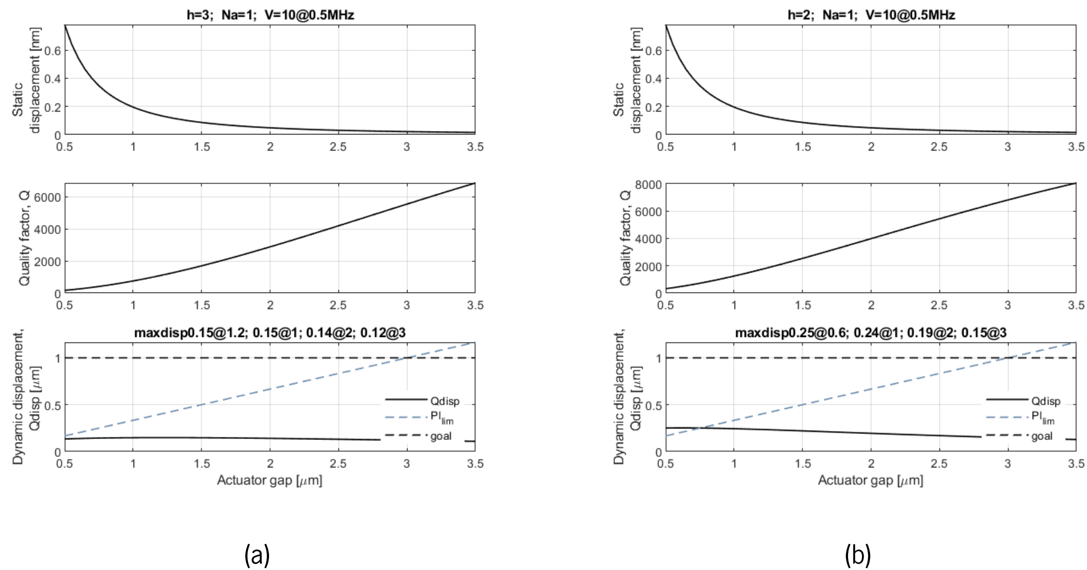

(a) (b)

Figure 4.4: Influence of the thickness of the device layer on the dynamic displacement.

Figure 4.4 (a) is when the thickness of the device layer is set and 3 μm and (b) when it is 2 μm. Other parameters are kept constant between runs. By comparing figure 4.3 (a) and both plots in figure 4.4, it is noticeable the increase in the maximum dynamic displacement. For an actuator gap of 1 μm, the maximum displacement when the height is 5 μm is 0.071 μm; when the height is 3 μm, the maximum displacement is 0.15 μm, and when the height is 2 μm the maximum displacement is 0.24 μm.

Actuation voltage

The direct influence of the actuation voltage in the displacement is also considered. The increased values of voltage lead to more displacement, although in some cases is not as beneficial as the displacement happens above the pull-in limit.

Figure 4.5 is the corresponding displacement when the actuation is set at 15V and then at 20V. Both outputs are also comparable with figure 4.4 (b).

The variation of the actuator plates gap is also depicted in the graphic plots where the distance varies from 0.5 μm to 3.5 μm. As the actuator plates gap decreases, the damping increases and the quality factor decreases; maintaining both mass and stiffness coefficient, the elastic force is kept the same; the electrostatic force increases with the smaller gap making it so that the static and dynamic displacements increase slightly. The change in the dynamic displacement values as the actuator gap increases is more noticeable when the actuation voltage values increase.

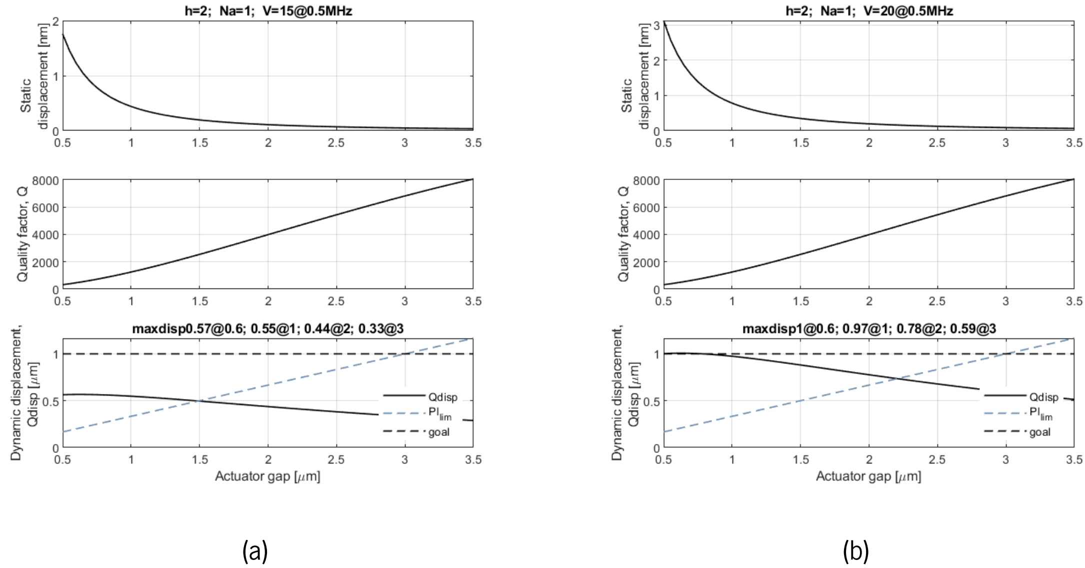

(a) (b)

Figure 4.5: Influence of the actuation voltage on the dynamic displacement.

4.1.2 Influence of geometry on the displacement in CD type of structures

Considering a CD-type structure with a grid area of 100x100 μm^2, a spring width of 3 μm, a resonance frequency of 2 MHz and combs distributed equally on each side of the movable mass. The spring length is calculated using the elastic spring model present in 3.3, and the results are computed using the system equations. Table 4.2 presents the geometrical parameters used for the simulation.

Table 4.2: Initial simulation parameters for CD type structures.

Parameter	**Value**	**Unity**
Spring width, ws	3	μm
Spring length, ls	42.4	μm
Grid length, lg	100	μm
Height, h	2	μm
Grid beam spacing, sg	1	μm
Grid beam width, wg	1	μm
Applied voltage, V	10	V
Comb width, wa	3	μm
Comb length, la	5	μm

Number of combs

The number of combs is considered. If the number of combs in the movable structure increases, the electrostatic force and static displacement both increase as per the equations mentioned in 3.2.2.

While maintaining the remaining parameters and increasing the number of comb pairs in the structure, the results can be seen in figure 4.6. To notice that the dynamic displacement is the same. Although the static displacement increases, the quality factor is less due to the increase in damping.

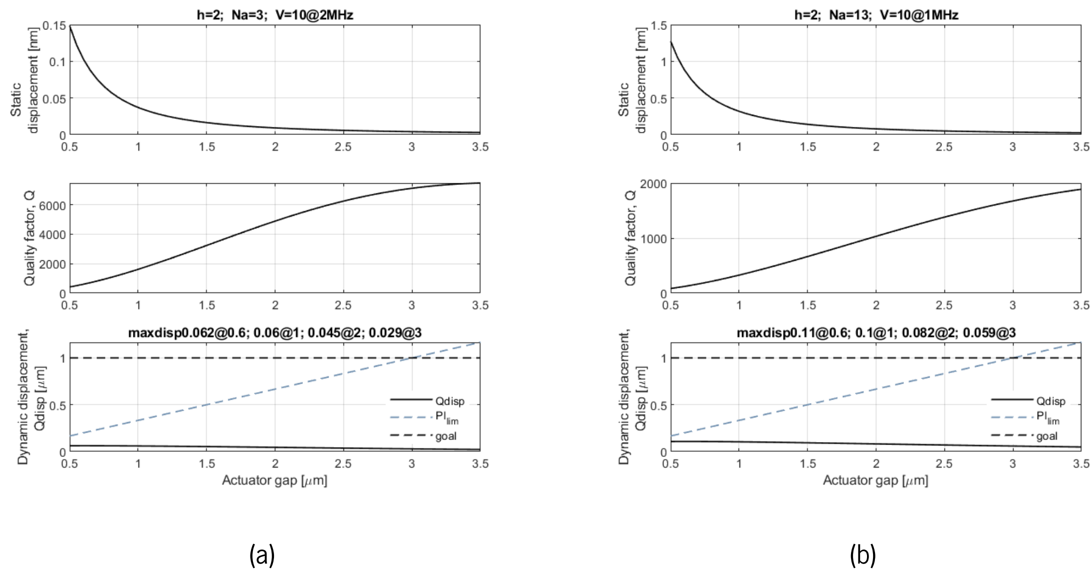

Figure 4.6: Influence of the number of combs on the dynamic displacement.

4.2 FEM Evaluation

The Finite Element Model (FEM) application for modelling and simulating different physical phenomena in interconnect structures by using COMSOL Multiphysics is discussed here. The finite element analysis is performed by building the model (creating the geometry to represent the domain under study and assigning the material properties to the domain). Then, the physical environments of the problem under investigation are generated by assigning the underlying physics (or multiphysics), mathematical equations, and finite element formulation to the model.

A FEM model and simulation aims to represent complex electromechanical phenomena through theoretical mathematical models, describing them by equations and solving, which provides the physics-related solutions of the model. Several FEM simulations were performed in the COMSOL Multiphysics software to evaluate the behaviour of the designed actuator.

4.2.1 Resonance Frequency (Eigenfrequency Simulation)

Eigenfrequencies or natural frequencies are certain discrete frequencies at which a system is prone to vibrate. An eigenfrequency analysis can only provide the shape of the mode, not the amplitude of any physical vibration. So, through the modal analysis, it is possible to determine the vibration characteristics of each structure and the corresponding mode shape.

The parameters and respective values considered for the Eigenfrequency simulation are a grid length of 100 μm, spring width, w$_s$ of 3 μm and height of 2 μm.

The resonance frequency established in the analytical model is either 0.5MHz or 2MHz, and the spring's length and respective stiffness were computed in regard to the pre-established frequency values. Therefore, the FEM Eigenfrequency simulation studies the model's resonance frequencies and the correspondence to the equivalent mode shapes of each frequency.

The simplified model for the modal and structural analysis is depicted in figure 4.7.

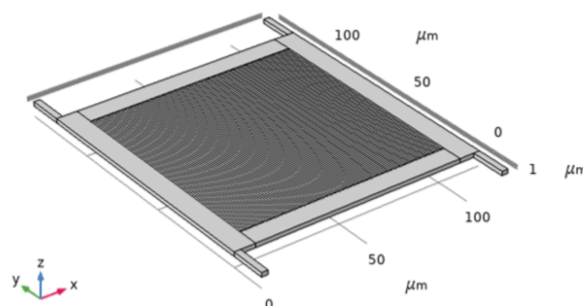

Figure 4.7: Simplified model for the modal and structural evaluation.

For a parallel plate actuator, the mass of the movable mass is 48.9 pg and the spring stiffness computed is 7300 N/m and length 17.1 μm when the desired frequency is 2 MHz; and 462.35 N/m and length 42.9 μm when the frequency is 0.5 MHz. When needed, the features were adapted accordingly.

First, for a spring length of 17.1 μm and a stiffness coefficient of 7300 N/m, the table 4.3 shows the Eigenfrequency study results for six different modes and respective frequencies and behaviour descriptions. Figure 4.8 are the Eigenfrequency mode plots for l_s 17.1 μm.

Table 4.3: Eigenfrequency study results when ls=17.1 μm and k=7300 N/m.

Mode	**Freq. [MHz]**	**Description**
1	0.50457	out of plane
2	0.93961	out-of-plane y-rotation
3	1.0561	out-of-plane x-rotation
4	1.3312	out-of-plane x-y
5	2.0586	in-plane
6	2.1612	out-of-plane x-y 45°

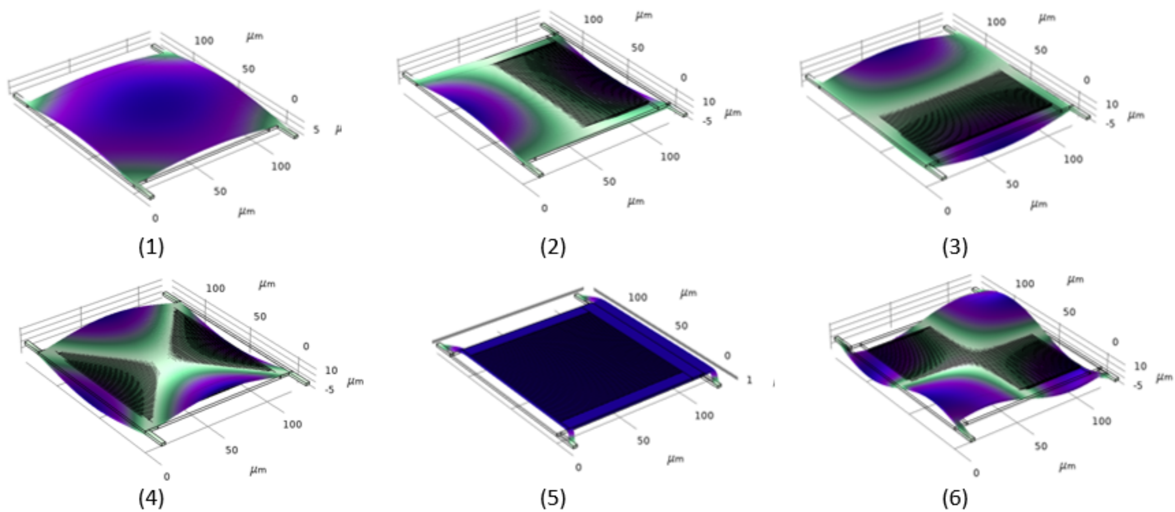

Figure 4.8: Eigenfrequency mode plots for l_s=17.1 μm.

For a spring length of 42.9 μm and a stiffness coefficient of 462.35 N/m, the results are depicted in table 4.4.

Table 4.4: Eigenfrequency study results when l_s=42.9 μm and k=462.35 N/m..

Mode	Freq. [MHz]	Description
1	0.29608	out of plane
2	0.50893	out-of-plane y-rotation
3	0.56578	in-plane
4	0.64752	out-of-plane x-rotation
5	1.2676	out-of-plane x-y
6	1.2896	out-of-plane x-y 45°

The Eigenfrequency simulation for the two spring lengths is represented, and it is possible to conclude that the in-plane vibration mode frequency is set near the pre-established value. The correspondent mode shape of the resonance frequency is essential in evaluating the devices since the goal is to achieve an in-plane movement.

4.2.2 In plane displacement and stress (static structural simulation)

A set of structural simulations were performed to estimate the in-plane displacement and stress induced on the springs. In this model, the conditions implemented were a boundary load with the same value as the electrostatic force computed in the analytical analysis and the fixed supports on the edge of the springs, figure 4.9.

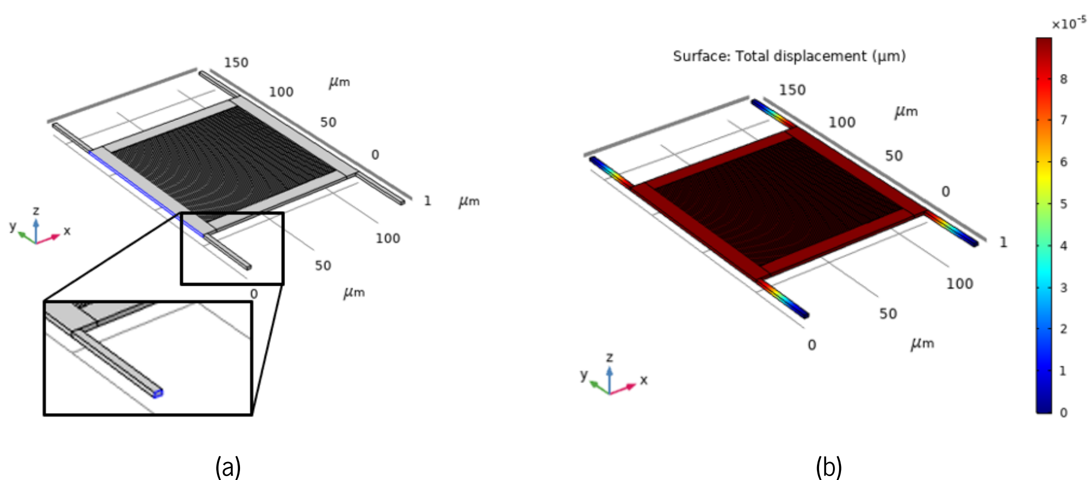

Figure 4.9: Boundary load and fixed constraints (a) and displacement in x direction evaluation (b).

This way, a horizontal force with the same value as the electrostatic force calculated in the analytical

evaluation was applied to assess the in-plane displacement. The elastic coefficient was also defined with the computed analytic value, and the resulting displacement was then compared with the Matlab values.

For a spring length of 49.2 μm with a stiffness of 462.35 N/m, the computed Matlab static displacement is 24.1 pm, where the displacement in the FEM evaluation is 17.4 pm. The results are a close approximation, and the small difference can be derived from the mesh defined in the simulation and the fact that the simplified model does not have the metal grid.

When a force is applied to an object, the object will either compress or stretch in response to that force. Figure 4.10 is obtained through structural simulation of the stress intensity.

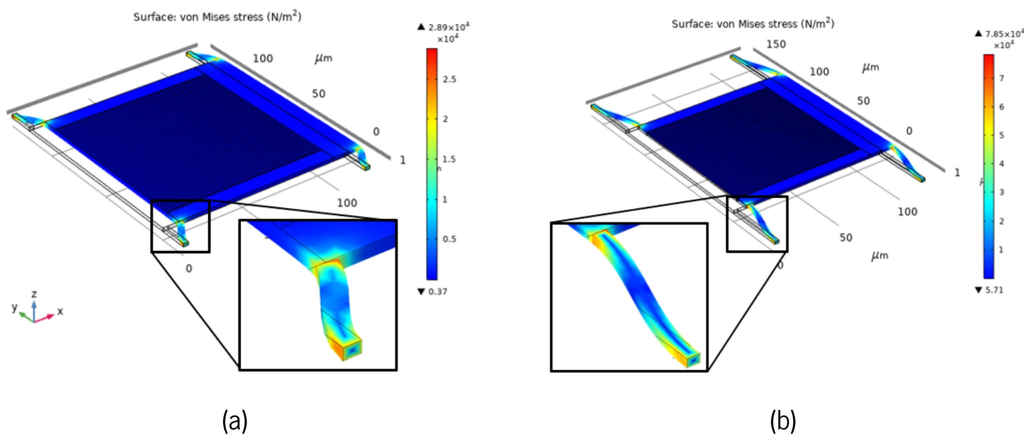

(a) (b)

Figure 4.10: Stress on a spring with 17.1 μm length (a) and 49.2 μm length (b).

In structural terms, the points where the stress intensity is higher are the anchor points of the springs and their segments, which, in turn, are the most critical points of the structure.

The deformation of an object typically presents three distinct stages: elastic deformation, plastic deformation and rupture. Elastic deformation disappears upon removal of the external forces causing the alteration and the stress associated with it and is reversible. Plastic deformation is a permanent deformation in the shape of a solid body without fracture under the action of a sustained force and is irreversible. Typically, the point of non-return of silicon deformation exists when the induced stress is higher than 1 GPa (1 GN/m^2) [33].

For a 17.1 μm spring length, the maximum stress point is 28.9 kN/m^2 and for a spring length is 78.5 kN/m^2, so the deformation is reversible. The design was adjusted to reduce the stress at the anchor spring points, and instead of a 90-degree angle, the connection points between the spring and the movable structure were filled.

4.2.3 Thermal Deformation

As a solid material experiences an increase in temperature, the volume of the structure is ultimately impacted by increasing. This process results from heat increasing a material's kinetic energy.

Within solids, molecules are typically located in close proximity to one another, contributing to the defined shape of the structure. As the temperature rises, molecules begin to vibrate more rapidly and push away from one another. This increased separation between the individual atoms causes the solid to expand, thus increasing the volume of the structure.

To attest to the deformation of the structures at different temperatures there was conducted a thermal variation and studied to if it would lead to any deformation. The range of temperatures was from 283.15 K to 313.15 K with an increment of 5 degrees. From the results, it is possible to verify that the temperature is the same across the structure. Moreover, the results show that below 288.15 K, the structure contracts and the stress is progressively higher as the temperature decreases. The structure expands for temperature values above 298.15 K, and the stress increases with the temperature. For a temperature of 293.15 K, there is no deformation. Figure 4.11 is the deformation stress when subjected to a temperature of 288.15 K (a) and 298.15k (b).

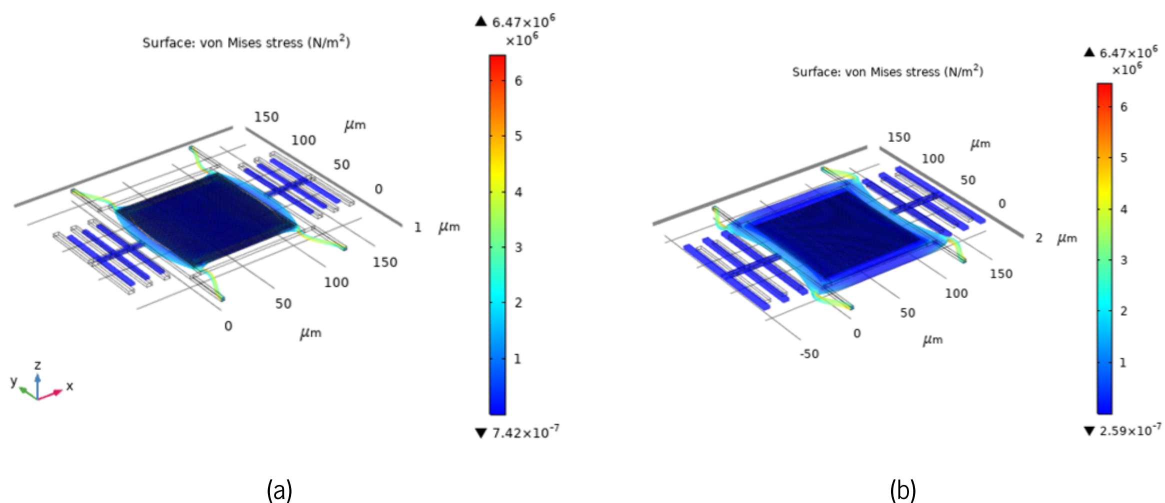

(a) (b)

Figure 4.11: Stress deformation at 288.15 K (a) and 298.15k (b).

This simulation was performed for multiple parallel plate structures, but since the deformation is concentrated in the springs, this is valid for all structures.

4.3 Designed MEMS Structures

In the previous sections, the analytical and FEM evaluations of the MEMS modulator were described. The MEMS structure will now be presented considering the results obtained previously. Figure 4.12 is the 3D model developed using the Rhinoceros CAD software of one die with ten different structures. The metal layer is represented in lighter grey, the device layer is depicted in medium grey, and the handle is dark grey.

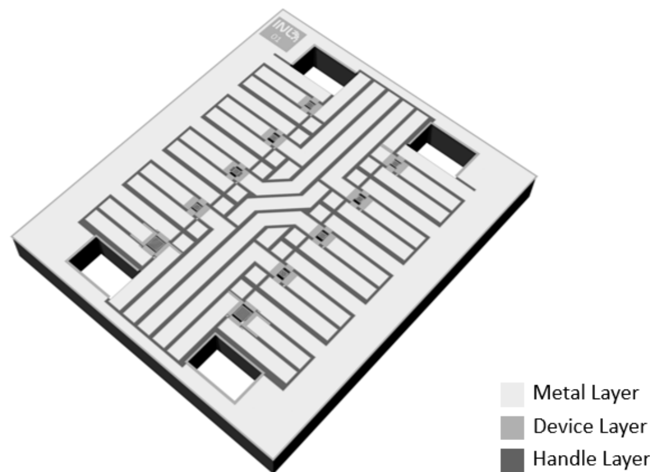

Figure 4.12: Die 3D Model design.

Each die has an area of 7.5x6.5 mm^2, and the ten structures with differences between them regarding their respective layout features: grid dimension, spring geometry and actuator type. The table 4.5 compiles the values for the ten structures, and the spring length is computed using the system model.

Table 4.5: Layout dimensions of the ten structures.

Parameters	**S01**	**S02**	**S03**	**S04**	**S05**	**S06**	**S07**	**S08**	**S09**	**S10**
Grid dimension [μm^2]	100x100								200x200	
Spring Length [μm]	17.1	17.1	42.9	42.9	38.8	42.4	17.1	42.8	11.7	29.4
Spring Width [μm]	3									
Type of actuator	Parallel Plates					Comb Drive				
Number of actuators	2				12	26		6	50	
Gap, d0 [μm]	3	1.3	3	1.3	1.3	1				

The MEMS structures developed in this dissertation were fabricated in an SOI wafer with a device layer of 5 μm thickness, a buried oxide layer of 2 μm thick and a handle layer of 650 μm. Although the

thickness of the device layer will be adjusted to a thickness closer to 2 μm.

The ten different layouts were designed, and the actuation is accomplished through a parallel plate or comb drive actuation. S01 to S04 are single parallel plate type actuators, S05 is a multiple parallel plate type of actuator and from S06 to S10 are comb drives, figure 4.13.

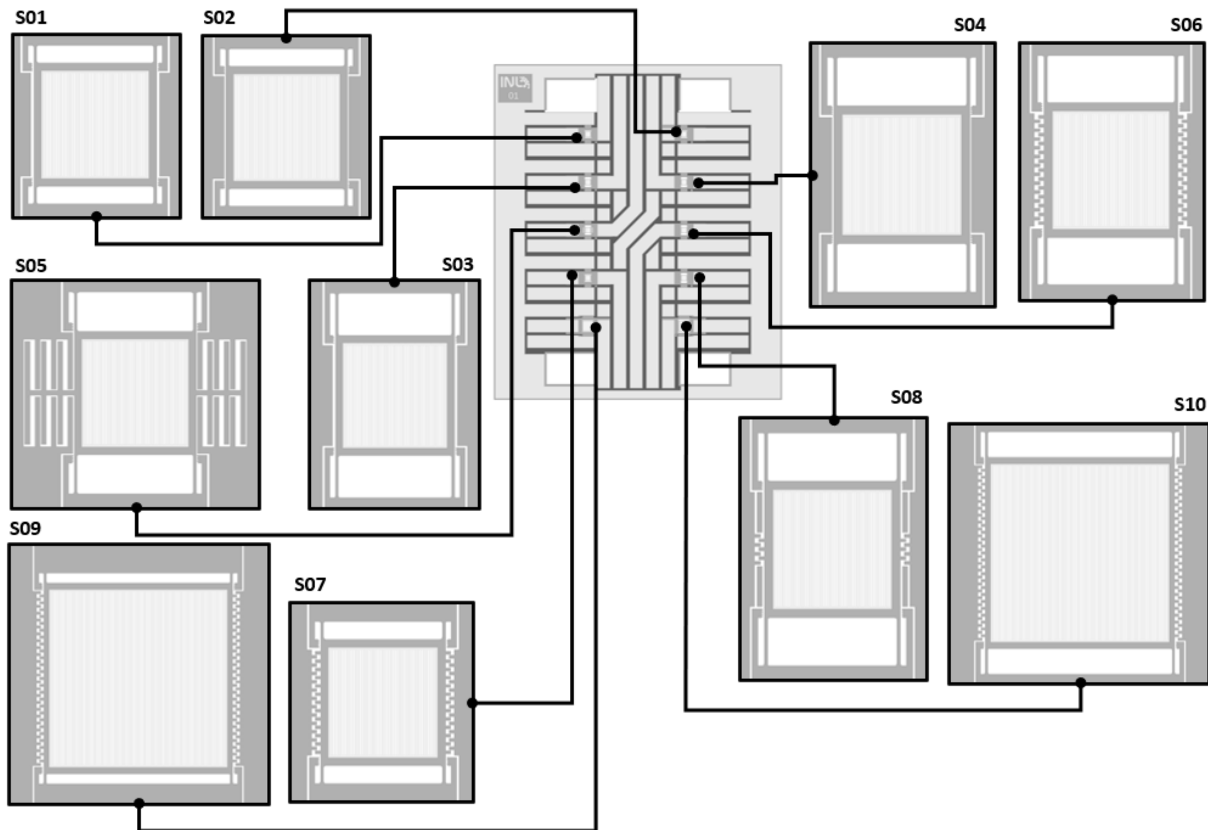

Figure 4.13: Ten different structures and distribution on each die.

From S01 to S04, the differences are the springs' length and the zero displacement gap distance between the actuating plates. These structural differences make the spring stiffness coefficient, capacitance and resonance frequency comparable between them.

Moreover, S05 is the only one with multiple pairs of parallel plates, maximising the structure area as it increases the overlapping area of the actuators. The spring length in this structure was adjusted to accommodate the wanted resonance frequency.

From S06 to S10, there are comb drive actuators. Between S06 and S07, the difference is the spring length leading to different resonance frequencies. S08 has fewer comb pairs; the spring length is adjusted accordingly to maintain the frequency.

The optical modulator grid area is 100x100 μm^2 in all the structures except the last two, which is 200x200 μm^2. S09 and S10 have more comb pairs, and the spring length is adjusted, considering the

desired resonance frequency.

All ten structures have four springs that suspend the movable mass and a stopper to limit its movement. The stoppers avoid possible collisions between the plates, and the bumps are there to avoid sticking.

The contact channels of the actuator with the outside are also included in the die design. This way, there are two contacts, one for the left and the other right side of the actuator and the area surrounded will be the ground.

Figure 4.14 is a closer look at the S05 structure, where there is a modulating grid, four springs and multiple actuating parallel plates on each side of the grid.

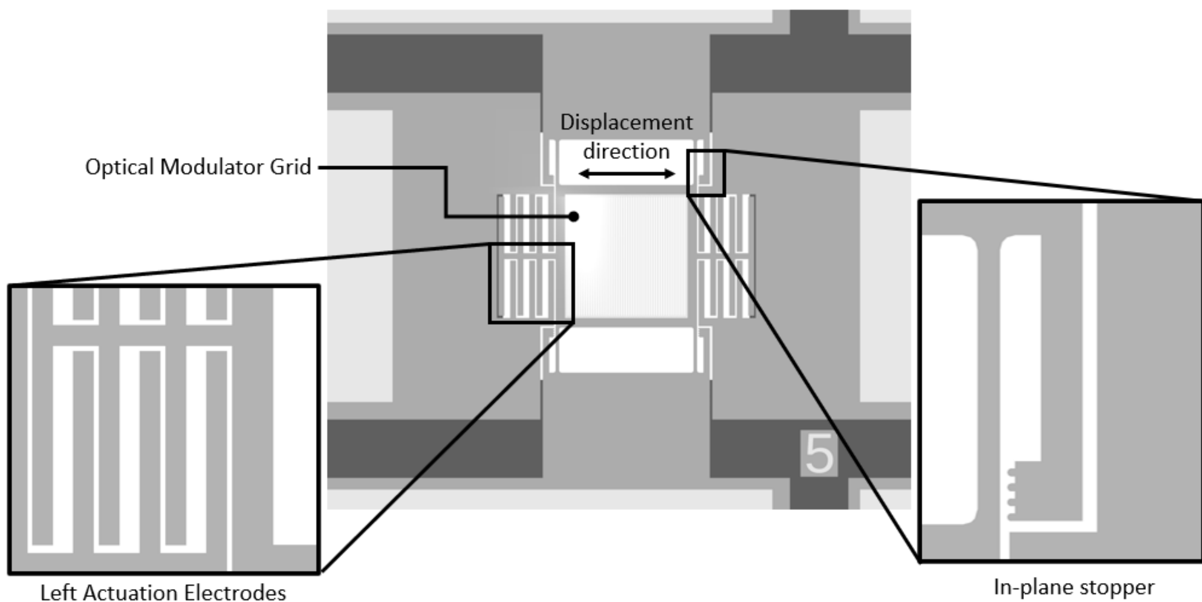

Figure 4.14: Structure 5 layout.

Each structure's mechanical and electrical parameters (stiffness coefficient, quality factor, damping coefficient, resonance frequency, capacitance at zero displacement, and mass) computed in Matlab are present in the table 4.6. These results were simulated for the device layer thickness of 2 μm.

Table 4.6: Electrical and mechanical parameters for each structure.

Structure	k [N/m]	Q	b [nN.s/m]	f0 [MHz]	C0 [fF]	m [pg]
S01	7300	7164.2	81.1	1.99	0.602	46.2
S02	7300	7164.2	81.1	1.99	1.39	46.2
S03	462.35	1181.7	81.1	0.499	0.602	46.9
S04	462.35	1181.7	81.1	0.499	1.39	46.9
S05	624.95	476.4	423.2	0.493	33.43	65.02
S06	478.9	4718.9	33.5	0.482	23.48	52.1
S07	7300	18233	32.5	1.96	23.48	48.1
S08	465.6	7541.8	19.7	0.498	0.071	47.4
S09	22792	28708	64.1	1.97	59.03	148.4
S10	1436.5	7219.2	64.1	0.494	59.03	148.9

4.4 Conlusions

This chapter presents the numerical analysis and FEM modelling and simulation. The analytical evaluation defined and computed the overall parameters that constitute the modulator layout and design.

The parameters that influence the dynamic displacement of the modulator were studied to extract the layout features. The number of actuator plates, the thickness of the device layer and the actuation voltage influence the dynamic behaviour of the device.

Regarding the FEM evaluation, the simulations focused on the structural behaviour of the device, such as resonance frequency, in-plane displacement, deformation of the springs and their induced stress.

This way, the Eigenfrequency simulation studies the natural frequencies of the designed device and correspondence to an in-plane movement at the stipulated resonance frequency. In addition, the in-plane amplitude displacement is comparable between both analytical and FEM evaluations, allowing for the analytical model's validation.

Chapter 5

Microfabrication

Microfabrication or MEMS fabrication defines a series of techniques that can modify a substrate material in an additive (surface) or subtractive (bulk micromachining) manner to convert a thin, generally planar substrate into a complex structure of multiple materials. Additive processes allow the deposition of thin layers of materials into a substrate through physical or chemical deposition techniques. Subtractive processes involve selective etching or erosion of regions of the structure through wet or dry processes. Microelectromechanical system devices are therefore constructed through a combination of micromachining and compatible thin-film deposition techniques that evolve the desired structure from an initial substrate [34].

This chapter will present the study and evaluation of the device's micromachining process and the INL Standard process in manufacturing SOI (Silicon on Insulator) based MEMS.

5.1 MEMS Modulator Process

SOI substrates have become a vital part of Si technology and are most common in microelectromechanical systems (MEMS) and advanced complementary metal–oxide–semiconductor (CMOS) integrated circuit fabrications. From their roots as specialised wafers for niche applications, SOI wafers have moved to the mainstream, providing significant enabling enhancements in circuit performance, such as reducing power and heat while increasing speed [35].

SOI wafers are unique products for specific end-user applications. Silicon-on-insulator wafers are a three-layer material stack composed of a device layer of silicon, a buried oxide layer (BOX) of electrically insulating silicon dioxide, and a bulk silicon support wafer (handle).

In this case, the fabrication process begins with a 200-mm-diameter single-side polished SOI wafer

where the device layer is 5 μm thick, the BOX 2μm, and the handle layer is 650 μm thick.

The device layer is also called the active layer since it is where the electrostatic structures are defined. Moreover, to facilitate wafer handling during the manufacturing process, the device layer is referred to as the front side (FS), and the handle layer corresponds to the back side (BS), figure 5.1.

Figure 5.1: SOI Wafer cross-section.

5.1.1 MEMS Standard Micromachining Process

The micromachining process available at INL is an in-house process, meaning it is not a commercial process, which allows the implementation of changes or slight variations whenever necessary and within the limits of the same. Figure 5.2 depicts the main process steps of the micromachining process.

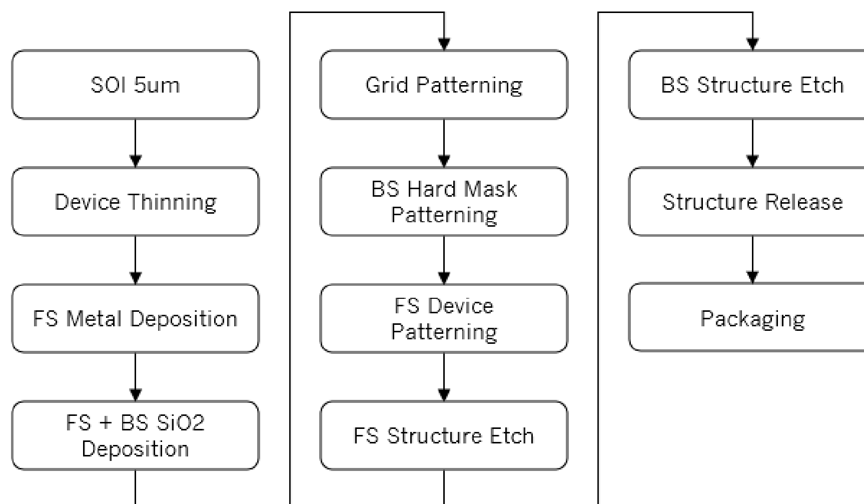

Figure 5.2: Microfabrication process used.

The process includes patterning alignment marks in the FS and BS, reducing potential misalignments while patterning the wafer. Accordingly, alignment marks were carved into both sides of the wafer to provide a better guideline for each of the three masks.

The use of polymers was introduced in the manufacturing process. The first, PMMA, is used as a mask layer for the front-side device layer patterning. Polyimide is the alternative used instead of thermal

tape, whose utility is to ensure that there is no damage to the device layer when etching the handle layer. This way, the polyimide removes the possible mechanical damage caused by applying the thermal tape.

The main steps cross sections of the process are shown in figure 5.3, where: (a) Device Layer Thinning; (b) FS Metal deposition; (c) FS and BS SiO2 Deposition; (e) Grid Patterning; (f) BS Hard Mask Patterning; (g) FS Device Patterning; (h) FS structure etch, device layer etch; (i) BS structure etch, handle layer etch; (j) Structures release, using HF vapour etching.

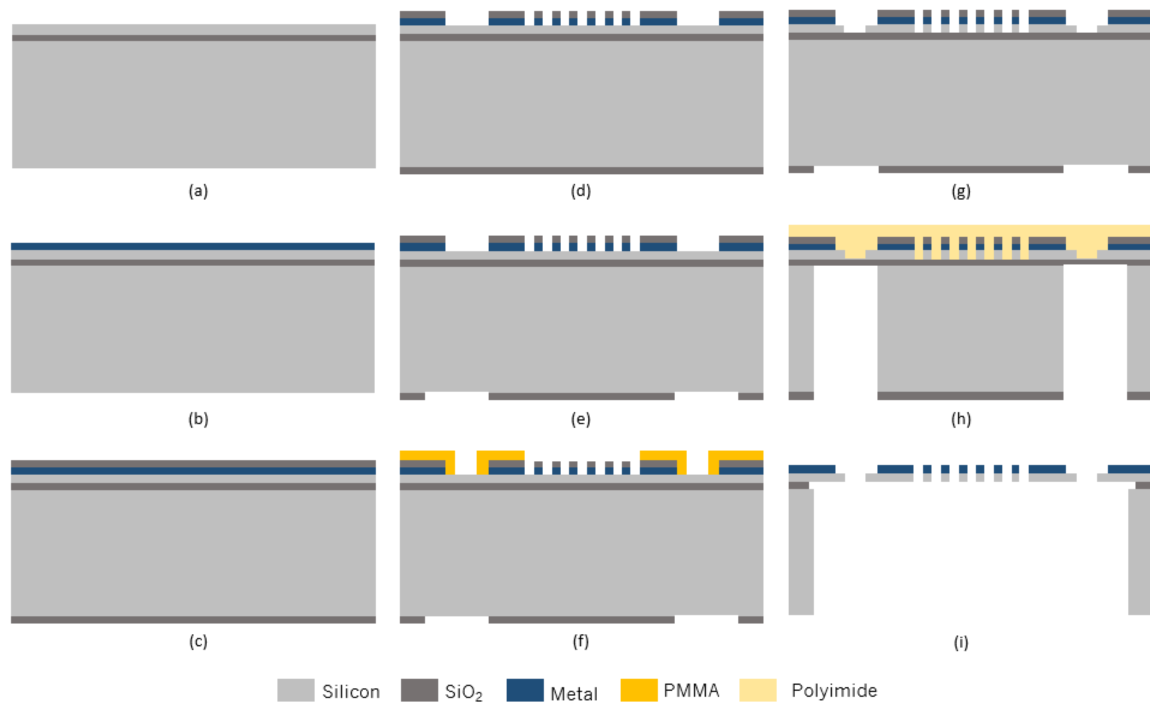

Figure 5.3: Main fabrication process steps.

The silicon layers are depicted in grey, the oxide in dark grey, the metal layer is represented in dark blue, and the polymers, PMMA and polyimide, are represented by orange and yellow, respectively.

5.2 Devices Distribution on the SOI Wafer

During the microfabrication process, it is essential to have the projected devices organized along the wafer. Thus, the mask was divided into smaller sections. At the same time, the maximization of the wafer's area and the behaviour and exposure time of the equipment used for the lithography process were kept in mind.

Therefore, the wafer is divided into 27 cells, named reticules. Each reticule comprises 8 dies, each of which has 10 structures. Upon characterization, these structures will have a nomenclature system namely CXXDYYSZZ, where XX is the number of the cell, YY is the number of the die and ZZ is the number of the

structure. The division and distribution were previously done on Klayout EDA Tool and then introduced in the lithography system. The final device distribution is in figure 5.4.

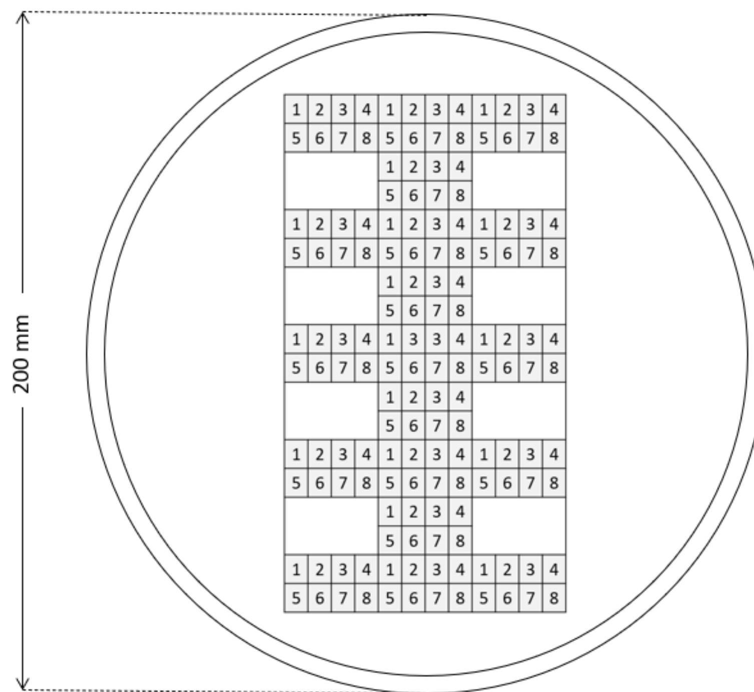

Figure 5.4: Devices distribution on SOI wafer.

The layout includes structures with different types of actuator sizes, different release approaches, and different metal contact layouts. Therefore, the 8 dies are distinguished in relation to:

- Die separation, related to the die release approach, means that the BS trench dedicated to separating the die can be with or without a bridge. If there is a bridge, the BS trenches are separated by a 20 μm gap;
- The aluminium connections referred to the approximation of the metal layer to the device structure. When there are full aluminium connections, it means that the metal layer follows the silicon almost to the end of the silicon layer;
- Horizontal bars were added to the grid structure so that the structural integrity of the grid is kept in case of breakage;
- The grid dimensions related to the beam grid spacing can be distinguished, and it can be either 1 μm lines and 1 μm gaps or 1.2 μm lines and 0.8 μm gaps.

The table 5.1 translates the differences between dies and their respective characteristics.

Table 5.1: Die ID matrix.

	Die separation	Continuous SOI over BS trench without bridge		Continuous SOI over BS trench with bridge	
	Aluminium connections	None	Full	None	Full
	Horizontal bars	N	Y	Y	N
Grid Dimension	1 µm lines, 1 µm gaps	1	2	3	4
	1.2 µm lines, 0.8 µm gaps	5	6	7	8

5.3 Device MEMS Modulator Micromachining Process

5.3.1 Device Thinning

The micromachining process starts with a device layer thinning achieved by the etching of the device layer in some steps on SPTS PEGASUS Deep Silicon Etcher, a system dedicated to deep reactive ion etching (DRIE) of silicon. Using OPM Nanocalc Optical Profilometer - Interferometer to monitor the thickness of the device layer before and between each etch step. The measurement principle of the Nanocalc consists of having a light source that illuminates vertically a thin layer and a spectrometer that measures the reflected light as a function of wavelength. This way, the Nanocalc software can extract the thickness of the layer.

Initially, the SOI wafer was inspected, and the results show an average thickness of 4820.725 nm, maximum and minimum are 4529.3 nm and 5031.1 nm, respectively, as shown in the figure 5.5.

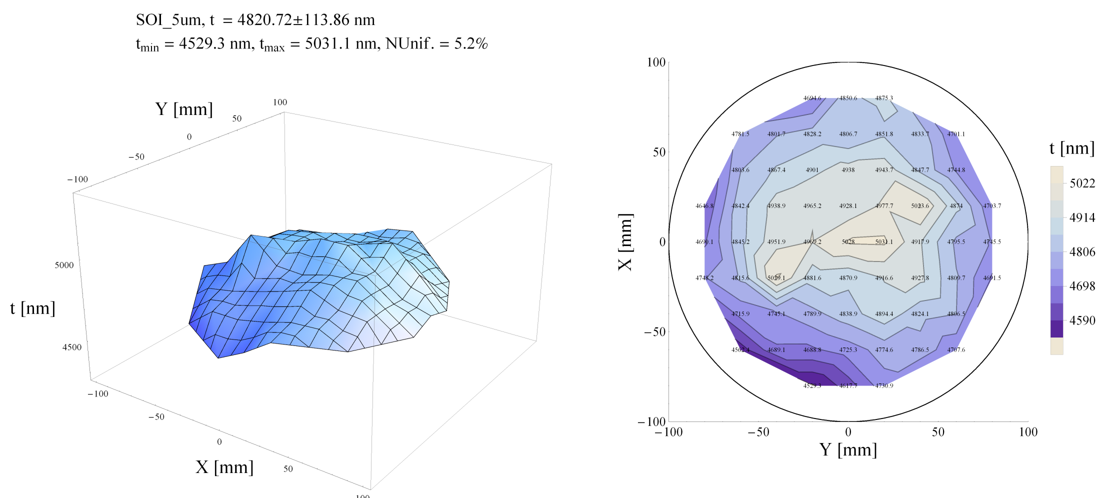

Figure 5.5: Device layer thickness, Nanocalc.

Since the device layer thickness is not homogenous, the silicon etch was accomplished in four steps,

followed by Nanocalc measurements. The thinning of the device layer is concluded when the minimum thickness part is considered close enough and does not risk damaging the wafer. In this process step, the goal is to reduce the thickness of the device layer from 5 μm to a thickness between 2 μm and 3 μm.

Table 5.2: Nanocalc results.

Process Step	Mean	Max	Min	Removed [nm]	ER [nm/min]
PS01.0 - Before Thinning	4820.725	5031.1	4529.3	-	-
PS01.1 - 4 DRIE Cycles	4209.254	4379.8	4017.2	611.4704918	1864.2393
PS01.2 - 4 DRIE Cycles	3578.439	3746	3437.9	630.8147541	1923.21571
PS01.3 - 4 DRIE Cycles	2966.513	3263.7	2761.1	611.9262295	1865.62875
PS01.3 - 2 DRIE Cycles	2665.15	3139	2446.3	301.3631148	1837.57997

Table 5.2 depicts the details of the Nanocalc inspection between each of these runs. The thinning process is concluded, and the device layer thickness is, on average, 2.665 μm.

5.3.2 FS Metal Deposition

The next step is sputtering metal on the FS of the wafer, which is accomplished with the Singulus Timaris FTM system. Metal deposition by sputtering is a plasma-based deposition process in which energetic ions are accelerated towards a target. The ions strike the target, and atoms are ejected (or sputtered) from the surface. These atoms travel towards the substrate and incorporate into the growing film.

The material to be deposited is TiW/ AlSiCu / TiW with a ratio of 15nm / 250nm / 15nm. The stack of metals works so that the first TiW layer ensures better adhesion of the AlSiCu to the device layer, and the second one protects the AlSiCu layer from the following lithography, this way behaving as a mask and sacrificial layer to the AlSiCu. The metal layer will be on top of the grid and is also responsible for the electrical contacts.

5.3.3 FS + BS SiO2 Deposition

After the deposition of the metal on FS, the next step is to deposit a layer of SiO2 on both the front and back sides on the SPTS CVD system.

Plasma-Enhanced Chemical Vapor Deposition (PECVD) is a variation of chemical vapour deposition (CVD) that uses plasma instead of heat to activate the source gas or vapour. Plasma in vapour deposition processes is typically generated by applying a voltage to electrodes embedded in a gas at low pressures.

PECVD systems can generate plasma by different means, e.g., radio frequency (RF) to mid-frequencies (MF) to pulsed or straight DC power. Whichever frequency range is used, the objective remains the same: the energy supplied by the power source activates the gas or vapour, forming electrons, ions, and neutral radicals. These energetic species are then prime to react and condense on the surface of the substrate. The coating's growth rate is relatively constant, so its thickness is proportional to the deposition time.

With the deposition rate of SiO2 known and by altering the time it is deposited a layer with 0.1 μm on the FS and on the BS 1 μm. The BS has already a layer of SiO2 with 2 μm thickness.

5.3.4 Grid Patterning

The lithography process for the grid patterning happened in the following order: vapour prime followed by spin coating, then MA exposure and respective development, and next was the DWL exposure and development.

Lithography Process

Photolithography is the process that defines and transfers a pattern onto a thin film layer on the wafer. In photolithography, a light source is typically used to transfer an image from a patterned mask to a photosensitive layer (photoresist or resist) on a substrate or another thin film. This same pattern is later transferred into the substrate or thin film (layer to be etched) using a different process called etching.

In the most general form, the following steps create this method:

- Vapour Prime - This step prepares the wafer for the photoresist by providing a clean surface coated with an intermediate chemical (such as HMDS or Hexamethyldisalizane. This creates a hydrophobic surface which boosts the adhesion of the photoresist to the wafer's surface.

- Spin Coating - The coating process is the application of a photoresist to the wafer's surface using the Karl Suss Optical Track System. The goal of the coating process is to distribute a uniform thickness of the resist across the wafer's surface with the desired thickness. The resist must be thick enough and durable enough to withstand the following process steps, and it must also be uniform to prevent problems during the exposure process.

- Exposure - Using the MA (Mask Aligner) or the DWL (Direct Writing Laser). During exposure, the photoresist layer is exposed when ultraviolet (UV) light from a source travels through the mask to the resist, exposing the resist.

- Development - In the development process, portions of the photoresist are dissolved by a chemical developer using the Karl Suss Optical Track System; With positive resist, the exposed resist is dissolved while the unexposed resist remains on the wafer; With negative resist, the unexposed resist is dissolved while the exposed resist remains.

- Optical Inspection - Using the Optical Microscope, the wafer is inspected immediately after the photolithography process and before subsequent processes such as etching. The inspection specifications vary depending on the product requirements (alignment, critical features, defects).

Alignment Marks

One of the critical features of the fabrication of the devices is the alignment between the front and back sides of the wafer and the metal and device masks. Therefore, it was necessary to pattern alignment marks on the FS and the BS to prevent significant discrepancies and have a precise guideline between each patterning layer. It is important that each layer is aligned properly and within the specifications of the previous layers and subsequent layers.

To create the alignment marks was performed lithography on the Mask Aligner System, which is used for photolithography and transfers a pattern from a mask plate to a photoresist coating on a substrate. Then, ultraviolet light is used to expose the photoresist, and the pattern on the mask plate will mask off areas on the wafer that will not be exposed, figure 5.6.

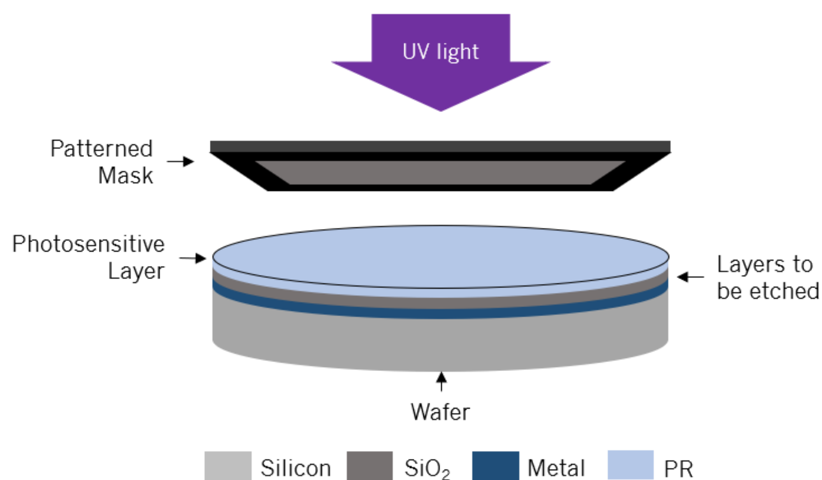

Figure 5.6: Mask Aligner.

A mask, by definition, implies a 1:1 ratio in a mask feature size to wafer feature size. So the mask plate is in direct contact with the wafer during exposure, and alignment can be done by looking through

the mask plate on the wafer. The wafer sits on a movable chuck and can be moved in x, y and θ directions to align existing patterns on the wafer to the pattern on the mask plate.

The mask with the alignment marks has already been developed at the INL, and the layout of this mask is presented in Appendix A - Alignment Marks Mask.

Metal Layer

The DWL is a laser pattern generator that uses a high-resolution laser to expose photoresist for substrate patterning of features. Moreover, the grid patterning consists of the patterning of the metal layer into the wafer, which is accomplished by the lithography process using the DWL.

The wafer is introduced in the DWL, and the alignment marks are the reference point for the first patterning on the wafer. At this stage, to expose the desired pattern, the digital mask containing the metal layer pattern (Appendix B - Metal Mask) will be converted, including the cells already distributed as desired.

In the development process, the PR coated on the FS of the wafer with the first designer-defined mask, portions of the photoresist are dissolved by a chemical developer, and the exposed resist is dissolved while the unexposed resist remains on the wafer, figure 5.7.

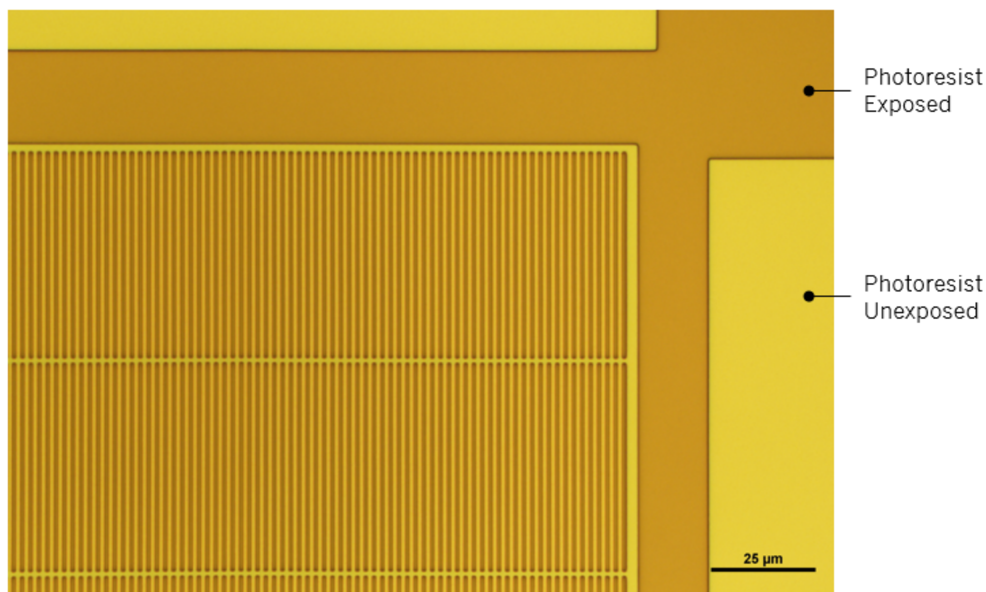

Figure 5.7: Metal layer patterning, OM after development.

After the development of the photoresist on the Karl Suss System, the underlying layers - that now have the first defined mask - will be etched. First, the SiO2 layer etch using the SPTS APS system, and then the metal layer etch using the SPTS ICP system.

Using SiO2 Etch 01, a standard process in the SPTS APS, the SiO2 etch was accomplished using He,

H2, and C4F8-based plasma. Standard processes available on the SPTS ICP system and used during this step are the Main Al Etch responsible for the metal layer etch and the ICP to remove the remaining photoresist. The latest is intended for resist striping and side wall passivation after chlorine-based aluminium etch. The purpose of it is to reduce the post-etch corrosion that substrates suffer in the atmosphere.

Figure 5.8, the grid patterning is accomplished by patterning the resist layer with the first defined mask and subsequently developing (a). Then the SiO2 and Metal etch with the PR removal, (b) and (c), respectively. The OM inspection shows the final result where it is noticed the grid pattern with metal and the exposed device layer where the metal was removed.

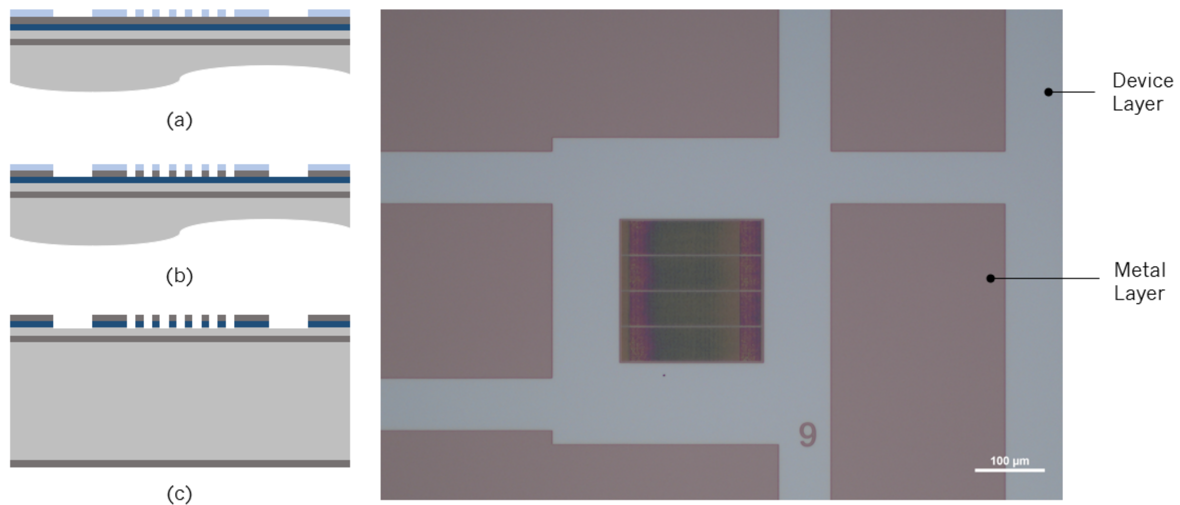

Figure 5.8: Grid patterning, process steps and OM inspection.

Furthermore, the wafer was submitted to the FEI NovaNano SEM system, where it was inspected again, figure 5.9.

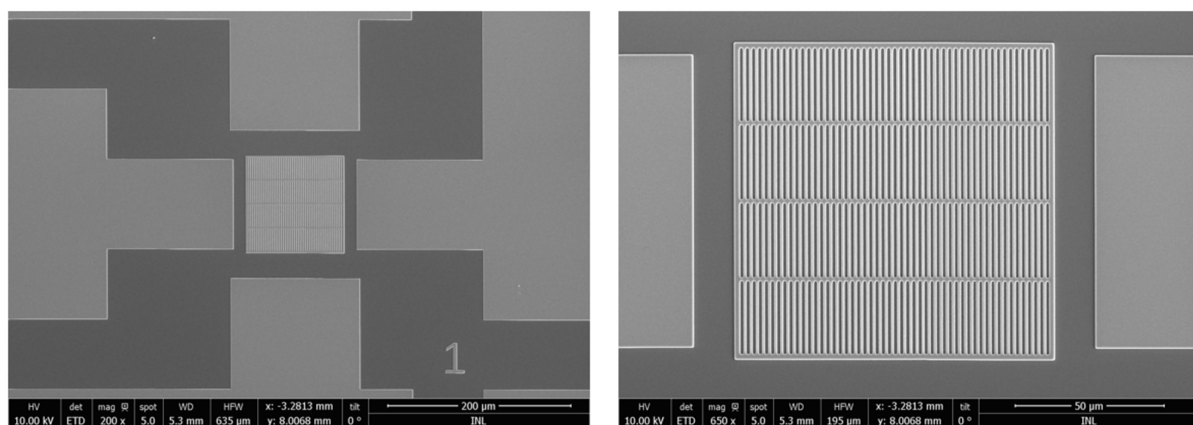

Figure 5.9: Grid patterning, SEM inspection.

5.3.5 BS Hard Mask Patterning

The Mask Aligner System can perform both-side alignment with a second alignment microscope. The same alignment marks (AM) transferred to the FS will be transferred to the BS using the MA.

After the development of the AM on the BS, the wafer is inserted on the DWL system, where the mask containing the BS patterning (Appendix C - BS Mask) is exposed and then developed on Karl Suss, figure 5.10 (a). After the PR is exposed and containing the patterning for the BS trenches, the wafer is transferred to the SPTS APS system where the underlying SiO2 layer is etched, figure 5.10 (b).

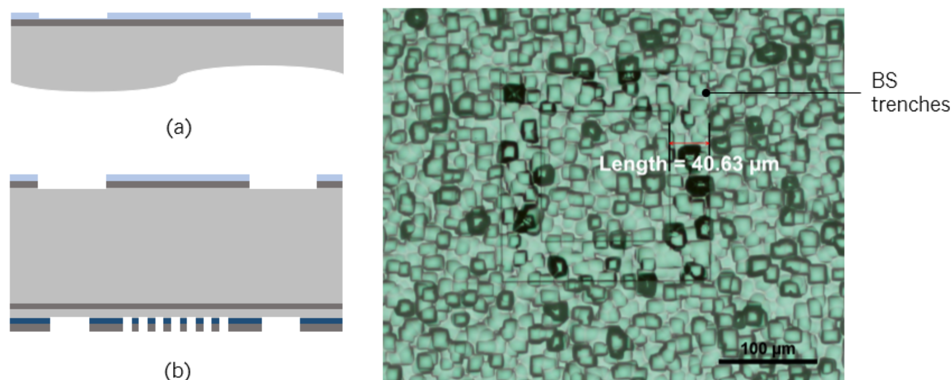

Figure 5.10: BS Patterning, process steps and OM after development on Karl Suss.

The wafer is introduced to the PVA Tepla Plasma Asher system to strip the PR.

5.3.6 FS Device Patterning

The device pattern on the FS starts with Polymethyl Methacrylate (PMMA) coating. PMMA is a polymer with inherent properties like easy availability and temperature resistance that can sustain the anisotropic etchant's action so it is the mask layer for the device layer patterning.

The PMMA is spin-coated on the FS of the SOI wafer on the Karl Suss E-Beam Track system obtaining a 200 nm layer thickness, and then it is vapour primed and spin-coated with the PR before being introduced in the DWL. At this stage, the correct alignment of the wafer is essential so that the grid patterning mask and the device patterning mask (Appendix D - Silicon Mask) positions correspond. Figure 5.11 is the OM inspection after the development of the photoresist. To notice a minimal misalignment, although it is not critical.

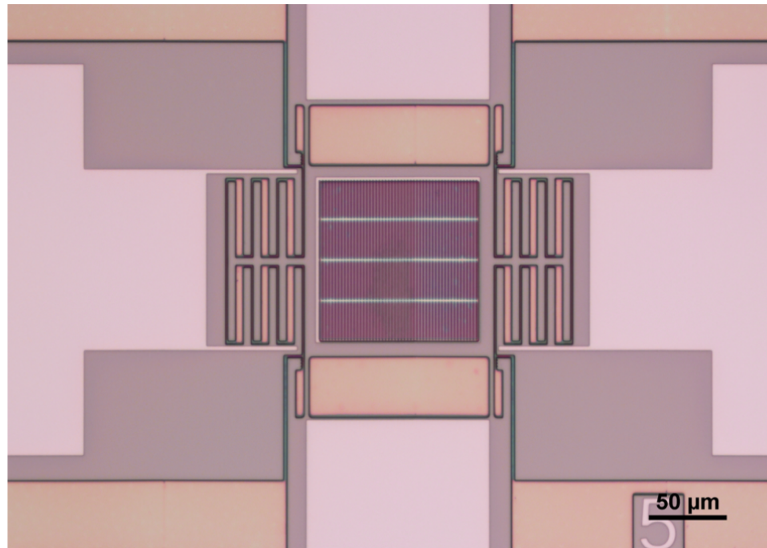

Figure 5.11: FS device patterning, OM after PR development.

After the PR is developed, the subsequent PMMA layer etch is carried out in steps using the Pegasus system. The SPTS Pegasus is a system dedicated to deep reactive ion etching of silicon using the Bosch Process. It can perform anisotropic etching of Si trenches with high aspect ratios and through wafer vias. For that, it uses a switched process by alternated cycles of SF6 plasma etching and C4F8 plasma for polymeric deposition.

Between each step, the posterior OM inspection allows for assessing the PMMA development and whether the gaps have opened. Figure 5.12 depicts the consecutive OM inspections after 15 sec of INL O2 Strip on the SPTS Pegasus system in between each.

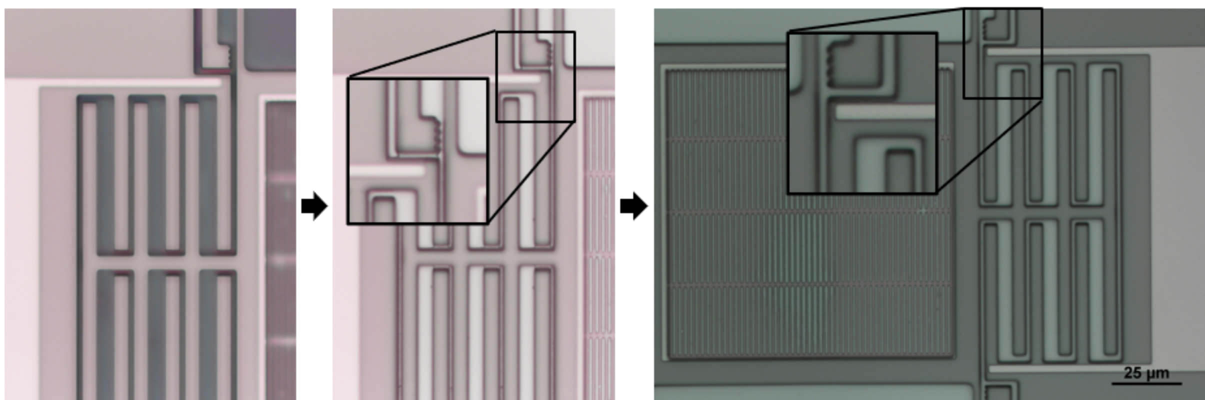

Figure 5.12: FS device patterning gaps, OM inspection.

5.3.7 FS Structure Etch

The structure etch is a critical step in the microfabrication process since it is desired to maintain the integrity of the grid. Therefore, the device layer silicon etch is performed as follows: half of the device layer thickness is etched using the Pegasus system, and the last half is accomplished on the ICP system, all while inspecting the thickness of both silicon and mask layers monitoring its development.

Starting by understanding the depth of PMMA and PR layers is inspected on the Mechanical Profilometer, making it so that the trenches accomplished in the device patterning have an average depth of 1.97μm. This, combined with the Optical Profilometer mapping of the device layer during the thinning of the layer and referring to the table 5.2, its average thickness is 2.665 μm, which is the guideline for the device layer etch. Along the process, the silicon layer depth is inspected in both FEI NovaNano SEM system and Optical Profilometer.

This way, inserting the wafer in the SPTS Pegasus system, through fast Silicon DRIE, with thirty seconds increments, it was etched around 1.6 μm of Silicon, figure 5.13. First after thirty seconds and then after one minute.

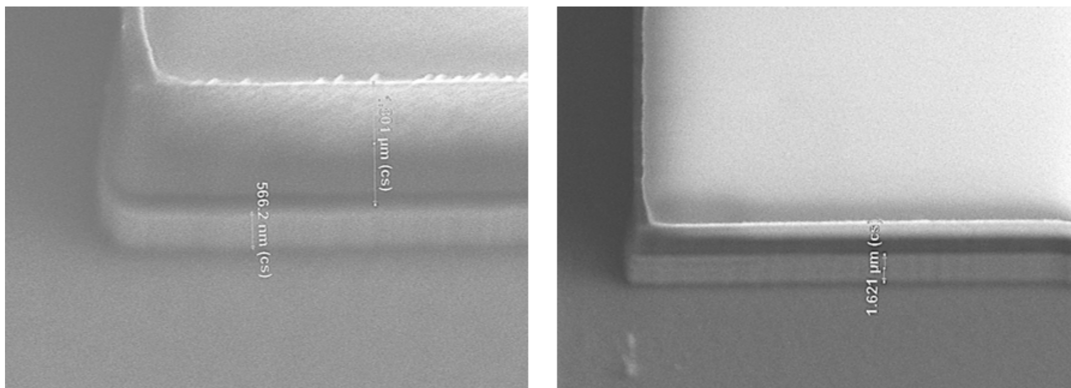

Figure 5.13: Device layer etch, SEM inspection after Pegasus.

The remaining device layer etch is accomplished in the SPTS ICP system with Fast TiW Etch to reduce notching while taking advantage of the etch selectivity, which describes the relative etch rates between the masks used for patterning, PR and PMMA, and the silicon etch rate.

There were performed two ICP runs, and between each run, the wafer was inspected on the OM to verify if either or not the silicon layer trenches were completely etched or if the gaps had opened, figure 5.14. In 5.14 (a), the gaps had not opened, and the silicon is noticeable when compared with the gaps in 5.14 (b). Another way to establish the completion of the structure etch was by using a multimeter and verifying the conductivity of silicon control structures present and distributed on the layout.

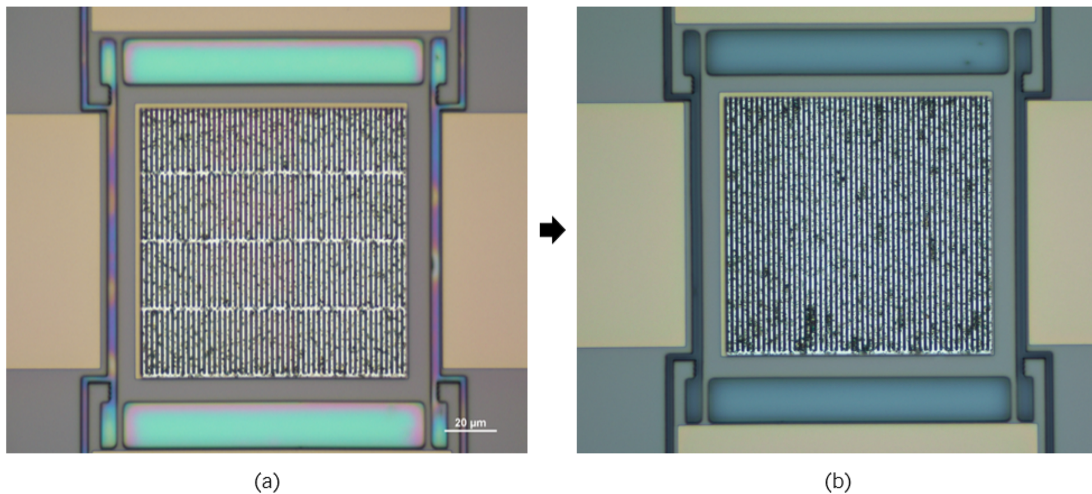

Figure 5.14: Device layer etch, OM inspection.

When the OM indicated that the gaps had opened and there was no more conductivity in the control structures, the wafer was inspected on SEM to measure the layer thickness. Figure 5.16 depicts the silicon layer and respective thickness corresponding to the average thickness mapping previously done on the device layer thinning process concluding the structure etch.

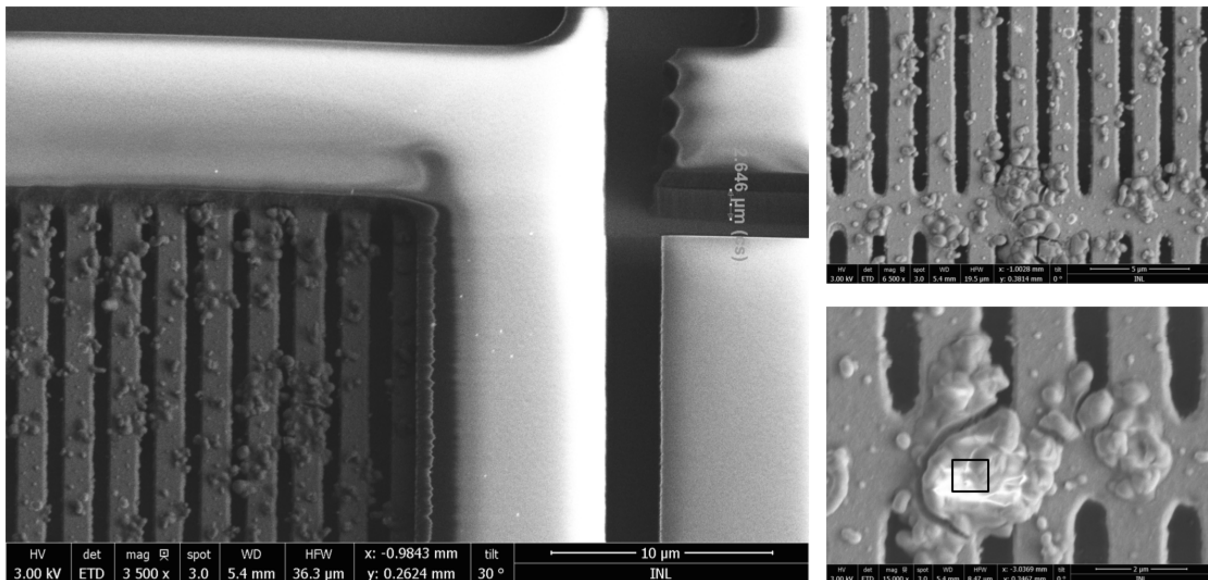

Figure 5.15: Device layer etch, SEM inspection after ICP.

As noticed in figure 5.15, the grid did not break, although this presented material residues along its surface. This will not compromise the target application of the device, maintaining its structural integrity and not breaking. Furthermore, the bursts were inspected on EDX INCA software present on the FEI NovaNano SEM system, and it is concluded that they are made up of Oxide and Aluminium, as seen in figure 5.16.

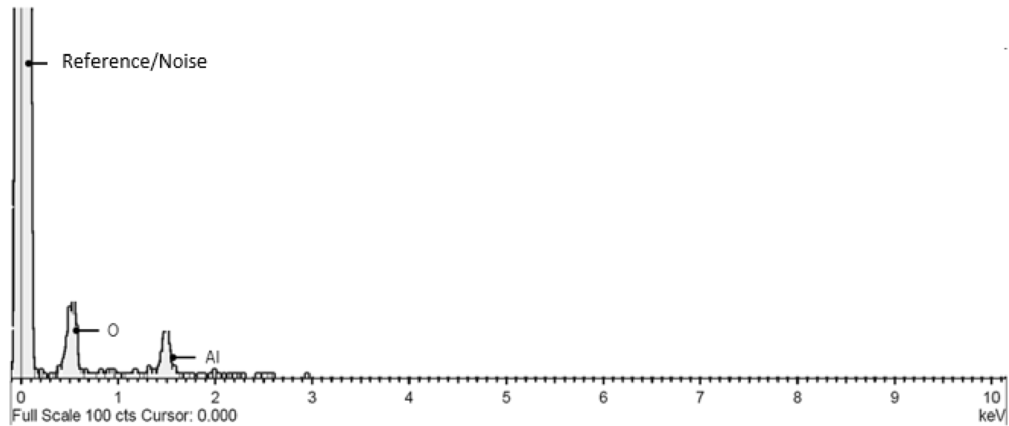

Figure 5.16: Grid inspection on EDX INCA software present on the FEI NovaNano SEM system.

Finally, the wafer was introduced in the SPTS Pegasus system and using O2 Strip, the remaining mask layer and possible residues were removed. The final inspection was done on SEM, figure 5.17.

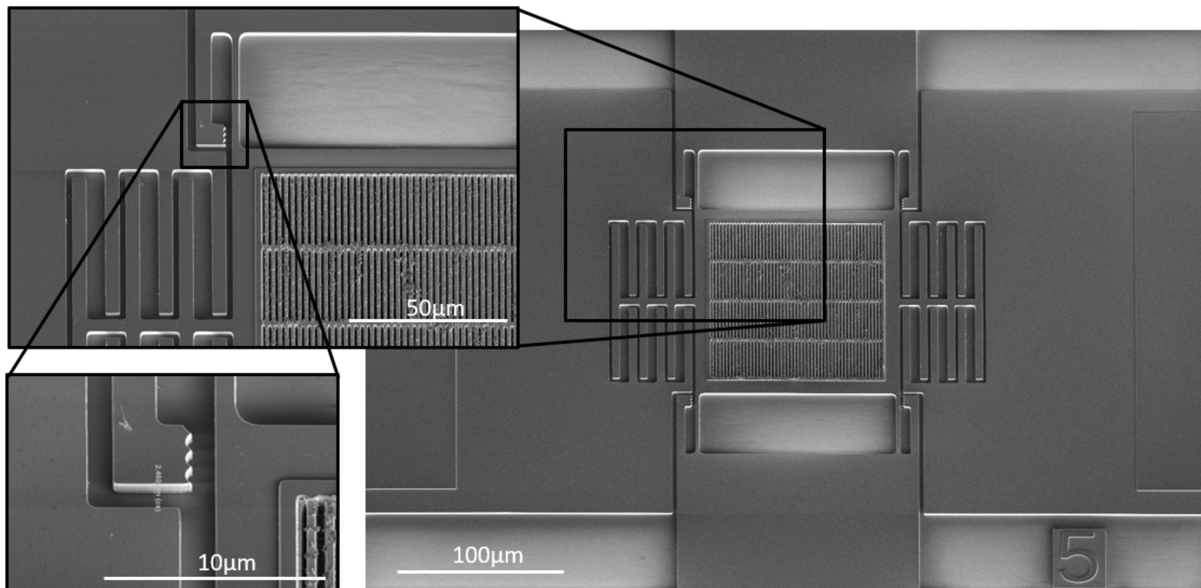

Figure 5.17: SEM inspection after structure etch.

5.3.8 BS Structure Etch

At this stage, and because the wafer is going to be handled through the BS, to give extra protection to both hard marks on the FS against scratching, cracking and other types of mechanical damage, it is deposited a layer of SiO2 and a polyimide coating. The BS structure etch uses the SPTS Pegasus system through fast Silicon DRIE.

The trench's depth is monitored on the Nanocalc system, and the etch time is adjusted accordingly.

Figure 5.18 is OM photo where it is possible to verify, from the FS, the open trenches and, in some cases, the respective overetch while noting that it is possible to see through the buried oxide layer.

Figure 5.18: BS trenches etch seen through the FS, OM.

After the OM inspection, it is concluded that the trenches are etched and the polyimide and the residues left on the wafer are removed through an O2 cleaning.

5.3.9 Structure Release

The last microfabrication step is the structure release, and it consists of the removal of the BOX that is exposed. This step uses the SPTS Primaxx - HF Vapor Etcher system, where sacrificial layers are isotropically etched using gaseous acids such as Hydrogen fluoride to release the free-standing components of the device.

Figure 5.19: Structure release, silicon oxide etch.

The patterned wafer is positioned over a dummy wafer during the HF process. Between the two wafers, supports are placed on the edges to ensure a reasonable distance between the patterned wafer and the dummy. This particularity guarantees that when the structures are suspended by the springs, they do not stick to the dummy wafer.

Furthermore, the die separation from the wafer is accomplished due to a trench around the die with a 40μm width. A trench around each die was also added in the FS masks, overlaying the one on the BS, ensuring that each die could be easily separated from the wafer. Trenches have also been designed by forming the outline of four rectangles in both layers. As a result, at the end of the oxide removal process, there is one hole in each corner of the die, becoming easier to remove the die from the wafer.

The buried oxide layer removal is the last step of the fabrication process. At this moment, the SOI wafer has 152 dies suspended, ready to be used and tested. In figure 5.20, it is possible to observe the fabricated wafer, the trenches which mark each die and the individual holes.

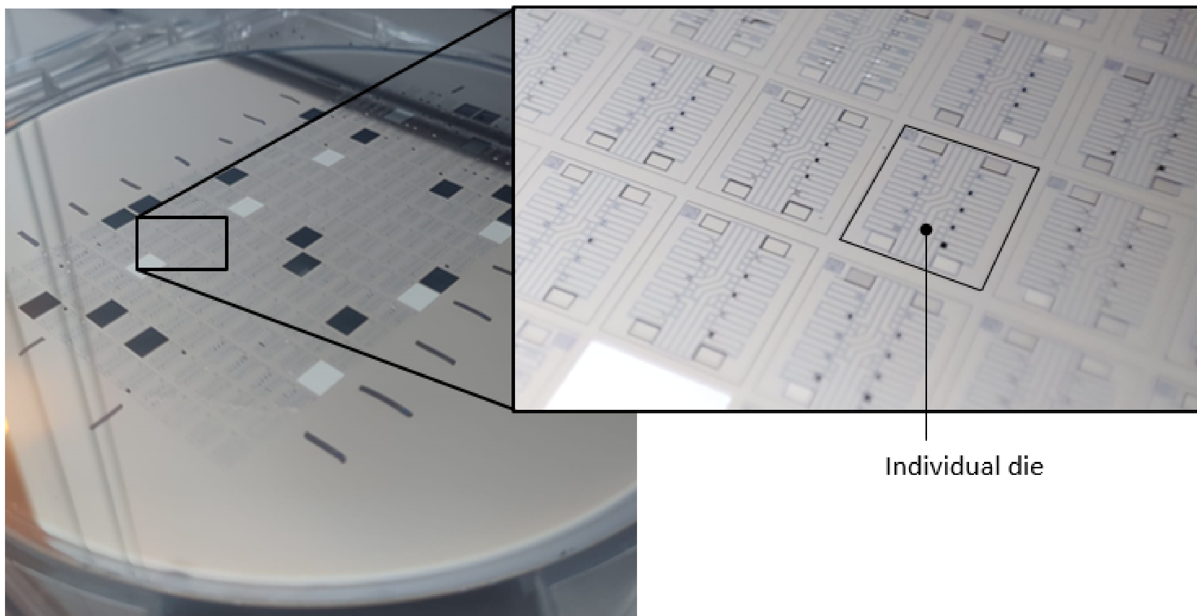

Figure 5.20: Wafer with the individual dies suspended.

5.3.10 Final Optical Inspection

When the wafer leaves the CR, it is necessary to evaluate the device's condition, so an optical inspection on the OM is performed while mapping the devices with the optimal structural results that are not compromised and can be characterized.

In the most general form across all devices, it is noticeable that the springs' width and length suffered some overetch, leading to longer and thinner springs which are also noted in the actuators. In the case of the parallel plate actuation structures, the gaps are wider, so the distance between the actuator and the moving mass also increases. In the comb drives, the distance between combs is wider.

Figure 5.21 is the optical inspection results of a parallel plate device and respective measurements (left) and comb drive (right).

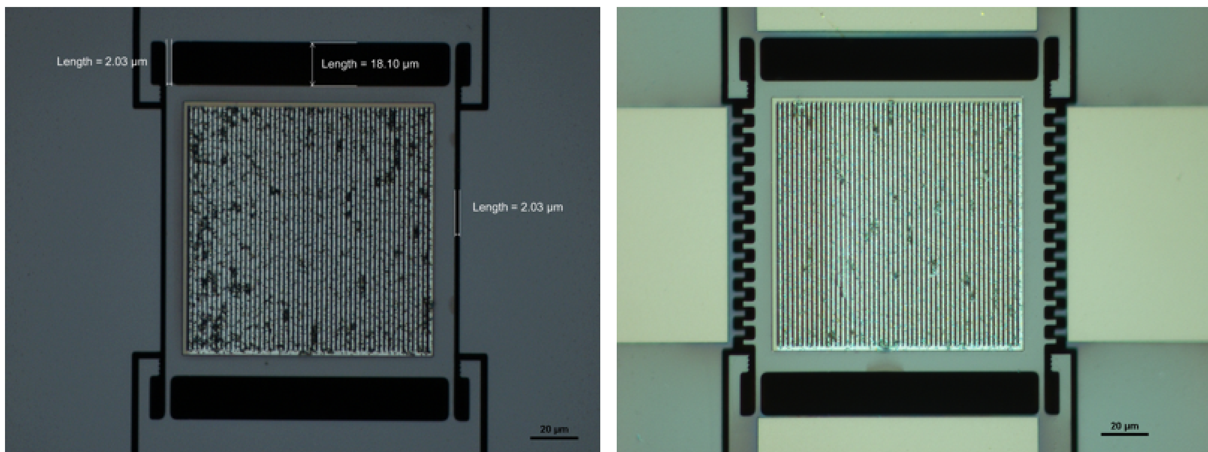

Figure 5.21: Optical inspection results of a parallel plate (left) and comb drive (right).

While the general optical inspection is performed, it is noticed that devices where the grid area is 200x200 μm^2 instead of 100x100 μm^2 (S09 and S10) present no intact devices or structures with minimal damage, resulting in no devices to be characterised. Devices with a spring target width bigger than 42 μm, which is the case of S03, S04, S06 and S08, although not so significant, also have structural damages having more than one spring broken. In figure 5.22 is possible to verify examples of damages sustained.

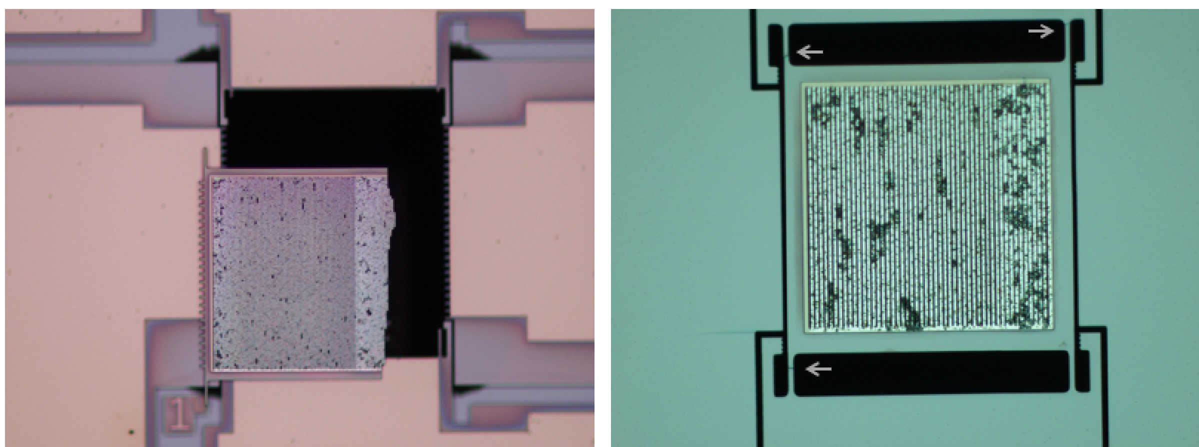

Figure 5.22: Optical inspection results with structure collapse (left) and broken springs (arrows on right figure).

The remaining devices (S01, S02, S05 and S07) have samples in condition to be characterised. This was due to having smaller length springs where the stress is less when compared to the longer ones. The good condition of the springs was prioritised due to being directly linked with in-plane actuation.

The adjusted mechanical features analysed in the optical inspection are further depicted 6.1.

5.4 Conclusions

This chapter detailed the microfabrication of the optical actuator and additional information about the deposition and etch methods used.

Critical steps in the form of alignment between both FS masks and BS were met. This was accomplished with a mask aligner system that proved effective with minimal misalignment between masks. Another particularity of the microfabrication of these devices where the protection and final integrity of the existing grid due to the introduction of polymers as a protective layer proved successful. The device layer etch was a critical step, and it was dealt with precaution where the adapted etch method was proven effective, not breaking the unprotected grid.

The discrepancies between the expected devices' measurements and the final ones are noticed upon optical inspection. Special recognition goes to the overetch of the device layer, which results in variations in the width and length of the actuator's springs and actuator, making the device's dimensions different when compared with the projected device.

Overall, the sustained variation in the structure and the BS trenches design makes the mass of the handle layer below the grid sometimes too heavy to support, leading to released devices and broken springs.

Subsequently, the number of devices for characterisation is less than expected, and its behaviour is not ideal compared to the theoretical prospects and objectives.

The die separation was done easily, and experimental tests can still be performed.

Chapter 6

Experimental Characterization

The fabricated actuator behaves as an optical modulator operating at a high resonance frequency with a substantial displacement. The tests performed aim to find the operating actuator's resonance frequencies, finding the one responsible for the in-plane movement. After, the displacement magnitude is measured. Several parameters and their influence were considered on the final results, naming the actuation signal and the vacuum chamber design to improve operating conditions while the device is characterised for frequency and displacement.

The experimental characterisation is performed using the Polytec MSA-500 system, where its analysis tools provide ways for data acquisition and respective visualisation and evaluation. Tests were conducted in the atmosphere and then in the vacuum chamber for comparison.

This chapter will mention the packing of the devices, the measurement set-up and respective characteristics, as well as surface topography, out-of-plane and in-plane analysis. These aim to characterise the microactuator's performance and behaviour, further assessing possible changes to optimise respective working characteristics.

6.1 Structure Selection and Packaging

As previously mentioned in (5.3.10), the devices that will be characterised are summarised, and the respective adjusted mechanical features are depicted in the table 6.1. These measurements are based on the measurement tool of the Optical Microscope.

The adjusted mechanical features are now used to model the analytical and theoretical behaviour of the devices upon characterisation. Based on the adjusted models, it is possible to establish a closer assessment of the mechanical characteristics of the device.

Table 6.1: Mechanical features adjusted.

Parameters	**S01**	**S02**	**S03**	**S04**	**S05**	**S06**	**S07**	**S08**	**S09**	**S10**
Grid dimension [um^2]	104x104								206x206	
Spring Length [um]	18.1	18.1	43.8	43.4	39.87	43.4	18.1	43.6	12.7	30.1
Spring Width [um]	2.03									
Type of actuator [um]	Parallel Plates					Comb Driver				
Gap, d0 [um]	3.87	2.03	3.68	2.03	2.03	1.74				
Number of viable devices	2	2	-	-	12	-	1	-	-	-

The dies with devices that are not compromised are placed in a chip carrier (made in a PCB). This chip carrier was designed while keeping in mind the modulator's optical application, so it has a cavity that goes through the PCB, and the die is placed directly above. The defined area of the cavity accommodates all ten devices and an adjacent area marked for the guideline of the die, figure 6.1.

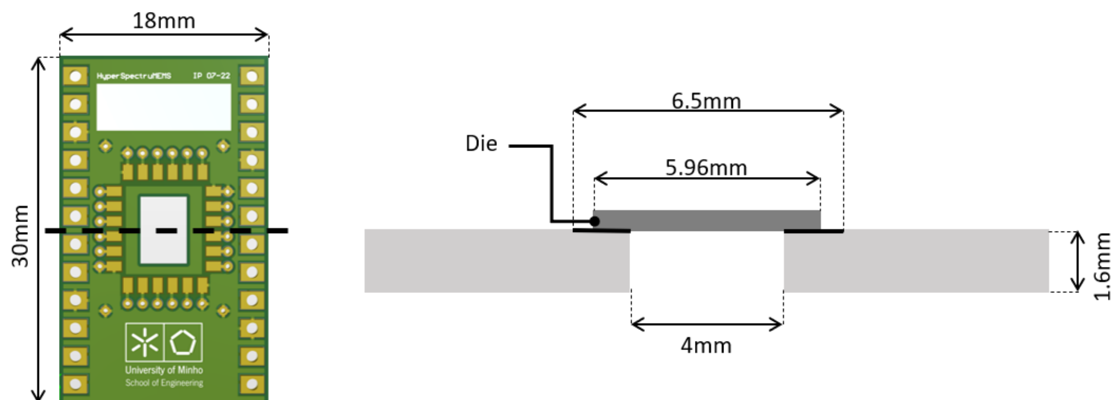

Figure 6.1: Chip carrier and respective cross-section.

Figure 6.2 is the chip carrier with a die and respective connections made through wire bonding. The Chip-carrier schematic and connections are presented in Appendix E - Chip Carrier.

Figure 6.2: Chip carrier with die connected through wire bonding.

6.2 Measurement Set Up

Static and dynamic analysis and visualisation are critical parts of the test and development process for MEMS devices. They are indispensable for validating FE calculations and measuring surface deformation. To characterise the devices and obtain analytics of their behaviour and performance, the Polytec MSA - 500 system was used.

Also, a vacuum chamber is designed to better the performance and compliance of the device with approximations of the device's ideal and optimal behaviour.

6.2.1 Polytec

The Polytec MSA-500 Micro System Analyser combines three measuring techniques in one instrument, which allows a comprehensive investigation of a microstructure:

1. Surface topography (i.e. the z-coordinate of each point in a surface) with sub-nanometer resolution.

2. In-plane deformation and vibration modes, with nanometer amplitude resolutions and at frequencies up to 1MHz.

3. Out-of-plane deformation and vibration modes, with picometer amplitude resolutions and at frequencies up to 24MHz.

The combination of all three techniques makes the Polytech MSA-500 a universal tool for obtaining 3D profiles and determining surface parameters, identification and measurement of system resonances and detailed information about amplitude and phase.

TMS - Topography Measurement System

When designing or manufacturing microsystems, structured functional surfaces require precise verification of surface topography to assure quality and performance.

The Topography Measurement System accomplishes a high-resolution and high-precision x y z mapping of the sample. Using a light source, part of the light is directed onto a reference surface and the other part onto the surface of the object under investigation. The light is reflected from both the reference and the test surface and is detected by a camera, thus detecting the interference pattern.

The sample's topography is shown in 2-D or 3-D, and a true topographical representation of the surface can be reconstructed and evaluated.

PSV - Scanning Vibrometer

The laser-Doppler vibrometer determines the vibration velocity and displacement at a measurement position. The moving surface to be characterised scatters light from the laser beam, and the Doppler frequency shift is used to measure the component of velocity which lies along the axis of the laser beam.

This way, optical vibration measurement Scanning laser-Doppler vibrometry allows non-contact measurements in real time to characterise out-of-plane behaviour by defining a scanning grid of the surface to be analysed, and the vibrometer moves to each point on the scan grid and measures the response.

An internal generator using Polytec software control provides a calibrated vibration excitation of the test object. In addition to the internal generator, an external excitation source can be used with the MSA-500.

PMA - Planar Motion Analyzer

Planar Motion Analyzer obtains accurate amplitude and phase information of in-plane resonance with further displacement behaviour data.

A stroboscopic technique is applied to precisely measure the high frequency and in-plane motion of the device under test. Using stroboscopic illumination and digital imaging, motions of periodically moving objects are captured, and the exact position of a given region is reconstructed in time.

The procedure works as the region of interest is defined, and an excitation signal of the internal signal generator excites the component with a broadband signal frequency of up to 1 MHz. The stroboscopic video employs a short light pulse synchronised with the device motion capturing the position at precise phase angles. By shifting the timing of these pulses by phase angle increments, the motion of a moving object can be sampled and reconstructed. The electronic camera shutter remains open until enough light at the same phase of the periodic motion has been collected.

The video sequences of the region selected are analysed using a measurement algorithm in the software and allow the visualisation of measurement of displacement system resonances, transient responses, phase variations, amplitudes and bode plot graphs.

6.2.2 Vacuum Chamber

A vacuum chamber was constructed to accommodate low-pressure conditions and improve the device's performance. In the vacuum chamber design, several characteristics were considered, such as the height that the die had to be placed inside the chamber, the maximum acrylic thickness and if it could withstand the lower pressures with no breakage.

Therefore, knowing the focusing distance of the operating lens, the chip carrier had to be raised by introducing a spacer between the socket and the bottom piece of the acrylic chamber. While the device was higher, the top piece of acrylic would still need to be thin enough so that the lens could still focus but not so thin that it could compromise the ability to resist lower vacuum pressures.

The final set-up comprises a bottom 5 mm acrylic piece, a middle part of 13 mm and a 2 mm piece on top of that. Then it was added a 5 mm acrylic with a window on top of everything to give back support and structural integrity to the vacuum chamber, not interfering with the working focusing distance of the lens used for characterisation.

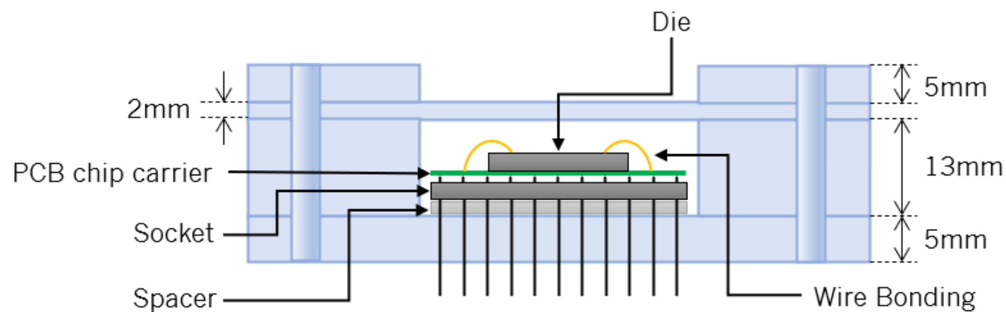

Figure 6.3: Vacuum Chamber set up.

The assembly was done with eight screws distributed along the vacuum chamber. The electrical connections are made through a PCB board, and the vacuum can be turned on without moving the chamber. The final set-up for the upcoming tests is depicted in figure 6.4.

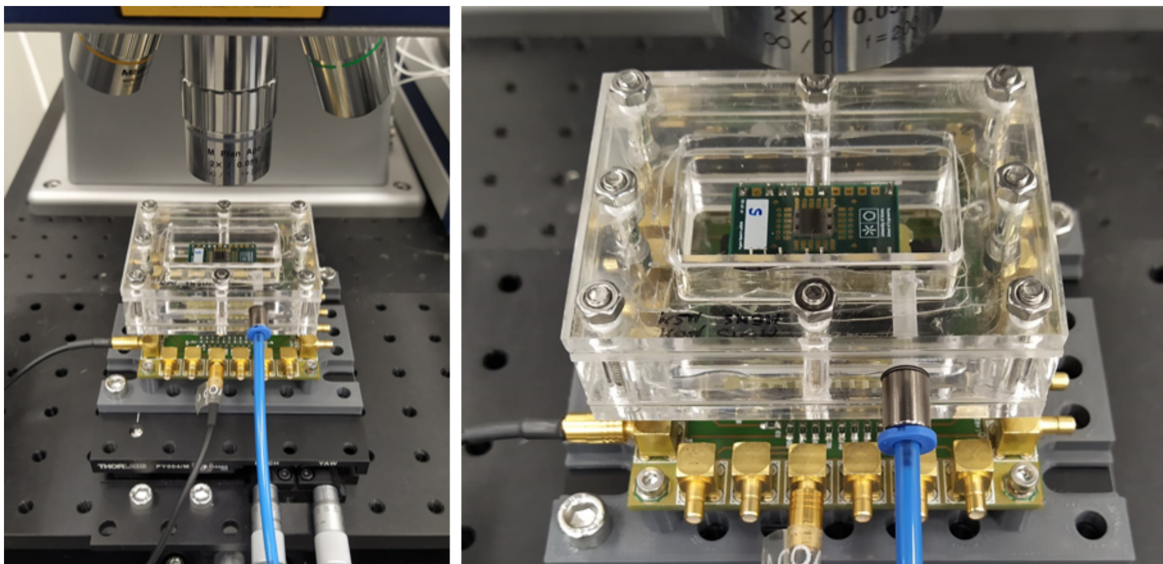

Figure 6.4: Final characterisation set up.

6.3 Surface and Topography Analysis

The Topography Measurement System (TMS) allows scanning of the surface of the device to be characterised. So, it was performed a 3-D analysis of some devices where off-plane anomalies can be detected.

As previously mentioned in 5.2, the devices to be characterized are identified by their cell number, followed by the die and then the structure number within the die. The cell can be from C01 to C19 depending on its location on the wafer; the die is related to the number of dies in one cell, so from D01 to D08 and the structure number from S01 to S10.

The 3-D scanning of the C04D04S07 device is depicted in figure 6.5(a), where the displacement off the plane is perceptible. Another device whose topography was analysed was the C07D05S05 having minimal deflection, and the device is at the same plane, figure 6.5(b).

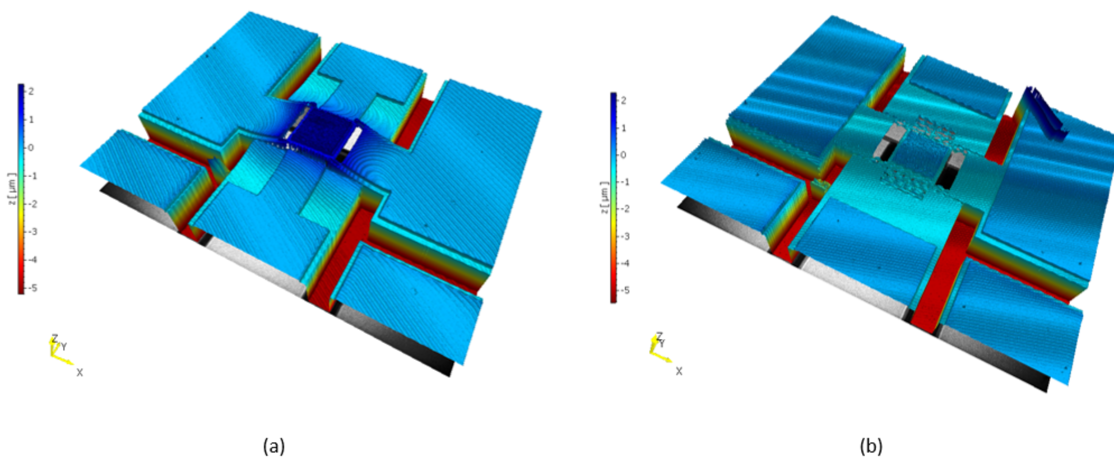

Figure 6.5: 3D scanning of the C04D04S07 device (a) and C07D05S05 (b)

Notice that in the case of (a), the die having full aluminium connections makes the movable mass move upwards due to the residual stress consequence of having the aluminium closer to the movable structure.

Figure 6.6 shows the scanning in both the x and y axis and respective z displacements. On the left are the topography of the C04D04S07 corresponding results, and on the right are the equivalent results for the C07D05S05 device.

The first shows a deviation from the reference flat to the grid of almost 2 μm in both x and y. Considering the device layer thickness of an average of 2.665 μm and a 2 μm upwards bending, the overlapped area of the combs reduces, reducing the electrostatic force and, consequently, the displacement. The second device, although with some deflection, it is not critical.

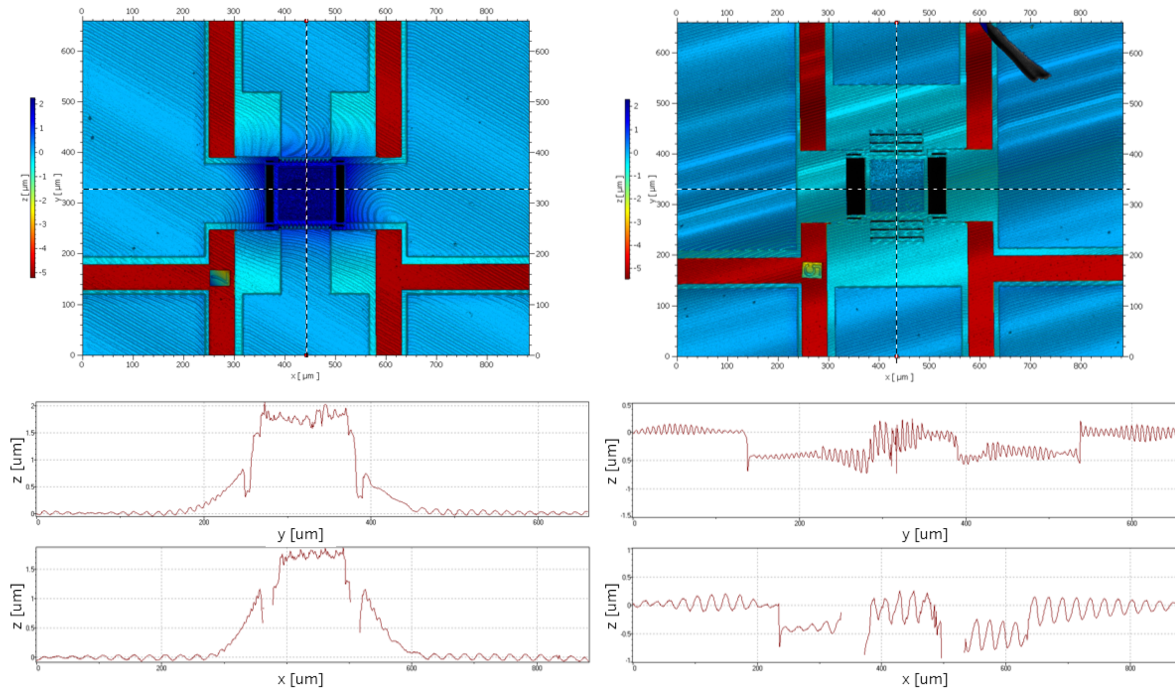

Figure 6.6: Scanning results of mentioned devices.

6.4 Out of Plane and Vibration Analysis

To understand each device's different resonance modes, out-of-plane vibration analysis was performed with the PSV system. This way, it was possible to find the various resonance modes of each device and try to match the equivalent of its behaviour.

The mechanical values of the devices were detailed in table 6.1, which are the result of the optical inspection performed, so the model for the FEM Eigenfrequency analysis is adjusted accordingly. Table 6.2 are the results of the resonance frequency evaluation regarding the adjusted values of the devices viable for characterisation. S01 and S02 have the same Eigenfrequency results as the spring's length, and width is the same.

Table 6.2: Comsol Eigenfrequencies for the adjusted mechanical values with the one responsible for the in-plane vibration highlighted in bold.

	Eigenfrequency [MHz]					
Structure	**1**	**2**	**3**	**4**	**5**	**6**
S01/S02	0.56572	1.0467	**1.1378**	1.2166	1.7075	2.4184
S05	0.2527	0.25315	**0.33364**	0.41087	0.42023	0.4463
S07	0.55822	0.98691	**1.1110**	1.2130	1.6135	2.3336

Each mode translates a different vibration mode, and the frequency responsible for the in-plane vibration is 1.1378 MHz for S01 and S02, 0.33364 MHz for S05 and 1.1110 MHz for S07.

An external excitation source was used to provide the device with a sine wave of 10 Vpp and 5 V DC offset while doing a frequency sweep within an interval coincident with the resonance frequencies found in the analytical FEM study with the updated geometry study.

The two laser beams for this analysis were moved, the reference beam laser to where the device's displacement is static and the second one to the moving part of the device.

The results obtained after the out-of-plane vibration analysis consist in a frequency spectrum where for the resonance frequencies, there is a correspondent displacement magnitude in the z-axis. Figure 6.7 is the respective analysis of the C05D04S05 device, and the same frequency sweep was performed in atmospheric conditions and in vacuum.

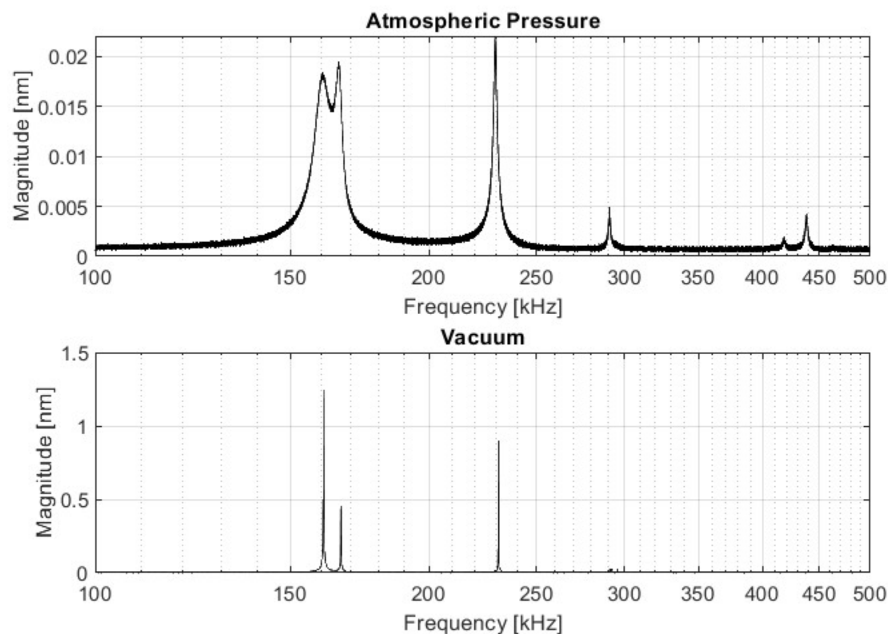

Figure 6.7: Out of plane and vibration analysis, C05D04S05.

The results show that for the resonance frequencies in the atmospheric pressure, the correspondent frequency in vacuum shifts to the right, typical of the spring hardening due to lower pressures. The magnitude displacement of each resonance frequency also grows in vacuum.

Comparing the frequency results of the out-of-plane vibration analysis and the eigenfrequency modes of the FEM evaluation, it is possible to approximate the one responsible for the in-plane movement. Not every mode is detected in the PSV evaluation.

In the case of the device analysis displayed in 6.7, the frequency corresponding to the in-plane vibration

is approximately set at 292.5 kHz.

More devices were submitted to the out-of-plane and vibration analysis, and the respective results are gathered in table 6.3. The sweep analysis results were gathered at atmospheric pressure, and the corresponding results are noticeable peaks while doing the frequency sweep.

Table 6.3: Out of plane and vibration analysis frequency results.

	Experirmentally identified frequency peaks [MHz]					
Structure	**1**	**2**	**3**	**4**	**5**	**6**
C18D03S01	0.171653	0.340513	0.542732	0.658259	1.272939	
C18D01S02	0.63031	0.761101	1.240247	1.4757	1.62994	1.680144
C05D04S05	0.160249	0.165781	0.229644	0.290968	0.418713	0.438108
C04D04S07	0.140874	0.207017	0.368738	0.525298	0.711711	0.788347

6.5 In-plane Analysis

After the out-of-plane and vibration analysis was performed to find the resonance frequency responsible for the in-plane movement of the fabricated devices, the in-plane motion was measured by stroboscopic video on the Planar Motion Analyzer of the Polytec.

6.5.1 Measurements at atmospheric pressure

The first test was performed at atmospheric pressure and without the vacuum chamber set up, so it has no interference of the acrylic barrier between the lens and the device, making up for a good reference and keeping the noise levels to a minimum.

The device is located, and the study area is chosen; in this case, the most suitable is where both static and movable actuators are. The supply source is internal and consists of a sine wave with 5 V amplitude and 5 V DC offset. The frequency sweep range comprises the in-plane resonance frequency, from 288 kHz to 293 kHz, with a 50 Hz step.

For the C05D04S05 device, the magnitude and phase obtained in the in-plane analysis are presented in figure 6.8 with the respective fitting. The quality factor is 271.9, and the resonance frequency is 290.67 KHz. Additionally, the maximum displacement is 74 nm, as depicted in figure 6.9.

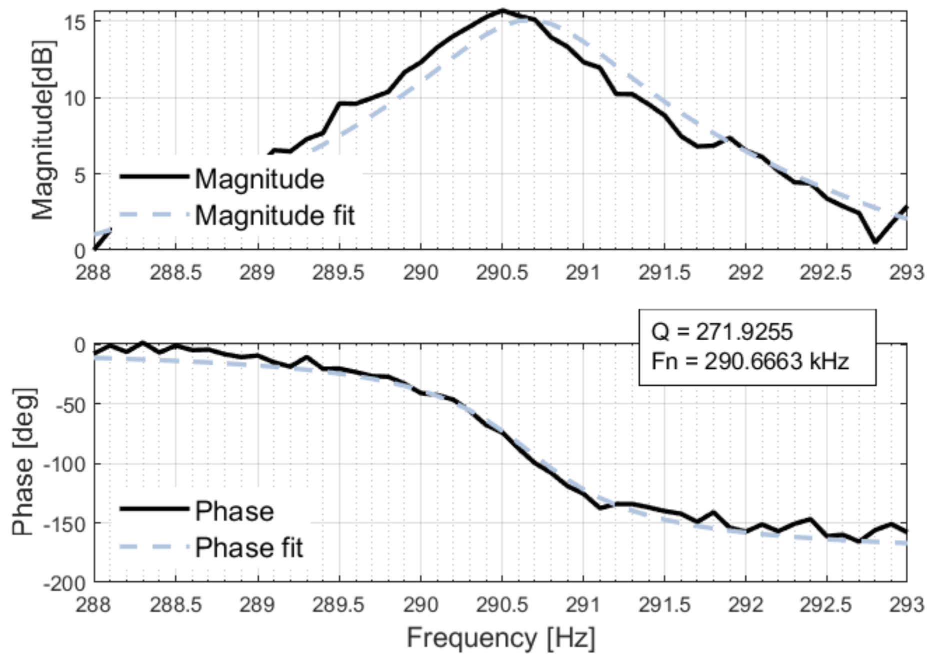

Figure 6.8: Magnitude and phase of C05D04S05 device.

6.5.2 Measurements at Vacuum

First, the acrylic chamber was connected to a lab vacuum line (maximum -0.9 bar pressure). The actuator response was saved and compared to the results at atmospheric pressure. The test was done under the same conditions: the internal supply source consists of a sine wave with 5 V amplitude and 5 V DC offset. The frequency sweep is from 290 kHz to 294 KHz with a 50 Hz step.

Compared to the results obtained at the atmosphere pressure, it is noticeable the increase in quality factor value; as the quality factor increases, the damping coefficient decreases and, consequently, the magnitude displacement also increases from 74 nm to approximated 160 nm, figure 6.9.

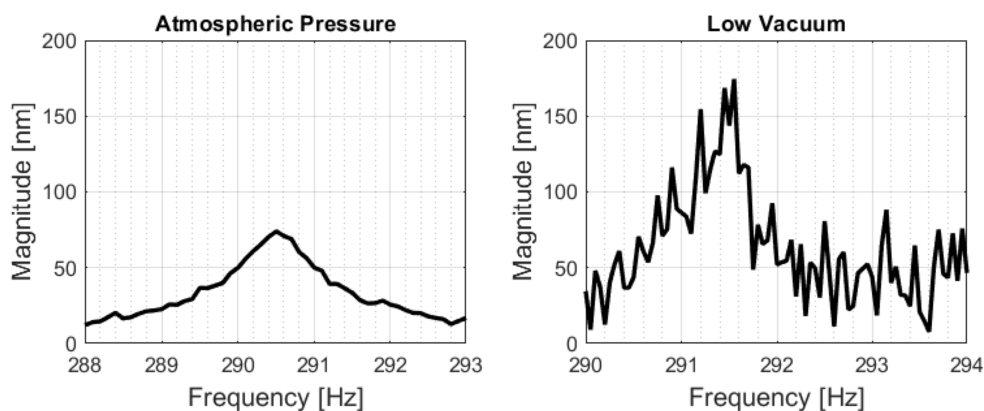

Figure 6.9: C05D04S05 device displacement magnitude at atmospheric pressure and low vacuum.

To notice the influence of noise in the displacement graphic when the acrylic barrier is present, the results at atmospheric pressure were obtained without the top acrylic layer, and when the vacuum chamber is set up, the Polytec image has less quality.

The results for the magnitude and phase at lower pressure and the equivalent fittings with the respective quality factor and resonance frequency are depicted in figure 6.10.

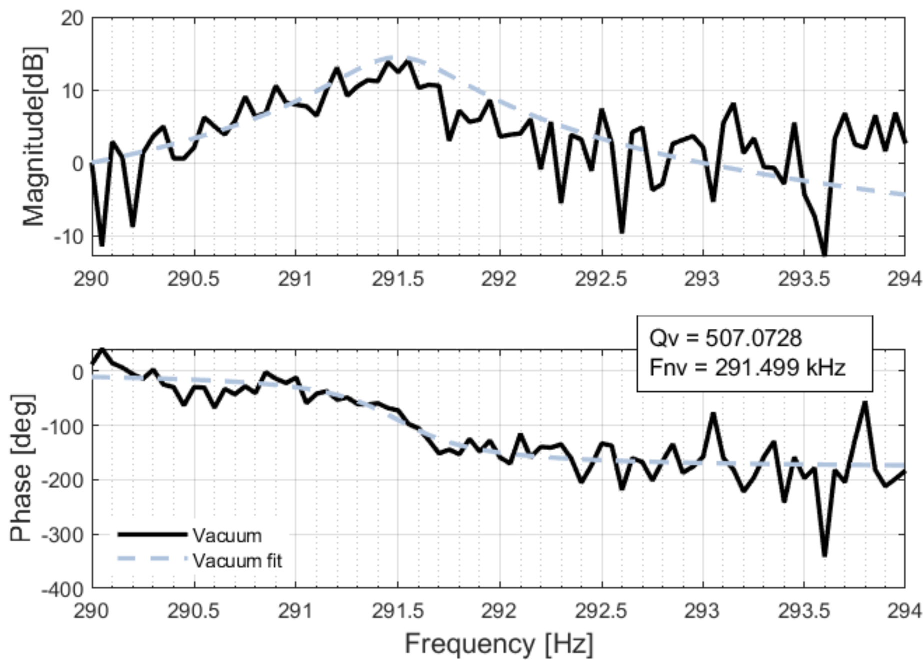

Figure 6.10: C05D04S05 device magnitude and phase at above -0.9 bar pressures.

The quality factor at lower pressure increased to 507.1 from the beginning point 271.9, and the resonance frequency started at 290.67 kHz and is now 291.5 KHz. Table 6.4 shows the microstructure's parameters when the device is submitted to the two different pressures and the theoretical values computed in the analytical simulation for the adjusted parameters.

Table 6.4: Microstructure's Parameters.

Parameters	**Atm. Pressure**	**Lower Pressure**	**Theoretical**
Resonance Freq., Fn[kHz]	290.67	291.5	293.7
Spring stiffness, k [N/m]	270.77	272.32	276.56
Damping Coeff., b [nN.s/m]	545.22	293.22	448.94
Quality Factor, Q	271.93	507.1	333.75

Between the values obtained for the two different pressure tests, the resonance frequency has a

positive shift being 290.67 kHz at atmospheric pressure and 292 kHz at lower pressure conditions. The spring stiffness also increases, being directly proportional to the frequency. The damping coefficient decreases as the pressure is reduced, consequently increasing the quality factor.

The positive resonance frequency shift is due to spring hardening behaviour which occurs as there is an increase in the effective spring constant as lower pressures are added to the system, and there is additional restoring force contribution from the gas compression within the chamber cavity.

The spring hardening and the spring softening are nonlinear phenomena in electrostatically actuated MEMS modulators/resonators. Nonlinearities in device operation can result from various MEMS specifications such as excitation voltage, resonator structure, device dimensions and pressure conditions, [36].

Spring softening is a reduction in the effective spring constant, manifesting as a downward shift in resonance frequency. Spring hardening is the opposite: an increase in the effective spring constant and an upwards shift in resonance frequency. The work demonstrated in [37] shows that by applying a constant DC voltage and varying the AC voltage, the results are translated to a spring hardening effect where the resonance frequency increases as it is AC voltages increase. In contrast, by varying the DC voltage and maintaining the AC amplitude, the resulting response is linked to the spring softening behaviour as the DC voltage increases, the resonance frequency decreases.

The spring hardening makes it so that the resonance frequency of the structure increases as the amplitude of oscillation also increases, and the maximum amplitude of displacement occurs at this frequency. On the other hand, when spring softening occurs, the resonance frequency decreases as the amplitude of oscillation increases. Further tests were conducted to verify this behaviour.

The vacuum chamber is connected to a vacuum machine instead of the laboratory vacuum line, and the pressure is further reduced. Maintaining the device in vacuum conditions, the structure response was tested when:

1. Constant DC and varying AC - Offset DC voltage is constant at 5 V, and the oscillation amplitude varies from 2 V to 5 V, with 0.5 V increments making the Vpp range between 4 to 10 Vpp;

2. Constant AC and varying DC - Oscillation amplitude is constant at 2 V, making Vpp 4 V, and Vdc varies from 2 V to 8 V with 1 V increments.

Other variables, such as frequency sweep interval and corresponding steps, were kept between runs. Then, the same tests were performed with steps of 50 Hz, 10 Hz and 5 Hz. The amplitude displacement results with a 50 Hz step are in figure 6.11.

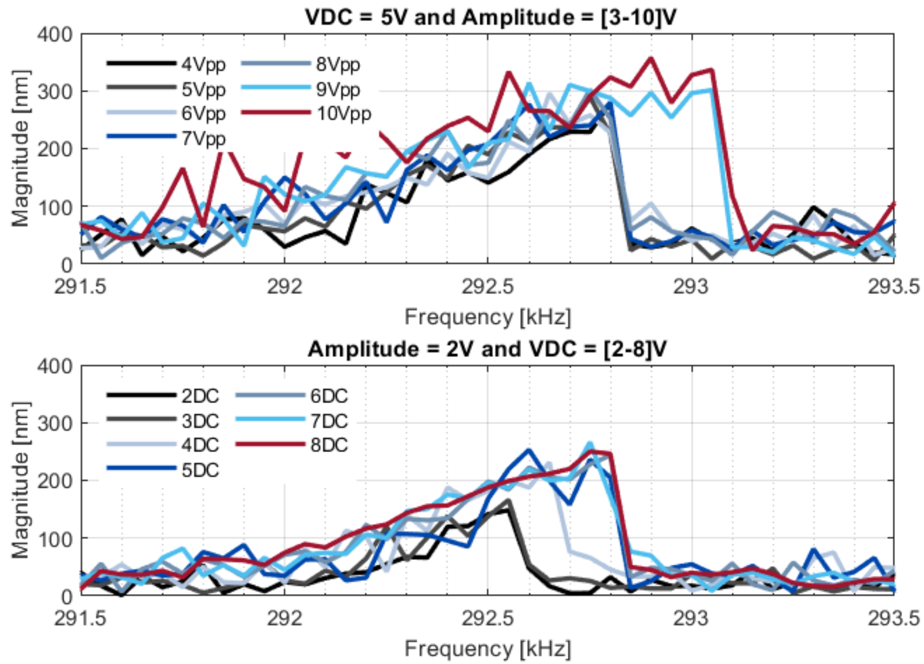

Figure 6.11: C05D04S05 device magnitude displacement with constant DC and varying AC (top) and constant AC and varying DC (bottom).

To notice that for the same actuation voltages with 5 V DC and amplitude 5 V, as used to obtain the results of figure 6.10, but now with lower pressure, the resulting plot (red line in the first graph of figure 6.11) has another shift to the right with a value of 293.05 kHz. And the maximum displacement is set at around 357 nm. The damping was further reduced, and the quality factor increased, leading to more displacement amplitude.

Between both tests, there are notable differences, such as the behaviour of the resonance frequencies: in the case of constant DC and varying AC, the resonance frequency when the Vpp varies from 4 V to 8 V is the same at 292.8 kHz, while for Vpp of 9 V and 10 V, the resonance frequency is 293.05 kHz; in the case of constant AC and varying DC, the resonance frequency for both VDC 2 V and 3 V is 292.55 kHz. For VDC 4 V, the resonance frequency increases to 292.65 kHz and, finally, the resonance frequency of the remaining DC voltages is 292.8 kHz.

The hardening effect is dominant under the given conditions. This was expected, considering that the softening nonlinearity is introduced from the transverse electrostatic force and is small compared to the hardening introduced from the springs, [38].

In addition, the softening becomes dominant when the DC offset and amplitude voltages become relatively high, [37]. The softening at these conditions is impossible to verify, while noise interference limits the amplitude of the supply voltage.

Other areas where the spring softening can be noticed is if the maximum displacement magnitude does not happen at the same frequency as the resonance for each supply voltage applied.

So, the frequency step is changed to 10 Hz to increase data resolution and understand the hardening and softening of the springs better. Maintaining the same actuation condition tested before. The resulting plots are in figure 6.12.

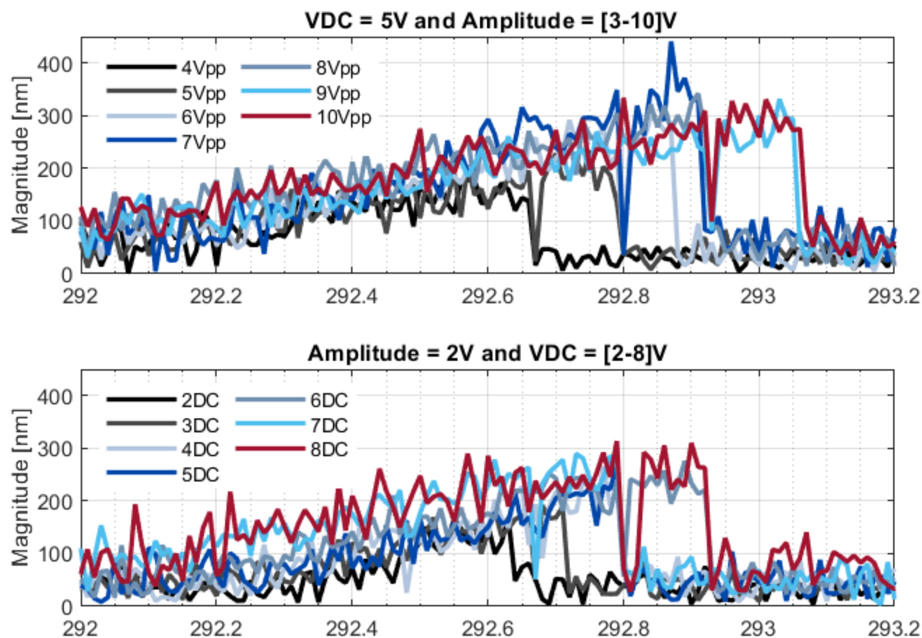

Figure 6.12: C05D04S05 device magnitude displacement with constant DC and varying AC (top) and constant AC and varying DC (bottom), step 10 Hz.

In the plots regarding the constant DC and varying AC, the frequency increases from 292.66 kHz to 293.06 kHz as the Vac actuation increases from 2 to 5V. And it is possible to observe that the maximum displacement at this condition happens when the amplitude is 3.5 V and is at a frequency smaller than the resonance frequency.

Observing both graphs, a sharp dip at an off-resonance frequency is noticeable. This dip generally immediately follows where the previous resonance frequency falls. This is because in the internal resonance condition, part of the mechanical energy of the first mode is transferred to a higher energy mode, and, as a result, the amplitude of the first mode is reduced, [39].

Notice that when the resonator has an applied electric voltage of 5 Vpp with a 5 V DC offset, the resonance frequency is 292.79 kHz, and the sharp dip fall at 292.67 KHz, which is close to the value of the resonance frequency when the actuation is 4 Vpp. Meaning that when applying larger driving voltages, the amplitude curve gets across the internal resonance condition without falling, although with a sharp

dip. The changing frequency value of the sharp dip can be linked to out-of-plane movement displacement interfering with in-plane spring stiffness.

Again, the same tests were performed with a 5 Hz step and the same actuation conditions as before to increase resolution. The resulting plots are in figure 6.13.

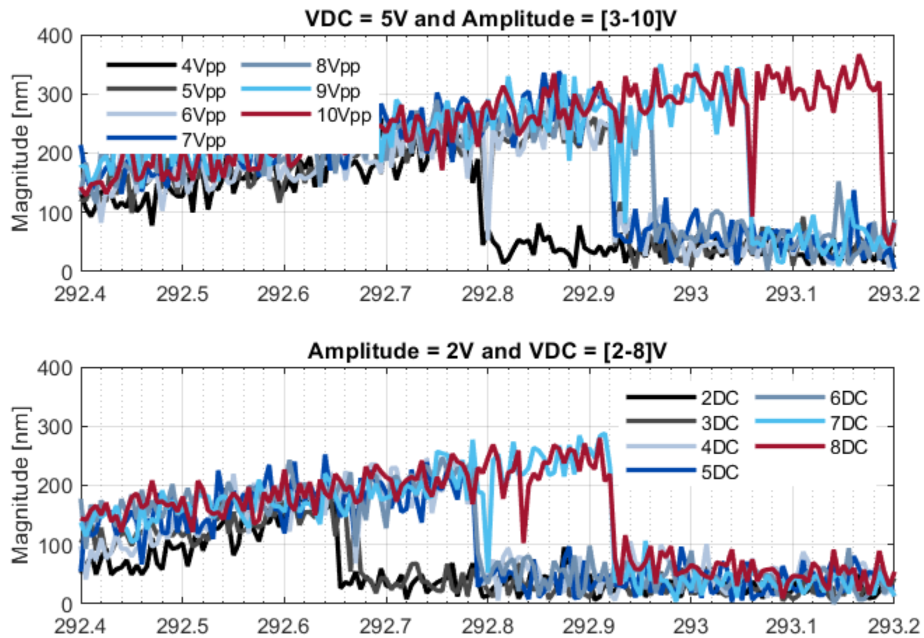

Figure 6.13: C05D04S05 device magnitude displacement with constant DC and varying AC (top) and constant AC and varying DC (bottom), step 5 Hz.

At this stage, the results with a 5 Hz step point towards the same conclusions as the previous results: the spring hardening behaviour is clearly noticeable across all the different actuation voltages. The resonance frequency value increases as the actuation amplitude or the DC offset increases. In some cases, the spring softening is observable, and it shows when the maximum amplitude displacement does not coincide with the resonance frequency of the supply signal.

The sharp dips persist as it remains almost coincident with the resonance frequency of the previous actuation voltage.

6.6 Conclusions

In this chapter, the modulator experimental characterisation was carried out, from which it is possible to conclude several points regarding the fabricated devices.

Regarding the measurement setup, in terms of the in-plane analysis, the devices with a resonance

frequency of 2MHz cannot be characterised, given the Polytec PMA limitation (maximum frequency to 1MHz). Even though the frequency value is reduced with the adjusted mechanical features obtained from the micromachining process, the resonance frequency for the in-plane movement in these devices is still superior to 1MHz. Furthermore, the vacuum chamber, although it works, can be improved to reduce the noise added to the system when the acrylic layer is in between the device and the microscope lens. By replacing the acrylic top layer with an alternative that is less thick and the digital image is improved.

The TMS analysis confirms that some devices present a significant out-of-plane deformation due to the full aluminium connections and consequent film stress, resulting in smaller actuation forces since the fixed and movable electrodes are misaligned and excitation of in-plane and out-of-plane simultaneously. The out-of-plane and vibration analysis is a good indicator to find the resonance frequencies of the various devices characterised here. Moreover, the respective COMSOL comparison allows for predicting the frequency mode responsible for the in-plane movement.

For the devices that could be characterised in-plane, the displacement and its behaviour were observed when submitted to both atmospheric pressure and vacuum conditions. With the reducing pressures comes an increase in the quality factor and a decrease in the damping factor, translating into bigger displacements, as expected. These values closely approximate the theoretical results with the mechanical parameters adjusted again.

Additionally, when comparing different pressure conditions, a spring hardening phenomenon was observed since the resonance frequency shifted to the right. Moreover, the influence of the two actuation components (AC and DC) and their respective influence on the spring behaviour was studied.

Although the mechanical features differ from the desired values due to overetch in the microfabrication, the results are a good indication of the operating dynamics of the modulator design.

Chapter 7

Conclusions

This dissertation concerns the development and characterisation of an optical modulator capable of operating at high frequencies.

The literature review section discusses the challenge of fabricating a device with high frequency and high displacement amplitudes and the trade-off between these operating conditions. Furthermore, the modulator operates as a 1-DOF electrostatic actuator, and the working equations on which the modulator was based were analysed as well as the variables that directly influence its behaviour which is the case of the damping, spring stiffness and movable mass.

The magnitude displacement is directly proportional to the quality factor of the system as the latter increases as the pressure condition are lowered.

The optical modulator described here is analytically modelled to achieve the operating goals set for the adaptation in the MPWC. And the given results were further analysed during the FEM simulations. Both the analytical and FEM studies allow for the model of multiple actuators with operating results that align with the parameters set in the beginning.

Regarding the fabrication process, the grid, the most challenging part, was patterned and etched successfully, along with the electrodes and device definition. The final yield of the process was poor, although the process was mostly successful. The observed overetch was much higher than expected, resulting in a significant deviation of the mechanical parameters concerning the desired values.

The adjustments of the pressure condition while testing by adding a vacuum chamber meant an achievable reduction of the damping factor, increasing the quality factor and leading to larger magnitude displacements.

7.1 Future Work

The work carried out in this dissertation is a good precedent for actuators with relatively high displacement for high resonance frequency. Although the target characteristics of the modulator were not met, it is still possible to conclude that this model design is a good indicator of the proposed initial solution.

The problems that were encountered and mentioned throughout this work were considered. Understanding what went wrong gives way to the possibility of bettering the results. The problems were recognised and are planned to be studied in the future as follows:

- Redesign to meet the target frequencies. Considering the overetch, the springs can be redesigned to be longer and shorter, withstanding the weight of the movable mass and stress;
- Optical modulation validation;

Bibliography

[1] J. P. Sáenz, "An introduction to micro electro mechanical systems (mems)," *Buran*, no. 22, pp. 13–18, 2005.

[2] P. F. Partnership, *An Introduction to MEMS*. 2002.

[3] M. Tilli and A. Haapalinna, "Chapter one - properties of silicon," in *Handbook of Silicon Based MEMS Materials and Technologies* (V. Lindroos, M. Tilli, A. Lehto, and T. Motooka, eds.), Micro and Nano Technologies, pp. 3–17, Boston: William Andrew Publishing, 2010.

[4] O. Solgaard, A. A. Godil, R. T. Howe, L. P. Lee, Y.-A. Peter, and H. Zappe, "Optical mems: From micromirrors to complex systems," *Journal of Microelectromechanical systems*, vol. 23, no. 3, pp. 517–538, 2014.

[5] B. T. Smith, D. Feng, H. Lei, D. Zheng, J. Fong, and M. Asghari, "Fundamentals of silicon photonic devices," *Kotura, Inc*, vol. 2630, 2006.

[6] M. Casalino, G. Coppola, M. Iodice, I. Rendina, and L. Sirleto, "Near-infrared sub-bandgap all-silicon photodetectors: state of the art and perspectives," *Sensors*, vol. 10, no. 12, pp. 10571–10600, 2010.

[7] A. D. Bristow, N. Rotenberg, and H. M. Van Driel, "Two-photon absorption and kerr coefficients of silicon for 850–2200 nm," *Applied Physics Letters*, vol. 90, no. 19, p. 191104, 2007.

[8] S. Zhu, M. Yu, G. Lo, and D. Kwong, "Near-infrared waveguide-based nickel silicide schottky-barrier photodetector for optical communications," *Applied Physics Letters*, vol. 92, no. 8, p. 081103, 2008.

[9] P. Dong, W. Qian, H. Liang, R. Shafiiha, D. Feng, G. Li, J. E. Cunningham, A. V. Krishnamoorthy, and M. Asghari, "Thermally tunable silicon racetrack resonators with ultralow tuning power," *Optics express*, vol. 18, no. 19, pp. 20298–20304, 2010.

[10] A. Rudnitsky, S. Agdarov, K. Gulitsky, and Z. Zalevsky, “Silicon based mechanic-photonic wavelength converter for infrared photo-detection,” *Optics Communications*, vol. 392, pp. 114–118, 2017.

[11] D. J. Bell, T. J. Lu, N. A. Fleck, and S. M. Spearing, “Mems actuators and sensors: observations on their performance and selection for purpose,” *Journal of Micromechanics and Microengineering*, vol. 15, p. S153, jun 2005.

[12] W.-T. Hsu and A. R. Brown, “Frequency trimming for mems resonator oscillators,” pp. 1088–1091, 2007.

[13] J. Barceló, I. de Paúl, S. Bota, J. Segura, and J. Verd, “Chaotic signal generation in the mhz range with a monolithic cmos-mems microbeam resonator,” in *2019 IEEE 32nd International Conference on Micro Electro Mechanical Systems (MEMS)*, pp. 1037–1040, 2019.

[14] Z. Chen, W. Liu, Q. Yuan, Y. Zhu, J. Yang, and F. Yang, “A novel ring-shaped extensional wine-glass mode rf-mems resonator with high quality factors,” in *2021 Joint Conference of the European Frequency and Time Forum and IEEE International Frequency Control Symposium (EFTF/IFCS)*, pp. 1–4, 2021.

[15] W.-t. Hsu, “Vibrating rf mems for timing and frequency references,” pp. 672–675, 2006.

[16] S. Pourkamali, A. Hashimura, R. Abdolvand, G. Ho, A. Erbil, and F. Ayazi, “High-q single crystal silicon harpss capacitive beam resonators with self-aligned sub-100-nm transduction gaps,” *Microelectromechanical Systems, Journal of*, vol. 12, pp. 487 – 496, 09 2003.

[17] R. Perelló-Roig, J. Verd, S. Bota, and J. Segura, “Thermomechanical noise characterization in fully monolithic cmos-mems resonators,” *Sensors*, vol. 18, no. 9, 2018.

[18] A. T.-H. Lin, J. Yan, and A. A. Seshia, “2.2 mhz piezoresistive mems oscillator operating in air,” *Procedia Engineering*, vol. 5, pp. 1498–1501, 2010. Eurosensor XXIV Conference.

[19] P. Singh, P. Gupta, P. Srivastava, M. Goswami, and B. Singh, “Design and analysis of high resonant frequency (1 mhz) mems accelerometer,” pp. 1–5, 04 2013.

[20] J. Grade, H. Jerman, and T. Kenny, “Design of large deflection electrostatic actuators,” *Journal of Microelectromechanical Systems*, vol. 12, no. 3, pp. 335–343, 2003.

[21] Y. M. Eltagoury, M. Soliman, M. Al-Otaibi, Y. M. Sabry, M. Sadek, and D. Khalil, “In-plane comb-drive actuator with high frequency-displacement product for micro-optical bench applications,” in *2014 International Conference on Optical MEMS and Nanophotonics*, pp. 155–156, 2014.

[22] Y. M. Eltagoury, M. Soliman, M. Sadek, Y. M. Sabry, and D. Khalil, “D1. high frequency in-plane mems actuator,” in *2015 32nd National Radio Science Conference (NRSC)*, pp. 323–328, 2015.

[23] P. Singh, P. Gupta, P. Srivastava, M. Goswami, and B. Singh, “Design and analysis of high resonant frequency (1 mhz) mems accelerometer,” in *2013 Students Conference on Engineering and Systems (SCES)*, pp. 1–5, 2013.

[24] W. Zhang, R. Baskaran, and K. L. Turner, “Effect of cubic nonlinearity on auto-parametrically amplified resonant mems mass sensor,” *Sensors and Actuators A: Physical*, vol. 102, no. 1, pp. 139–150, 2002.

[25] T. G. Bifano and J. B. Stewart, “High-speed wavefront control using MEMS micromirrors,” vol. 5895, p. 58950Q, 2005.

[26] J. Lardies, O. Arbey, and M. Berthillier, “Analysis of the pull-in voltage in capacitive mechanical sensors,” in *International Conference on Multidisciplinary Design Optimization and Applications*, (Paris, France), June 2010.

[27] M. Bao, “Chapter 3 - air damping,” in *Analysis and Design Principles of MEMS Devices* (M. Bao, ed.), pp. 115–174, Amsterdam: Elsevier Science, 2005.

[28] R. Pratap, S. Mohite, and A. Pandey, “Squeeze film effects in mems devices,” *Journal of the Indian Institute of Science*, vol. 87, 01 2007.

[29] T. Veijola, H. Kuisma, J. Lahdenperä, and T. Ryhänen, “Equivalent-circuit model of the squeezed gas film in a silicon accelerometer,” *Sensors and Actuators A: Physical*, vol. 48, no. 3, pp. 239–248, 1995.

[30] T. Veijola and M. Turowski, “Compact damping models for laterally moving microstructures with gas-rarefaction effects,” *Journal of Microelectromechanical Systems*, vol. 10, no. 2, p. 263–273, 2001.

[31] S. Dutta, P. Saxena, A. Panchal, R. Pal, K. Jain, and D. Bhattacharya, “Effect of vacuum packaging on bandwidth of push–pull type capacitive accelerometer structure,” *Microsystem Technologies*, vol. 24, 12 2018.

[32] J. W. Lee, R. Tung, A. Raman, H. Sumali, and J. P. Sullivan, “Squeeze-film damping of flexible microcantilevers at low ambient pressures: theory and experiment,” *Journal of Micromechanics and Microengineering*, vol. 19, p. 105029, sep 2009.

[33] W. Sharpe, K. Jackson, K. Hemker, and Z. Xie, “Effect of specimen size on young’s modulus and fracture strength of polysilicon,” *Journal of Microelectromechanical Systems*, vol. 10, no. 3, pp. 317–326, 2001.

[34] A. B.-H. YD Premchand and Z. S. LJ Gauckler, ETH Zurich, “Micro cells,” 2009.

[35] G. K. Celler and S. Cristoloveanu, “Frontiers of silicon-on-insulator,” *Journal of Applied Physics*, vol. 93, no. 9, pp. 4955–4978, 2003.

[36] V. Zega, G. Langfelder, L. G. Falorni, and C. Comi, “Hardening, softening, and linear behavior of elastic beams in mems: An analytical approach,” *Journal of Microelectromechanical Systems*, vol. 28, no. 2, pp. 189–198, 2019.

[37] A. M. Elshurafa, K. Khirallah, H. H. Tawfik, A. Emira, A. K. S. Abdel Aziz, and S. M. Sedky, “Nonlinear dynamics of spring softening and hardening in folded-mems comb drive resonators,” *Journal of Microelectromechanical Systems*, vol. 20, no. 4, pp. 943–958, 2011.

[38] S. Johnson, “Experimental analysis of spring hardening and softening nonlinearities in microelectromechanical oscillators.,”

[39] D. Antonio, D. Zanette, and D. Lopez, “Frequency stabilization in nonlinear micromechanical oscillators,” *Nature communications*, vol. 3, p. 806, 05 2012.

Appendix A

Appendix - Alignment Marks Mask

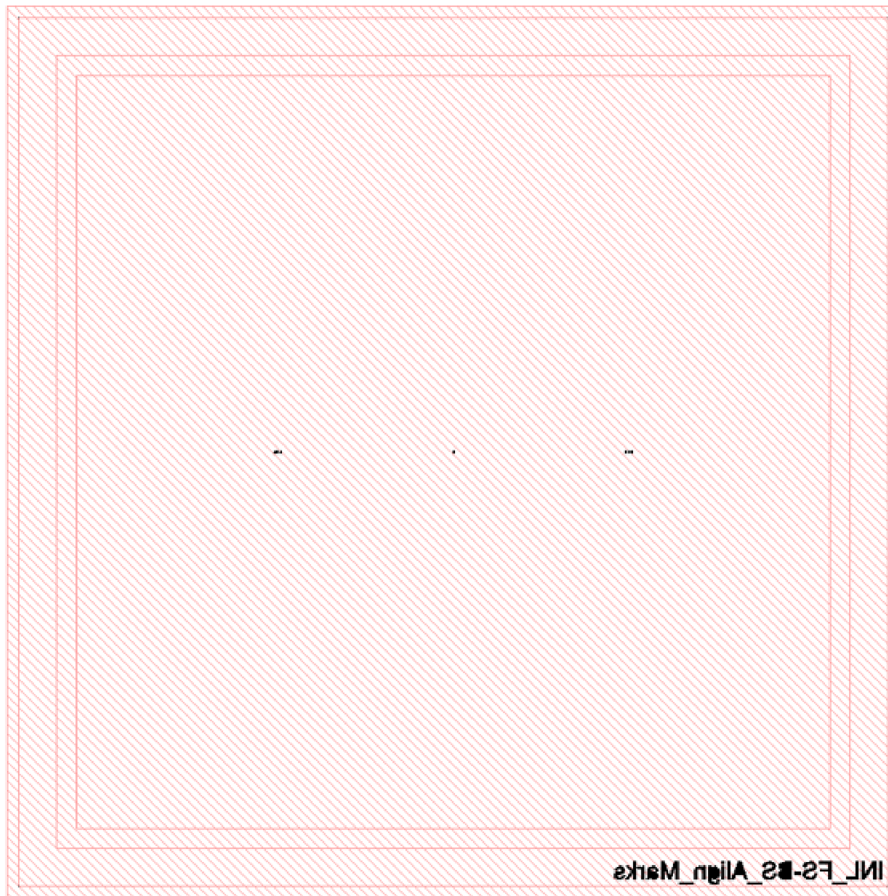

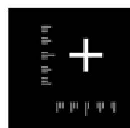

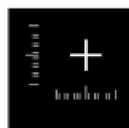

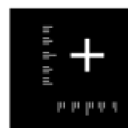

Appendix B

Appendix - Metal Mask

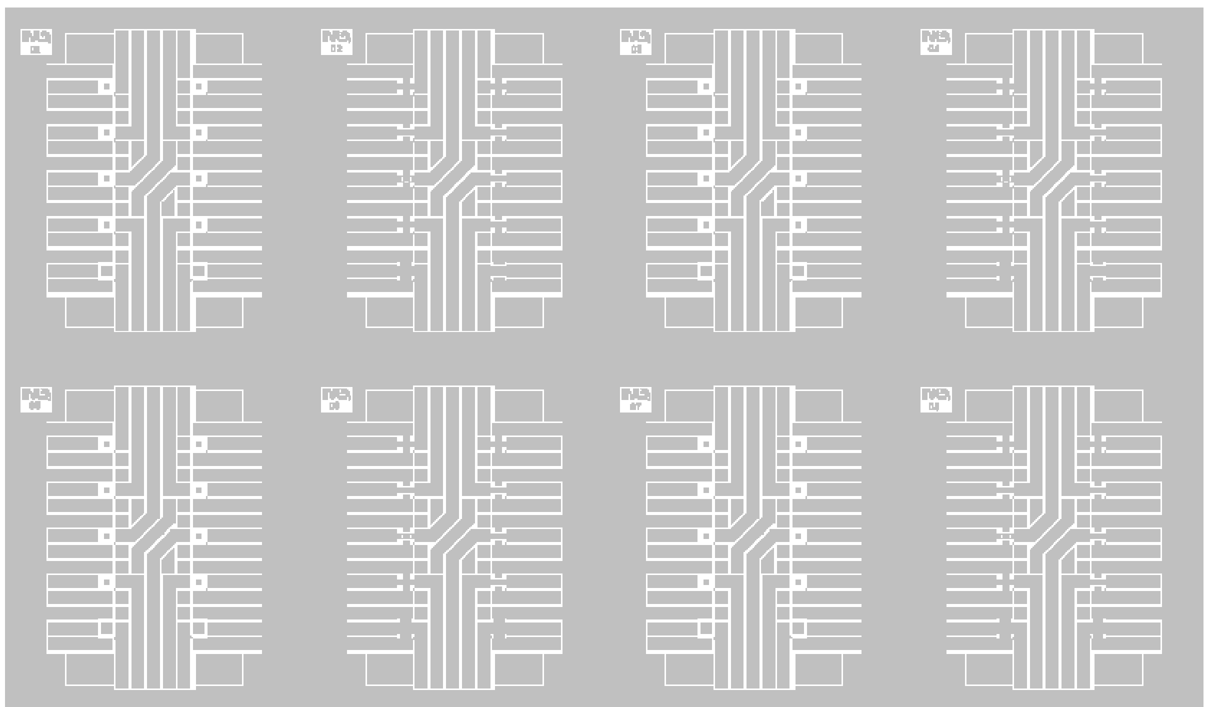

Appendix C

Appendix - BS Mask

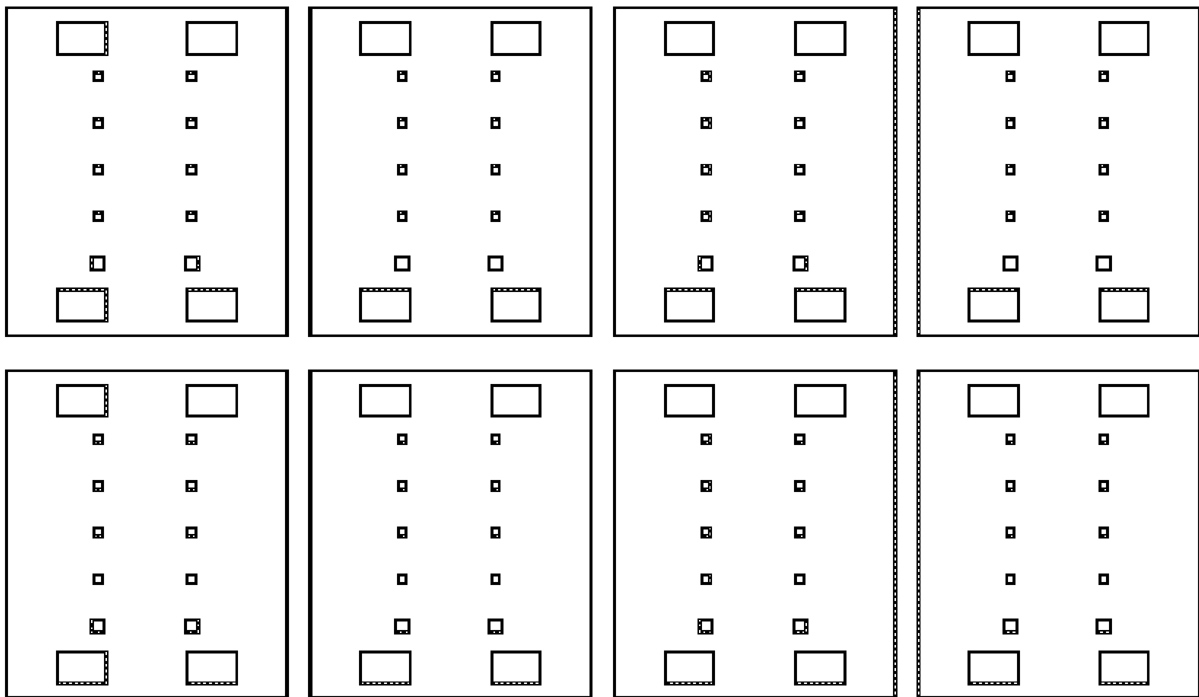

Appendix D

Appendix - Silicon Mask

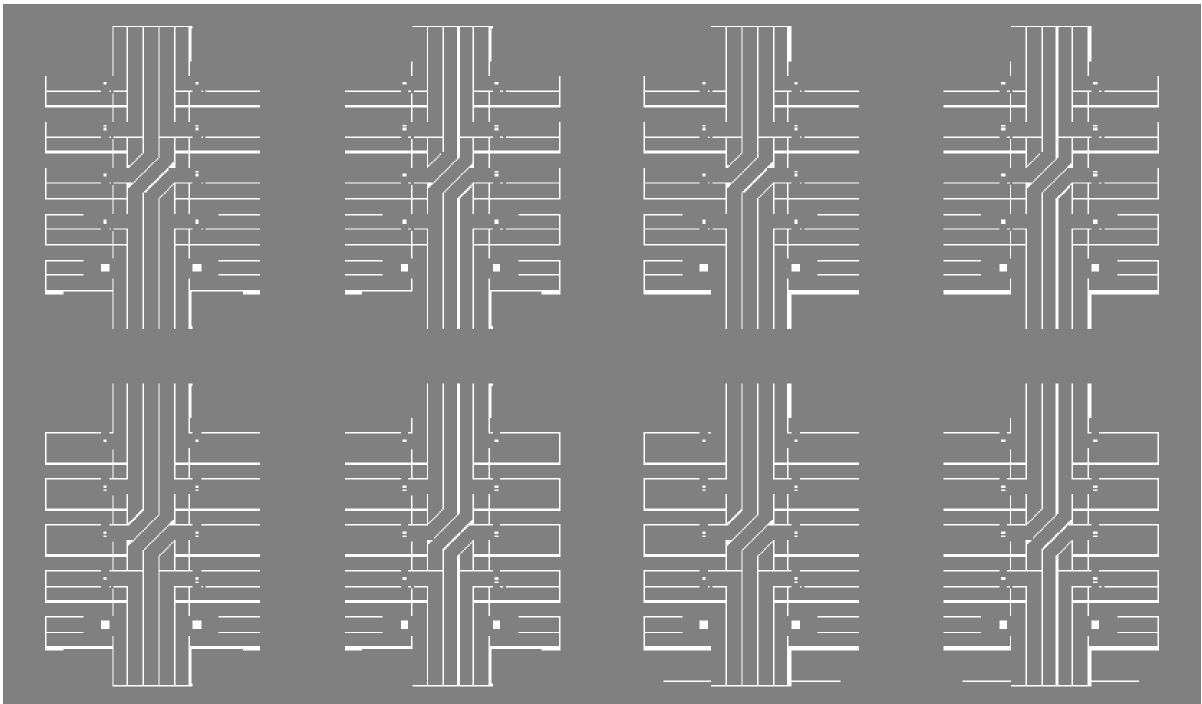

Appendix E

Appendix - Chip Carrier